

Application of Ultrasonic Motors to MR-Compatible Haptic Interfaces

THÈSE N° 4317 (2009)

PRÉSENTÉE LE 27 FÉVRIER 2009

À LA FACULTE SCIENCES ET TECHNIQUES DE L'INGÉNIEUR

LABORATOIRE DE SYSTÈMES ROBOTIQUES 1

PROGRAMME DOCTORAL EN SYSTÈMES DE PRODUCTION ET ROBOTIQUE

ÉCOLE POLYTECHNIQUE FÉDÉRALE DE LAUSANNE

POUR L'OBTENTION DU GRADE DE DOCTEUR ÈS SCIENCES

PAR

Dominique Chapuis

acceptée sur proposition du jury:

Prof. M.-O. Hongler, président du jury

Prof. H. Bleuler, directeur de thèse

Prof. E. Burdet, rapporteur

Prof. M. Lauria, rapporteur

Prof. Y. Perriard, rapporteur



ÉCOLE POLYTECHNIQUE
FÉDÉRALE DE LAUSANNE

Suisse
2009

Acknowledgements

This thesis describes four years of research carried out as a PhD student at the Laboratoire de Système Robotique (LSRO) at the Ecole Polytechnique de Lausanne (EPFL, Switzerland). I would like to thank the Prof. Hannes Bleuler, as he accepted me in his laboratory first as a project student, a research assistant and finally as a PhD student. I am grateful for the trust and the freedom he gives to me during this project. My gratitude also goes to the jury of this thesis, Prof. Max Hongler, Prof. Yves Perriard, Prof. Etienne Burdet and Prof. Michel Lauria for the time invested and their comments leading to the final version of this document.

This work is a part of the SNF project entitled "An fMRI compatible haptic interface to investigate brain mechanisms of manipulation". I thank the different partners of this project for this fruitful collaboration:

- Prof. Etienne Burdet from Imperial College London, for his interest in my work and his advices.
- Dr. Markus Klarhoefer and Prof. Klaus Scheffler from the Division of Radiological Physics of the University Hospital and University of Basel for the scanning time and the manpower provided to run the experiments.
- Dr. Sven Haller and Prof. Wilhelm Radue from the Division of Diagnostic Neuroradiology of the University Hospital of Basel for the design and the analysis of the several fMRI studies carried out during this project.

The results obtained in this work are not those they are without the help of some people which I am grateful:

- To Roger Gassert with whom I have worked closely for several years. Thanks to the complementarities of this team, we carried out a large amount of projects together. It was a pleasure to work with him and I hope it will continue.
- To my current and former colleagues from the LSRO for the friendly and stimulating atmosphere, especially to Patric Pham who is a true friend, to the different reviewers of this thesis, Francois Barrot, Thomas Moix and Thomas Bosgiraud, they also contributed to this project with their knowledge, to my office neighbors Laurent Sache and Evren Samur who have endured my presence for years.

- To the EPFL colleagues, such as Matteo Bullo and Markus Flueckiger who investigated the force-feedback with the USM, such as Emeric Grandjean and Guillaume Ding kindly shared with me the morning coffee and newspapers.
- To the semester and master project students who have made a bit, such as Ludovic Dovat, Oliver Lambercy, Xavier Michel, Yves Ruffieux, Simon Honold and Thomas Lemmin.
- To the *microtechnique* workshop staff, such as Jean-Jacques Crausaz, Jean-Claude Amendola, Pascal Zwbinden and Jean-Pierre Rougnon for their solutions and the care taken in the manufacture of the prototypes parts.

Last but not least, I would like to thank my family for their continuous support over the years and also Patrick for his contribution to the *apéro*. I dedicate this work to my beloved mother who gave me the taste of the studies and her support enabled me to concentrate totally writing this thesis.

This research was funded by the Swiss National Science Foundation, FNS-205321-104292/1. I thank Jtekt corp. Japan for providing the ceramic ball bearings.

Abstract

Functional Magnetic Resonance Imagery (fMRI) is an imaging technique allowing the observation of brain activity. Haptic interfaces can be used in conjunction with fMRI to stimulate the subject while measuring brain activity. Using robotic stimulation over conventional methods offers repeatability, flexibility and the possibility of logging of different experiment variables. Such system becomes a powerful tool for neuroscience study, diagnostic and rehabilitation.

The MR scanner with its high magnetic fields and radio frequency pulses is a harsh environment for a robotic system. Robots that can operate safely and do not induce disturbances in the imaging of the scanner are qualified as MR-compatible. The actuation of these robots is an important issue. Electrical power brought to the actuator represents an important source of interferences with the scanner. Since electrical motors cannot be introduced in the MR room, haptic interfaces are conventionally remotely actuated over a long transmission with the actuators placed outside of the MR room. In particular cases, such as the study of finger motion, small haptic interfaces with limited force ranges are required. Remote actuation methods impose transmission lengths and means that cannot be reduced nor scaled down thus imposing a trade-off between performances and size reduction in these applications.

This work investigates an alternative actuator that can achieve high-quality force-interactions with the fingers. The Ultrasonic Motor (USM) is MR-compatible and offers good performances. But it is not well suited for force-feedback and may be hazardous for the users. To address these issues, mechanical solutions are investigated by using an electrical analogy applied to mechanical systems. A novel actuation system using the USM as a power source and a clutch to control the output torque is proposed: the Hybrid USM Clutch Actuator (HUCA).

The first prototype validates the different mechanical concepts developed in this work. The second, MR-compatible, integrates a clutch based on electrorheological fluids (ER). MR-compatibility has been validated and performances evaluated.

Since the HUCA has the unique property of behaving both like a force source and a velocity source, dedicated control schemes have been developed to implement impedance and admittance force control. These enable the display of stiff walls and the rendering of a wide range of impedances thanks to the overlap of their range of displayable impedances. Compared to the hydrostatic transmission actuation, the HUCA shows higher performances and user safety. Furthermore, the powering through electrical wires allows developments of

multi-DOF interfaces.

Keywords: haptics, MR compatibility, USM, clutch, electrorheological fluid (ERF), impedance control, electrical analogy.

Résumé

L'Imagerie à Résonance Magnétique fonctionnelle (IRMf) est une technique d'imagerie permettant d'observer l'activité cérébrale. Les interfaces haptiques peuvent être utilisées avec l'IRMf pour stimuler l'activité cérébrale du sujet de manière répétable et flexible. Par ailleurs, ils permettent le suivi des données expérimentales. Cette association devient un outil puissant pour les études en neuroscience, le diagnostique et la réhabilitation.

Des champs magnétiques importants et des impulsions radio font des environs du scanner RM, un lieu hostile pour un système robotique. Les robots capables de fonctionner de manière sûre et sans perturber l'acquisition des images du scanner sont alors qualifiés de compatibles RM. L'actionnement de ces robots constitue un problème important. La grande quantité d'énergie électrique introduite dans la salle du scanner constitue une source potentielle importante de perturbations. Pour éviter cela, les interfaces haptiques sont généralement actionnées à distance par une longue transmission mécanique et un moteur placé à l'extérieur de la salle. L'étude des mouvements des doigts requiert des interfaces plus petites avec une gamme de force plus faible. La longueur imposée des transmissions ne peut pas être réduite imposant un compromis entre miniaturisation et performance.

Ce travail étudie un actionneur alternatif pouvant accomplir un retour de force de grande qualité avec les doigts. Le moteur à ultrason (USM) est compatible RM et offre de bonnes performances. Cependant il n'est pas adapté au retour de force et son utilisation n'est pas sûre. Pour résoudre ces problèmes, des solutions mécaniques ont été étudiées en utilisant l'analogie électrique appliquée aux systèmes mécaniques. Un système hybride inédit d'actionnement est proposé : l'HUCA, l'USM y fournit la puissance, alors qu'un embrayage contrôle son couple de sortie.

Un premier prototype valide les concepts mécaniques développés dans ce travail. Un second compatible RM intègre un embrayage à fluide électrorhéologique. Ses performances ont été évaluées, et sa compatibilité MR a été validée.

L'HUCA a l'unique particularité de pouvoir se comporter comme une source de force et de vitesse, pour l'exploiter des schémas dédiés de contrôle ont été développés et implémentés. Ils permettent de restituer des murs rigides et une large gamme d'impédances grâce au chevauchement de la gamme du contrôle d'impédance avec celle du contrôle d'admittance. Comparé à la transmission hydrostatique, l'HUCA démontre une meilleure sécurité et de meilleures performances. D'autre part, la transmission de puissance à l'aide de câbles électriques permet

le développement d'interfaces à plusieurs degrés de liberté.

Mots clés : haptique, compatibilité RM, moteur à ultrasons, embrayage, fluide électrorhéologique, contrôle d'impédance, analogie électrique.

Contents

1	Introduction	1
1.1	Motivation	1
1.1.1	MR-compatible Robotics	1
1.1.2	Actuation Issues	2
1.1.3	Fingers Interactions	2
1.2	Objective	3
1.3	Approach	4
1.4	Thesis Outline	4
2	MR-Compatible Actuators	7
2.1	Actuator for Force-Feedback	7
2.1.1	Introduction	7
2.1.2	Requirements	9
2.1.3	Human Factors	11
2.1.4	Conclusion	11
2.2	MR-Compatibility	12
2.2.1	Magnetic Resonance Imaging	12
2.2.2	Criteria	13
2.2.3	Conclusion	16
2.3	Overview of MR-Compatible Actuators	17
2.3.1	Electrostatic Actuator	17
2.3.2	Piezoelectric Actuator	18
2.3.3	Electrorheological Fluid	19
2.3.4	Electroactive Polymers	19
2.4	Conclusion	21
3	Ultrasonic Motor	23
3.1	Introduction	23
3.1.1	History	23
3.1.2	TWUSM Operating Principle	27
3.1.3	Characteristics	28

3.1.4	The TWUSM in Haptics	29
3.1.5	Conclusions	31
3.2	Electrical Analogy	32
3.2.1	Principle	32
3.2.2	USM Models	33
3.2.3	Thevenin's Equivalent	36
3.2.4	Comparison with a DC Motor	37
3.3	Conclusion	38
4	Proposed Mechanisms	47
4.1	Series Dynamics	47
4.1.1	Spring	47
4.1.2	Damper	51
4.1.3	Conclusion	55
4.2	Hybrid Actuators	55
4.2.1	Force-Controlled Clutch	56
4.2.2	Operating Modes	58
4.2.3	Properties	60
4.2.4	Safety	65
4.3	Conclusion	65
5	Implementation	69
5.1	Clutch Configurations	69
5.1.1	Direct Clutch	69
5.1.2	Redundant Clutches	71
5.1.3	Differential-Brake	74
5.2	Sensors	78
5.2.1	Motion	78
5.2.2	Force	79
5.3	Conclusion	80
6	Prototypes	87
6.1	Non MR-Compatible Haptic Knob	87
6.1.1	Design	87
6.1.2	Preliminary Control Tests	90
6.1.3	Conclusion	92
6.2	MR-Compatible Haptic Knob	93
6.2.1	Design	93
6.2.2	MR-compatible Torque Sensor	95
6.2.3	ERF Differential-Brake	97
6.2.4	MR Compatibility Testing	103

6.2.5	Conclusion	105
6.3	Conclusion	105
7	Evaluation of the Performances	107
7.1	Setup Configuration	107
7.2	Velocity control	108
7.2.1	USM Characteristics	108
7.2.2	Closed-Loop Control	110
7.2.3	Performances	112
7.2.4	Conclusion	113
7.3	Torque control	114
7.3.1	Clutch Characteristics	114
7.3.2	Open-Loop Control	116
7.3.3	Closed-Loop Control	117
7.3.4	Performances	117
7.3.5	Conclusion	119
7.4	Indirect force control	119
7.4.1	Impedance control	120
7.4.2	Admittance control	123
7.4.3	Conclusion	123
7.5	Transparency and Walls	124
7.5.1	Transparency	124
7.5.2	Wall	125
7.5.3	Conclusion	126
7.6	Comparison with the Hydrostatic Transmission Interfaces	127
7.6.1	Specifications	127
7.6.2	Performances	128
7.7	Conclusion	129
8	Conclusion	131
8.1	Contributions of this Thesis	131
8.2	Outlook	133
	Bibliography	135
	Nomenclature	145
	Curriculum Vitae	151

Chapter 1

Introduction

1.1 Motivation

1.1.1 MR-compatible Robotics

The Magnetic Resonance Imagery (MRI) is a non invasive imagery technique used to perform anatomical scans. The produced images are three dimensional and present a good tissue contrast and a spatial resolution below 1 *mm*. Thus, MRI is mainly used for the diagnosis of the different lesions or tumors. With the MRI, it is possible to image the brain activities. This is called functional Magnetic Resonance Imagery (fMRI). The fMRI is mainly used in neuropsychology or cognitive studies.

The robots can be associated to the MRI, and two types of applications can be distinguished:

Interventional robots: The MRI gives the position of the surgical tool with respect to the different body parts and can image parts that are not accessible with an endoscope. The limited space in the scanner and the low acquisition time make the robots use advantageous to perform the surgery or at least to be used as a guide. The majority of these interventional robots are used for percutaneous interventions like brachytherapy or biopsy [Masamune 95, Chinzei 00, Larson 04, DiMaio 06, Melzer 08]. An other possible application for surgical robots is laparoscopy, a minimally invasive surgery [Kim 02, Oura 06].

Haptic interface: Associated with the fMRI, the robot is a mean to stimulate the subject in order to obtain brain activities. The advantage of a robotic stimulation over conventional methods is its repeatability and the possibility to record the different experiment variables. The applications of these robots are neuroscience studies, diagnosis and rehabilitation. Usually interacting with the hand, these robots are placed at the entry of the scanner bore. Vibrotactile stimulators were the first haptic interfaces used in a MR

environment [Golaszewski 02, Zappe 04]. Force feedback interfaces allow more complex tasks such as rehabilitation exercises in the MRI [Khanicheh 05, Riener 05].

Although the important advantages brought by the association of robots with MRI, the MR environment with its high-magnetic fields and radio frequency pulses is a harsh environment for a robotic system. On another hand, the MR scanner is very sensitive to magnetic field inhomogeneities or Electro Magnetic (EM) noise that a robot can emit. Robots that can operate safely without disturbing the imaging of the scanner are qualified as MR-compatible.

1.1.2 Actuation Issues

To comply with the MR-compatibility constraints, specific materials, sensors and actuators must be used in the robot. The actuation is an important issue. It determines a main part of the device performance on the one hand, and on the other hand the electrical power brought to the actuator may be an important source of interferences with the scanner [Gassert 06d].

To actuate its MR-compatible haptic interfaces, the Laboratoire de Systèmes Robotiques (LSRO) has developed a solution based on *hydrostatic transmissions*. Since electrical motors cannot be introduced in the MR room, these interfaces are remotely actuated over a long transmission between 6 m to 10 m. The motion of the motor placed outside of the MR room is propagated from a master piston to a slave piston through hoses filled with oil. This actuation method has been successfully used in a wrist interface [Moser 03], a 2 Degrees of Freedom (DOF) interface (Fig. 1.1(a)) to perform arm reaching movements [Gassert 06a]. Both are used at ATR (Advanced Telecommunications Research Institute), Japan. These developments are summarized in a PhD thesis on the MR-compatible robotics in general and MR compatibility testing procedures [Gassert 06c].

1.1.3 Fingers Interactions

This work takes place in the frame of the project "An fMRI compatible haptic interface to investigate brain mechanisms of manipulation" [Bleuler 03]. The goal of the project is to study the control of the fingers and to develop the MR-compatible robotic technology required to perform it. The study of fingers has several advantages:

- The brain areas related to the fingers are large proportionally to the fingers sizes.
- The motions of the finger has a limited influence on the imaging process.
- Fine motion tasks can be performed with fingers.

However, from a robotic point of view, the development of a device to interact with fingers poses some challenges:

- The small size of the fingers requires a miniaturized interface.

- Their limited force range requires an interface with low friction and inertia to prevent fatigue.

An interface based on the hydrostatic transmission has been developed to study the motions between the thumb and the index : the *finger interface* (Fig. 1.1(b)). It has been used in different fMRI studies [Honold 06].

In this interface, the piston sizes have been reduced in order to match the finger forces and sizes. Since the hose lengths depend on the scanner room, they could not be shortened and therefore increased the influence of the transmission in the system. In the finger interface, the transmission inertia, compliance and friction are proportionally larger compared to larger size systems for example [Gassert 06a].

Because their lengths cannot be reduced, the hydrostatic transmissions and the other remote actuation methods cannot be scaled down with the haptic interfaces. For small haptic interfaces, the relative compliance, friction and inertia of the transmission increase largely their influence on the output force and limit the achievable performances. An alternative actuation method is required for the interaction with the fingers and other small haptic interfaces.

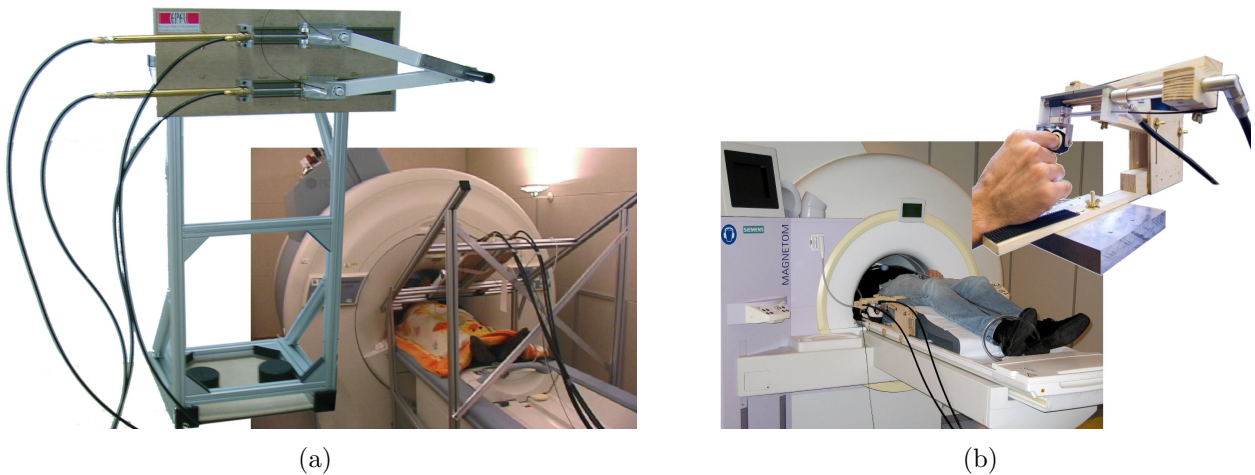


Figure 1.1: (a) 2 DOF interface used to investigate arm motion [Gassert 06a]. (b) Finger interface developed in the project [Bleuler 03].

1.2 Objective

The objective of this work is to develop a high-performance MR-compatible actuator for the force interaction with the fingers. This actuator must be force-controlled in order to display force fields and free motion.

1.3 Approach

In order to achieve a high-quality force-feedback, the control aspects must be considered in the choice of the actuator principle and during its design. Because the remote actuation methods impose a tradeoff between performances and size reductions, these methods must be avoided. Only actuators that can be placed in the MR room, close to the subject's hand will be considered.

To ensure the MR-compatibility of the developed solution, only MR-compatible physical principles, materials and components will be considered in the development of the actuator, and MR-compatibility tests must be performed on the final prototype.

From the different actuators with a MR-compatible transduction principle, the Ultrasonic Motor (USM) shows the best performances, however because of some characteristics, the USM is not adapted to perform force-feedback and may be hazardous for the users:

- Velocity controlled.
- Non reversible.
- The motor locks its output when it is turned off.

The USM force control and safety issues must be addressed to allow a safe interaction and a high-quality force feedback with the subject. Since these undesired features are mainly due to the high output impedance of the USM, pure control approaches will lead to poor performances.

In this work, mechanical solutions to modify the output impedance of the USM will be investigated. In haptics, electric concepts like impedance or admittance are applied to mechanical systems. Therefore, the use of electrical analogy can lead to tools and solutions used in electricity.

To rapidly validate concepts, before developing finalized MR-compatible versions, some preliminary tests can be performed on non-MR-compatible prototypes using standard components.

In order to evaluate the performance of the developed actuator, its main parameters must be identified and appropriate control schemes must be implemented.

1.4 Thesis Outline

The next chapter defines the MR-compatibility and its constraints. The requirements of actuators for haptic interfaces are given. An overview of the different MR-compatible actuation principles is presented and their abilities to perform force-feedback are discussed.

Chapter 3 presents the USM, its history, operating principle and important characteristics. An overview of haptic interfaces actuated by the USM is made. A linear model of the USM is

set, and the electrical analogy is used to explain the influence of the USM output impedance in the force control.

Chapter 4 analyzes the different mechanical solutions to modify the USM output impedance in order to improve its safety and its performances in force control. The Hybrid USM Clutch Actuator (HUCA), based on the association of the USM and a clutch, is proposed and its properties are discussed.

Chapter 5 analyzes the different solutions in order to reduce the inertia of the clutch. A system based on the combination of a differential with a brake is proposed. The sensors required for the operations of the HUCA and their positioning are discussed.

Chapter 6 presents the mechanical design of the two realized HUCA prototypes. The first is constituted of standard components and validates the concepts with preliminary control experiments. The second prototype is MR-compatible, the design of its electrorheological brake and the associated high-voltage driver is described. The MR-compatibility of this second prototype is validated.

Chapter 7 investigates the different control schemes adapted to the HUCA specificities. Its performances in the different control modes and its capacity to display transparency and hard contacts have been evaluated. The HUCA is compared to the finger interface.

Chapter 8 summarizes the contribution of this work to the actuation of MR-compatible haptic interface. Future work directions concerning the HUCA are suggested.

Chapter 2

MR-Compatible Actuators

In this chapter, the different aspects of a MR-compatible actuator for force feedback are discussed such as its definition of the actuator, its requirements and the MR-compatibility criteria. An overview of MR-compatible actuators and their suitability to this application are discussed.

2.1 Actuator for Force-Feedback

In this section, the different requirements of actuators in a force-feedback system are presented and their consequences on the actuator for finger interaction are presented.

2.1.1 Introduction

The goal of the force feedback or force reflecting interface is to reproduce in the physical world a physical interaction created in a virtual environment. The virtual environment is implemented on a computer and belongs to the electrical domain whereas the force belongs to the mechanical domain, the force feedback interface must ensure the link between these two domains and thus the force feedback interface is intrinsically a mechatronic system. The key components for this interaction are the transducers (actuators and sensors) that convert the signal from a domain to another (Fig. 2.1). Their definitions may vary and could be more or less restrictive concerning the domains. In this thesis, only electrical and mechanical domains will be considered for the definition.

Sensor measures a physical quantity and transforms it into an electrical signal.

Actuator converts the *electrical power* input into *mechanical power*. Two types of actuators can be distinguished [Pons 05]:

Active actuators can output and dissipate mechanical power.

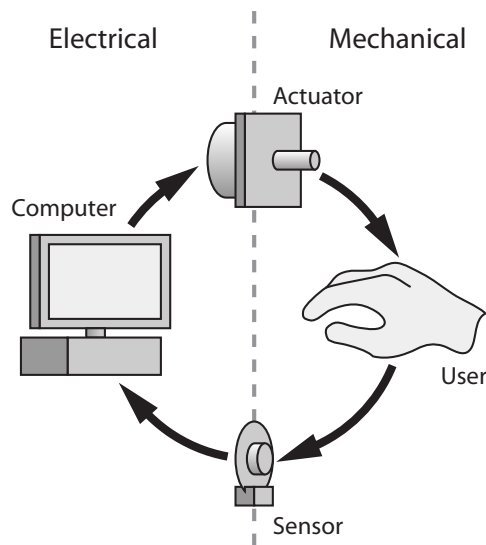


Figure 2.1: A haptic interface allows the interaction between a virtual environment (symbolized by the computer) and the physical world (symbolized by the hand).

Semi-active actuators can only dissipate mechanical power. For this reason, we can consider brakes or clutches as actuators, if they are controlled by an electrical signal.

The power is not completely converted by the actuator from a domain to another, there is some power loss dissipated in heat (Fig. 2.2). This effect is undesired in the active actuator, because it reduces its efficiency, but is necessary for the semi-active actuator.

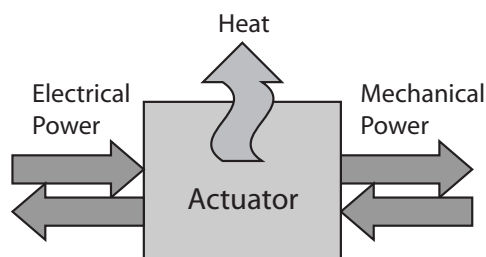


Figure 2.2: Power flows in an actuator

2.1.2 Requirements

During fMRI study, the haptic interface must be able to display arbitrary forces, then the actuator for finger interactions must be an active actuator, as the semi-active one can only display resistive forces.

During force interaction, every components of the chains influence each other (Fig. 2.1), and the virtual environment (in particular the control) and the mechanical components are closely linked. The choice of the control algorithm will determine the type of actuators and reciprocally. Before discussing the different control mode possibilities, the concepts of impedance and admittance must be introduced first.

The mechanical interactions on an object can be defined by a force response to an applied motion. If this relation is linear, the object can be described by its impedance, the admittance gives the inverse relation. These concepts comes from the electrical domain.

Impedance The impedance \underline{Z} determines the force response of a linear system for a given harmonic motion:

$$\underline{Z} = \frac{\underline{F}}{\underline{V}} \quad (2.1)$$

Where \underline{F} is the complex force and \underline{V} is the complex velocity. The system inertia, viscosity or stiffness can be described in term of mechanical impedance.

Admittance The admittance \underline{Y} is the inverse of the impedance and gives the motion of the mechanical system \underline{V} in function of the applied force \underline{F} :

$$\underline{Y} = \frac{\underline{V}}{\underline{F}} \quad (2.2)$$

The impedance is an important notion in haptics as it can be used to describe the user, the interface and the virtual objects. An other suitable approach to represent multi-domains systems are bondgraphs. They have been applied to analyzes haptic interfaces in [Spaelter 06].

As ideal sensors and actuators measure and output forces or motions (usually position or velocity), then there are four possible connections or control schemes as shown in Fig. 2.3. Each control scheme has its specificities:

Direct force control outputs a force to a given input force. The force-feedback loop gives a good control on the displayed force.

Impedance control outputs a force to a given input motion. This is a indirect force control method.

Admittance control outputs a motion to a given input force. This is a indirect force control method.

Motion control outputs a motion to a given input motion. This control scheme doesn't allow the control of the force.

The admittance and impedance control schemes are indirect force control, because the output force depends on the output motion, thus they are also called interaction controllers [Hogan 04]. They are not only dual in their schemes, but also in their performances [Adams 02]. Then the choice of the type of control scheme will also influence the mechanics of the device. During psychophysical experiments with fMRI, free motions are often used and force field are displayed, then the direct force control and the impedance control in conjunction to a lightweight haptic interface are the most suitable [Hogan 04]. The impedance control requires force-controlled actuator and lightweight interfaces as it neglects their inertia [Hogan 85]. With a device with high friction and high gear ratio, inertia, like the hydrostatic transmission, admittance control can be used to display lower impedance at low frequency. However at high frequencies, the dynamics of the controlled device remains the same than the uncontrolled dynamics [Newman 92]. Thus a lightweight force-controlled actuator is preferred.

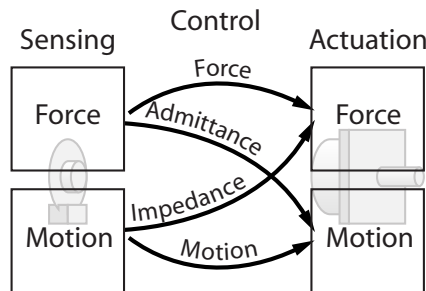


Figure 2.3: The different control possibilities

As a haptic interface has to interact with humans, it has to be safe. The following measures must be implemented on the actuator.

Safe power off state The interface may be powered off suddenly, when the emergency button is pressed or when the power is cut off. In this case, the interface must return in a safe state. For a haptic interface, this means to let the user move freely, otherwise remaining forces may harm the user.

Limited output ranges Injuries may result when the interface produces high forces. This may happen when the output force of the interface is not limited or when an impact happens at high speed. Output force and speed must be limited to prevent this. Usually the maximum output force is limited by the actuator itself and the speed by software.

2.1.3 Human Factors

The other requirements come from the demand of quality force-feedback that depends on the human perception.

In order to have a realistic perception of the force interaction, the performances of the device must be beyond the human perception. Various body sensors have their respective sensitivity, and the following haptic requirements for the interaction with fingers come from [Tan 94]:

Position Resolution It must be below 2 mm , by considering the finger joints position Just-Noticeable-Difference (JND) of 2.5° and a 50 mm finger.

Force Resolution It must be below 0.15 N . It is determined by the finger force JND at low frequencies. The finger force JND between the thumb and the index is in average 7% of the applied force F_0 , with F_0 in the range of 2.5 N to 10 N [Pang 91].

Force Range The maximum output force must be between 10 to 50 N for interactions with fingers or the hand. The finger can outputs controlled force up to 50 N . This value decreases by more than half for a sustained force.

Bandwidth It must be above 7 Hz for kinesthetic¹ interactions. This value corresponds to the upper limit of the human force control. However, the humans are very sensitive to low frequency vibrations, below $< 30\text{ Hz}$ one can perceive vibrations with $1\text{ }\mu\text{m}$ amplitude. Humans can feel vibrations up to 1 kHz . The interface should avoid producing vibrations in order to keep the feeling of smooth motion.

Stiffness In order to render hard object the interface should be able to output stiffness higher than 24N/mm .

2.1.4 Conclusion

Actuators for force-feedback are subject to requirements from different origins. The actuator applications to fMRI studies require an active actuator that output torque to display arbitrary forces. Human perception has a very large bandwidth, thus it is almost impossible to build devices covering the whole perception range. This means that tradeoffs have to be taken in term of force range and bandwidth according the application requirements. In order to keep a safe interaction, the output of the actuator should be limited in term of force and velocity. When the other requirements conflict with the safety, safety requirements should prevail.

¹related to the sensation by which bodily position, weight, muscle tension, and movement are perceived

2.2 MR-Compatibility

It is important to understand the principle of MRI in order to identify the possible interferences between the MR scanner and the mechatronic device, then the MR-compatibility criteria are presented.

2.2.1 Magnetic Resonance Imaging

MRI is based on the *Nuclear Magnetic Resonance* (NMR) phenomena of the hydrogen nuclei that are abundant in biological tissues. When a strong static magnetic field B_0 (0.5 to 3 T for clinical scanners and up to 9.4 T for research) is applied on the tissues, these spins get oriented parallel and anti-parallel to the B_0 direction. The resulting *net magnetization* is parallel to B_0 . If we observe a single spin, its magnetization forms a fixed angle to the direction of B_0 and precesses around at the Larmor frequency f_L . This frequency is proportional to the magnetic field B_0 and is 42.58 MHz/T for the proton. The resonance occurs when an electromagnetic field with the Larmor frequency is applied to the tissue.

Because the Larmor frequency is in the range of the radio frequencies (several MHz), the exciting electromagnetic field is called *Radio Frequency (RF) Pulse*. The effect of the excitation depends on the time length and the intensity of the RF pulse. It has two consequences, it cancels or even reverses the longitudinal net magnetization, and a *transverse* magnetization (perpendicular to B_0) appears. After the RF pulse, the different spins return to their initial states, this is the *relaxation*. During the relaxation, radio frequency waves are emitted by the tissues and are recorded. Biological tissues could be then identified based on their typical relaxation times.

To enable three-dimensional reconstruction, a magnetic gradient induced by switching magnetic fields is applied in the three directions of the space in order to spatially encode the radio signal.

The fMRI uses the oxygenation of the blood to observe indirectly the brain activity. The magnetic susceptibility of the blood changes with its oxygenation level, this is the *Blood Oxygenation Level Dependant (BOLD) effect* [Heeger 02]. The image variation due to the brain activities is very small (only a few percent of the picture intensity).

The MRI and fMRI result of a chains of complex physical phenomena and requires a high static magnetic field, fast switching magnetic fields and radio frequency pulses in order to form images. If one of these components is disturbed, the image will be degraded, thus MRI is very sensitive to magnetic perturbation and electromagnetic noise. Thanks to the hemodynamic response, the fMRI allows to image the brain activities. fMRI is even more sensitive to the field inhomogeneities than MRI as it uses the change of magnetic susceptibility to image the brain activity. Therefore, the scanner used for MRI and fMRI is placed in a shielded room to avoid EM perturbations, and electronic devices should not be introduced in the MR-room.

2.2.2 Criteria

The MR-compatibility is a complex issue. On the one hand the MRI is very sensitive to the EM noise and magnetic field perturbation and on the other hand the MR environment is very harsh for a mechatronic device due to the strong magnetic field and their EM emissions. During the design of the actuator, the scanner electromagnetic fields must be taken into account to obtain a MR-compatible device, for example the values of the 3 T scanner used for the experiment on the finger motion are summarized in the Table 2.1.



Table 2.1: Siemens Allegra Magnetom 3T Specifications

Static Magnetic field	DSV ^a	220 mm
	Field strength	3 T
	Homogeneity	< 0.1 ppm Vrms
Switching Magnetic field	Max. amplitude	40 mT/m per axis
	Slew rate	400 mT/m/ms per axis
RF pulses	Frequency	123.2 MHz

^aThe Diameter of Spherical Volume (DSV) is the volume inside what the scanner specifications are valid. It corresponds also to the field of view of the scanner.

As defined in [Chinzei 99], a MR-compatible device must fulfill 3 criteria:

- it must be *MR-safe*.
- its use in the MR-environment should not affect the *imaging quality*.
- its operation should not be disturbed by the MR-environment.

These criteria depend on the mutual influence of the scanner and the device, the criteria on the MR-safety and the normal operation are determined by the influence of the scanner on the device, while the criterion on the image quality is defined by the influence of the device on the scanner. Since the MR-safety and the normal operation criteria depend on the same phenomena, their discussion will be grouped. These discussions introduce the criteria for general case, and their consequences on an actuator placed in the hand area.

MR-Safety and normal operation

In this section phenomena determining the MR-safety and the normal operation of the device will be discussed. Safety is essential in the definition of the MR-compatibility and limits the hazards created by the introduction of the device in the MR room. The term of MR-safe relates to *a device that poses no safety hazard in the context of a defined application, imaging sequence and placement within the MR environment* [Gassert 08a]. Thus the term of MR safe must be specified with the normal use conditions².

The different electromagnetic fields used in the scanner are sources of hazard for the user and sources of dysfunctions for the device. In [Food 97], different injuries and accidents are reported and show in which ways devices may be dangerous.

Static magnetic field The intensity of the magnetic field can reach 3 T for the clinical scanner, this value is twice the remanence of the strongest permanent magnet.

For the subject, this high magnetic field produces strong forces that attract ferromagnetic materials into the bore of the scanner and will hit the subject, i.e. *missile effect*.

For the device, the strong magnetic field creates parasitic forces in the ferromagnetic components and braking forces due to the eddy currents in the electrically conducting moving components. Another effect can be the demagnetization or the saturation of magnetic materials. These effects may damage electromagnetical actuators.

To avoid this, magnetic and ferromagnetic materials should be avoided, or if they have to be used, they must be carefully fixed in the MR room. Note that not only steel and iron, but also nickel and cobalt are ferromagnetic. The moving parts of the device should be not conducting.

Switching magnetic field The switching magnetic field causes eddy current in electrically conductive objects, which are generally too low to produce an excessive heating, but may damage electronics components.

For the user and the device, this may be a hazard if it results a failure of vital devices such as pacemakers.

Electronic parts should not be introduced in the MR-room, otherwise they must at least be shielded.

RF pulses Due to its high frequency above several MHz, RF pulses may induce eddy currents in conductive material, creating an excessive heat.

For the user, this represents a burn hazards.

For the device, the RF pulses are an important source of noise that may degrade sensors signal and could damage the electronic.

²The term MR safe used in the robotic community and used in this report corresponds to the term of MR conditional in the standard F2503-05 published in 2005 by the American Society of Testing Material.

For these reasons conductive material and electronics should be avoided near the isocenter. If they have to be used, tests must be performed to evaluate the resulting heat and the influence on the operations of the electronic.

In area of the subject's hand, the influence of the switching magnetic field and the RF pulses are decreasing. Thus the actuators have to respect mainly the constraints related to the static magnetic field. These constraints prohibit the use of magnetic materials and limit the use of conductive material.

Image Quality

Mechatronic systems are constituted of many components that could influence the scanner in several aspects and due to the scanner high sensitivity, image degradations, called *artifacts* may appear. Only tests with the specific imaging sequence could verify the quality of the produced image. The typical artifacts sources in a scanner are:

Magnetic field inhomogeneities In order to operate properly the scanner requires a high field homogeneity below 1 *ppm* depending on the model.

Closer a component is placed from the imaging area, the more similar its susceptibility must be to those of biological tissues and to those of water ($\chi_{water} = -9 \times 10^{-6}$). In the imaging area the difference must be smaller than 10^{-5} . Outside this area, material with a susceptibility up 10^{-5} could be used [Schenck 96].

Electromagnetic motors even without magnetic material may degrade the homogeneities of the magnetic field with the induced fields of their own coils. Thus electrical currents have to be limited as much as possible.

The motion of conducting material in the spatial gradient of the static magnetic field can induce eddy currents, and the resulting magnetic counter field creates magnetic field inhomogeneity.

The magnetic inhomogeneities degrade the spatial encoding, leading to images distortions.

RF Pulse Dimming If conductive materials are placed inside the imaging area, the RF pulses will induce eddy currents that will create a magnetic counterfield. The amplitude of the RF pulses will be dimmed by this field [Bennett 96]. RF pulses are localized in the imaging area and decrease quickly outside this area, thus conductive material must be avoided in the proximity of the imaging area.

On the images, lobes and intensity loss will appear around conductive material.

EM noise The Electro Magnetic (EM) noise affects the scanner, by degrading the recorded radio signal. Because the signal intensity is low, the image will be very sensitive to the EM noise. The image becomes noisier and the Signal to Noise Ratio (SNR) decreases.

There are multiple sources of EM noise making its reduction difficult. Normally, the bandwidth of the signal measured by the sensors is lower than the one used by the scanner. However digital sensors, like incremental encoders can produce high frequency noise due the switching between low and high voltage levels.

Actuators are an important source of noise due to amount of power carried by their power signals. This means that Pulse Width Modulation, with its switching signal, must be avoided. The cables can also bring noise from the external environment to the MR room.

To reduce this effect a proper shielding of the different components must be carried out. The shield must be connected to the scanner room ground, and ground loops must be avoided. A low-pass filter must be used to suppress the high frequencies that may interfere with the recorded signal of the scanner. Thus the cut-off frequency must be at least several orders below the Larmor frequency.

In the subject's hand area, the source of disturbances that can still influence the scanner is the magnetic field inhomogeneity and the EM noise. For its operation, the MRI uses almost the whole bandwidth of magnetic and electric fields. In the low to the middle frequencies range (several kHz), there are the static and the switching magnetic fields and, in the very high frequencies (several MHz), the RF pulses occupy both magnetic and electrical fields. The only remaining space for the operation of a MR-compatible actuator is the electrical field in the static to the middle frequency range (Fig. 2.4). To keep the right amount of power without creating parasitic magnetic fields, the actuator must then operate with low currents and thus with high voltages.

2.2.3 Conclusion

Haptic interfaces are usually placed in the hand area, which means that the device is at the entrance of the scanner bore, i.e. a region where the influence of the RF pulses and switching field is weak. However the gradient of the magnetic field is very high in this region. The MR-compatibility requirements applied to the haptic interface knowing this position allows the use of non ferromagnetic metals, like copper, brass, bronze or aluminium in addition of the polymers and ceramic materials. However if the metallic parts move, their sizes must be limited in order to reduce the eddy currents.

The use of electromagnetical actuators must be avoided in the MRI as they do not fulfill any of the three MR-compatibility criteria. They can neither be adapted in order to become compatible, because their principle requires the conversion of electrical power in magnetic power. This conversion will interfere with the different magnetic field of the scanner. Thus electromagnetic actuators are intrinsically non MR-compatible. Only actuators with transduction principle using the electric field at high voltage and low current may be MR-compatible as they limit the possibilities of signal interactions with the scanner.

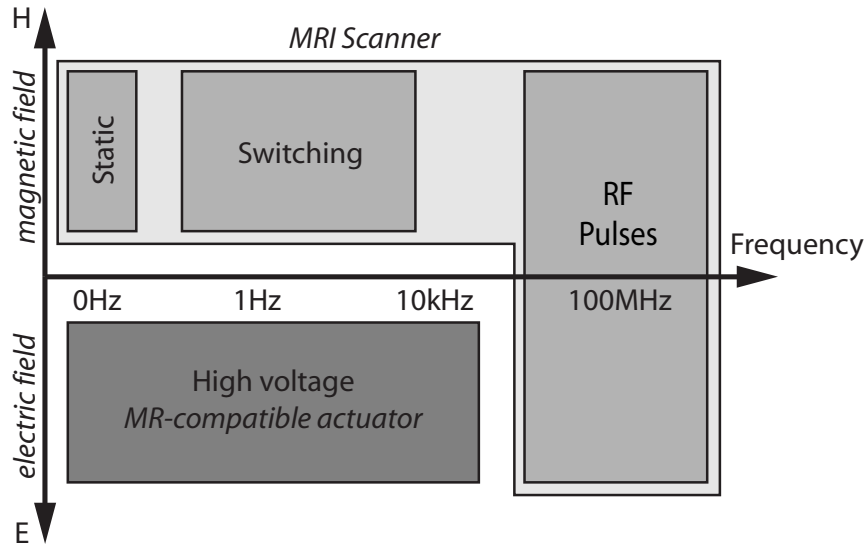


Figure 2.4: Occupation of the electromagnetic fields of the MRI. The MR-compatible actuator can use the electric field at low and mid frequencies.

2.3 Overview of MR-Compatible Actuators

Conventional force-feedback actuators, electromagnetical motors, can not be used in the MR environment. The variety of solutions and principles developed for this application shows the difficulty to actuate an MR-compatible force-feedback interface. This review will describe MR-compatible actuators and discuss their suitability for force-feedback. In the remote actuation methods, transduction elements do not operate in the MR environment and due to their limitations, they have not been included in this discussion. A more comprehensive review can be found in the paper [Gassert 06d].

2.3.1 Electrostatic Actuator

The electrostatic force is the most natural way to obtain force from high electrical fields. This phenomenon has been exploited in an MR-compatible actuator [Yamamoto 05] called Dual Excitation Multiphase Electrostatic Drive (Fig. 2.5(a)). This is a synchronous linear motor constituted of pairs of flexible printed circuit boards. On these films three phases electrodes are printed and three sinusoidal high voltage signals are used to drive the motor. Because the electrostatic force is small, the pairs of PCB are stacked and dielectric fluid is used to prevent breakdown due to the high voltage. The actuator tested was able to output 8 N with a voltage of 1.4 kV. In terms of MR-compatibility this actuator doesn't pose any problem, its current consumption is below 5 mA, and the frequency of the driving signal is in the tens of

Hz depending on the velocity. Due to its synchronous drive principle, this actuator is suitable for admittance control but has a limited travel range. The main difficulty in this principle is the high voltage amplifiers required to create the driving signal, and the main limitation is the low speed achievable. Recently, the electrostatic actuation principle has been integrated into a MR-compatible 2 DOF translational joystick [Hara 09].

2.3.2 Piezoelectric Actuator

In order to obtain higher forces than electrostatic forces, smart material like piezoelectric ceramics can be used. In contrast to electrostatic forces, the force obtained with a piezoelectric ceramic is large, but its deflection due to the high Young modulus of the ceramic is very small. They can for example be used as vibrotactile stimulator [Harrington 00].

In order to allow force interactions with piezoelectric actuators, movement amplification is required.

Ultrasonic motors The ultrasonic motor is based on the piezoelectric motor and uses mechanical resonance in order to amplify the motion of the piezoelectric ceramics. This motor is widely used in surgical MR-compatible robots [Masamune 95, Chinzei 00, Kim 02, Larson 04, Oura 06].

The USM requires a lower voltage of about 150 V, a higher current of several tens of mA and a higher driving frequency of several tens of kHz . From an MR-compatibility point of view, this is less favourable than the electrostatic actuator, but tests have shown that it can be used while an fMRI sequence is running [Hartwig 04].

The ultrasonic motor has a high torque output and low speed that allows using it as direct drive in a haptic device. Its response time can be below 1 ms . In [Flueckiger 05], an ultrasonic motor was used to display forces in an MR environment (Fig 2.5(b)). However, this system can hardly display low forces.

Piezoelectric valve Another way to obtain large motion amplitudes with piezoelectric actuators is to use them instead of electromagnetic actuators to actuate pneumatic valves. These valves have been used in a MR-compatible needle guide [DiMaio 07].

Piezoelectric valves do not pose MR-compatibility problems as the main source of power is provided by compressed air. Therefore, the required electrical power is limited.

Thanks to its MR-compatibility, this valve can be placed close to the piston reducing the delay and compliance felt on the piston output. As other pneumatic systems, this system is not well suited to output forces, but rather for position control.

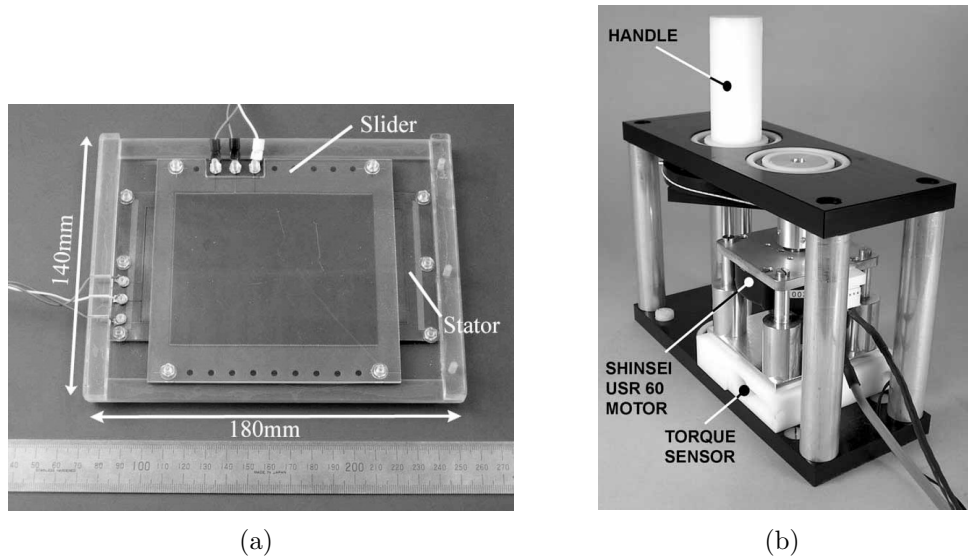


Figure 2.5: (a) Dual Excitation Multiphase Electrostatic Drive, reprinted from [Yamamoto 05].
 (b) MR-compatible handle actuated by an USM, reprinted from [Flueckiger 05].

2.3.3 Electrorheological Fluid

This actuation principle differs from the previous ones as it can only display resistive force. Thus, actuators based on electrorheological fluids are considered as semi-active actuators. The electrorheological fluid consists of particles in suspension in oil. The application of a high electrical field on this fluid will modify the viscosity, by increasing its yield stress. This effect which is similar to dry friction can be used to actuate brakes, clutches or any other damping devices.

Because it dissipates mechanical power, the electrorheological actuator needs only little electrical power. Its operation requires high driving voltages from 1 kV to 5 kV , but its current consumption is below 1 mA . [Khanicheh 05] reports the development of a handle actuated by an electrorheological fluid actuator (Fig. 2.6(a)) and its MR-compatibility tests.

The electrorheological fluid actuator is well adapted to display resistive forces: it is force controlled and has a response time below 1 ms .

2.3.4 Electroactive Polymers

An emerging group of actuators uses Electroactive Polymers (EAPs) as transduction elements. The used principles are multiple and give different properties to the EAP. Their lower Young modulus compared to piezoelectric ceramics allows larger displacements. [Bar-Cohen 04] distinguish two groups of EAP:

Electronic EAP is based on physical phenomena:

- The **electrical field** changes the polymer molecules shapes (Ferroelectric³ Polymer) or aligns the polymer molecules along it (Electrostrictive Graft⁴ Elastomers).
- **Coulomb forces** are used to squeeze a elastomer between two electrodes creating a lateral expansion of the elastomer (Dielectric EAP or Electro Polymer Artificial Muscle (EPAM)).

Electronic EAP have interesting properties for robotic as they can hold their displacement and have a high bandwidth. In addition the high-voltage and low current required for their operation make their use possible in the MR environment.

Ionic EAP uses the motion or the diffusion of ions and then implies chemical reactions. This group includes the Ionic Gels (IGL), Ionomeric Polymer-Metal Composite (IPMC), Conductive Polymers (CP). Their mechanism are complex and beyond the scope of this thesis. Compared to the electronic EAP, the ionic EAP are less suitable to robotic; they have a lower bandwidth and some of them suffer from permanent deformations if exposed to a constant signal. The use of ions in their operating principles decreases their driving voltage and increases their current consumption what is not desired in the MR environment.

This list of EAPs is not exhaustive please refer [Bar-Cohen 04] for more comprehensive informations about the EAP.

From the different EAPs, the EPAM has been used in two noticeable applications:

- It has been used to modify the shape of RF coils inside the scanner. The quality of the image obtained with this coil was good, proving the MR compatibility of the EPAM[Vogan 04].
- The *dielectric spring roll linear actuator* (Fig. 2.6(b)) has been developed for haptic interaction with the fingers [Zhang 06]. It is based on a spring around which an EPAM is rolled. This actuator can change its length by keeping the same output stiffness. This actuator has a length of 45 mm, a diameter of 8 mm, a maximum output force of 8 N and a maximum stroke of 5 mm.

By considering these two applications, the EPAM has a large potential for force-feedback applications in MR-environment. However, its muscle shape and its unidirectional output force make difficult its integration in a conventional force-feedback interface.

³Ferroelectric materials are a particular type of piezoelectric materials that show a spontaneous electric polarisation.

⁴To increase the magnetostriction effect, the polymer molecule is constituted of a flexible backbone on which polar groups are grafted.

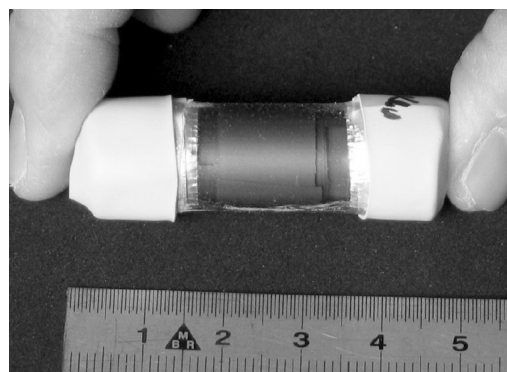
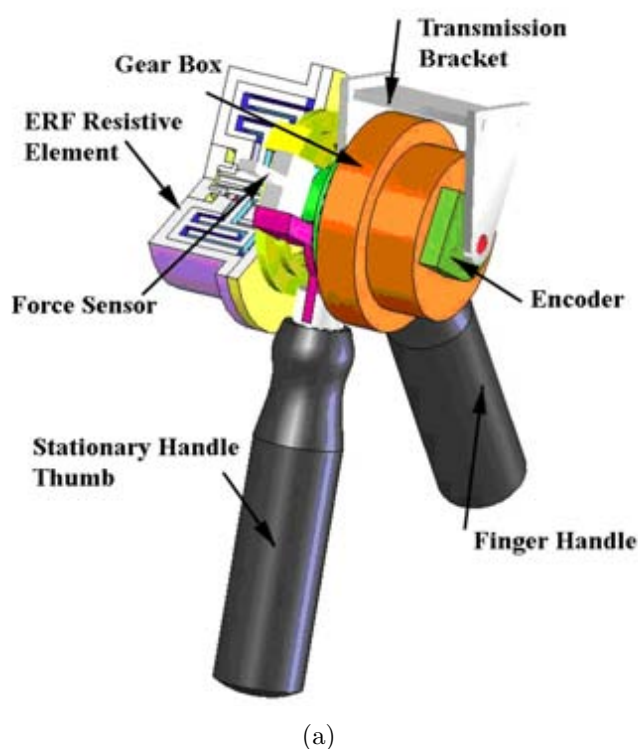


Figure 2.6: (a) Handle actuated by electrorheological fluid, reprinted from [Khanicheh 05]. (b) Dielectric spring roll linear actuator using EPAM, reprinted from [Zhang 06].

2.4 Conclusion

With the size reduction of interfaces, the actuation of haptic interface through a long transmission become less efficient. Then to keep good performance with interfaces for the fingers interaction, the actuator must be placed in the subject's hand area, then an actuator with a MR-compatible transduction principle is required.

To comply the MR-compatibility constraints, the electromagnetic interactions between the actuator and the scanner must be avoided. For its operation, the MR scanner uses a static magnetic field, switching field, magnetic fields and radio frequency pulses. They occupies almost the whole magnetic field spectrum and the high frequencies in the electrical field, leaving only the electrical field free from the low frequencies to the middle frequencies (several kHz) for the actuator operation. Thus the actuator must use a high voltage and low current transduction principle with driving signals below the very high frequency.

In addition to the MR-compatibility constraints, this actuator must be lightweight and force-controlled to achieve a good force interaction with the user. The reviewed MR-compatible actuators show poor performances for haptics:

- **ERF** actuators can only display resistive forces.
- **Electrostatic motors** and **USMs** are velocity controlled, lacking the ability to accurately display small forces.
- **EAPs** are too novel. The EPAM has interesting property, but its muscle shape and muscle behavior are not adapted to conventional haptic interfaces.

The lack of satisfying solutions explains the variety of actuation principles used for force-feedback in MR environments, compared to the surgical applications that mostly use USMs actuation. The USM also shows the most interesting characteristics for haptic interfaces:

- High torque and low speed characteristics
- Unlimited rotations
- Non-magnetic version readily available on the market

This thesis will investigate solutions based on the USM to actuate haptic interfaces in MR environments. These results may have a large impact, as USMs are widely used in the MR-compatible robotics.

Chapter 3

Ultrasonic Motor

3.1 Introduction

The ultrasonic motor is a particular type of piezoelectric actuator, where the piezoelectric ceramic is used to excite a mechanical body, the stator, close to its resonance frequency. These oscillations drive a rotor or slider pressed against the stator by the means of friction in an unidirectional movement. The vibration frequency is greater than the upper limit of human hearing ($> 20kHz$), thus the name called *ultrasonic motor*. There are both linear and rotary motor. The focus of this thesis is on the rotating motor, but the different principles presented below have also been applied to linear motors[Spanner 06].

3.1.1 History

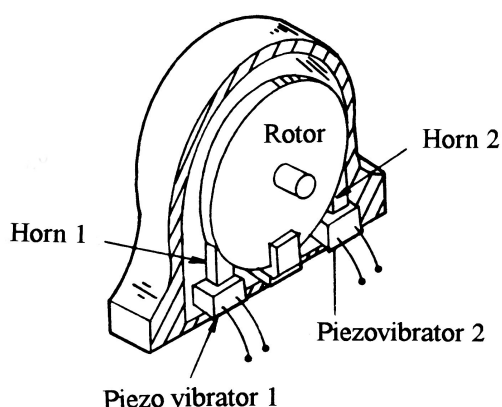
Standing Wave

The first ultrasonic motors used longitudinal standing waves on the stator. To transform the linear motion on the surface of the stator, different mechanisms were used.

The invention of the ultrasonic motor is attributed to V. Lavrinenko in 1965 at the Kiev Polytechnic Institute [Lavrinenko 65]. His motor was constituted of a piezoelectric plate applied on the circumference of a cylindrical rotor.

In 1973, H. V. Barth proposed his ultrasonic motor consisting of two vibrators pressed on the circumference of the rotor [Barth 73]. In the vibrator, piezoelectric ceramics induced a longitudinal vibration transmitted into a horn. The horn is a mechanical part that amplifies the vibration movements thanks to its decreasing section. The rotor motion was obtained through the difference between the direction of the vibration and the contact angle of the rotor with the vibrator. Barth's motor was equipped with two vibrators in order to drive the rotor in both directions. However, wear and tear prevented the practical use of this motor.

The first practical implementation of the USM was made by T. Sashida in his *wedge-type ultrasonic motor*[Sashida 93] in 1980. Several improvements were made compared to Barth's



Barth's motor, reprinted from [Ushino 97]

motor. In order to reduce the wear, the angle between the vibration direction of the horn and the surface of the rotor was decreased to 6° (Fig. 3.1(b)), limiting the slippage between the tips of the horn and the rotor. These tips were slanted to ensure a large contact surface with the rotor. This motor was able to reach high speeds of up to 3000rpm , thanks to the different mechanisms that amplified the piezoelectric ceramic motion. A Langevin's vibrator¹ was used and the small angle of the tips acted as a speed increaser between the longitudinal and tangential motion. This motor suffered from the wear of the tips.

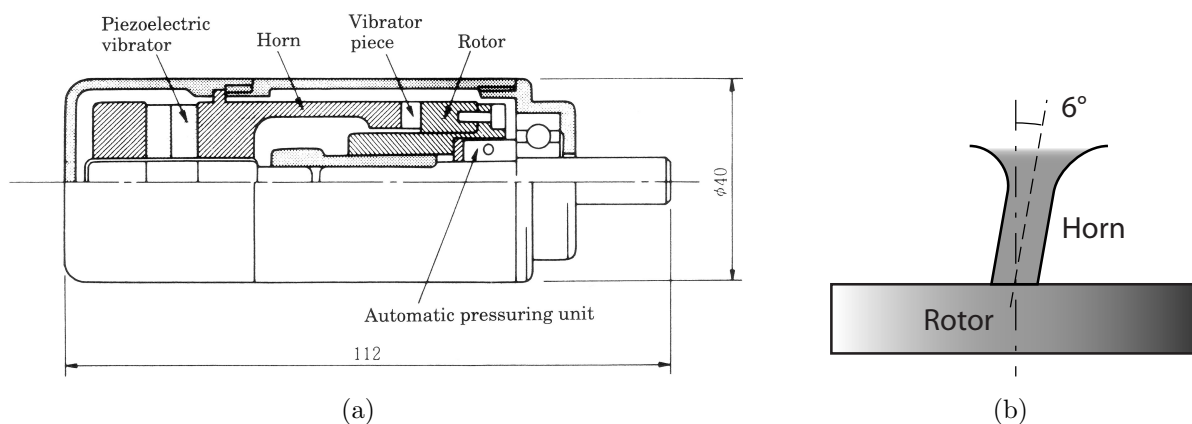


Figure 3.1: (a) Sashida's wedge type motor, reprinted from [Sashida 93], (b) inclination of the horn according the rotor axis.

In 1985, A. Kumada developed the PUREV motor (Piezo Ultrasonic Resonator with Elliptical Vibration) [Kumada 85]. It used a Langevin's vibrator to induce vibration in the

¹The Langevin's vibrator is a mechanical device used to amplify the longitudinal vibration of the piezoelectric ceramic. It is made of two piezoelectric plates stacked in the middle of two aluminium cylinders. The resonance frequency of the vibrator is given by its length that corresponds to the half length of the resonance wave. An additional horn could be used to further amplify the movement of the extremity.

axial direction of the motor. A part called *torsional coupler* was used instead of the slanted tips to transform the longitudinal movement in an elliptical motion. It consisted of a cylinder with a groove machined along its diameter on the side connected to the vibrator and a square beam on the other side. Due to the angle formed by the groove and the beam, the bending movements of the cylinder induced torsion into the beam, creating an elliptical motion on its extremities. A spring pressed the rotor against the square beam. This motor could rotate in both directions. However, to change the direction of rotation, the spring load on the rotor had to be adjusted, thus the direction could not be changed dynamically.

These motors used a standing wave in conjunction with an asymmetrical geometry to induce the elliptical movements of their tips, thus they could drive the rotor in only one direction. In order to have a bidirectional motor, S. Ueha added a supplementary torsional vibrator on the longitudinal vibrator in his *hybrid transducer type ultrasonic motor* [Kurosawa 91]. Thanks to longitudinal and torsional vibrators, the direction of the trajectory could be controlled in both directions, enabling change of the rotation direction of the motor.

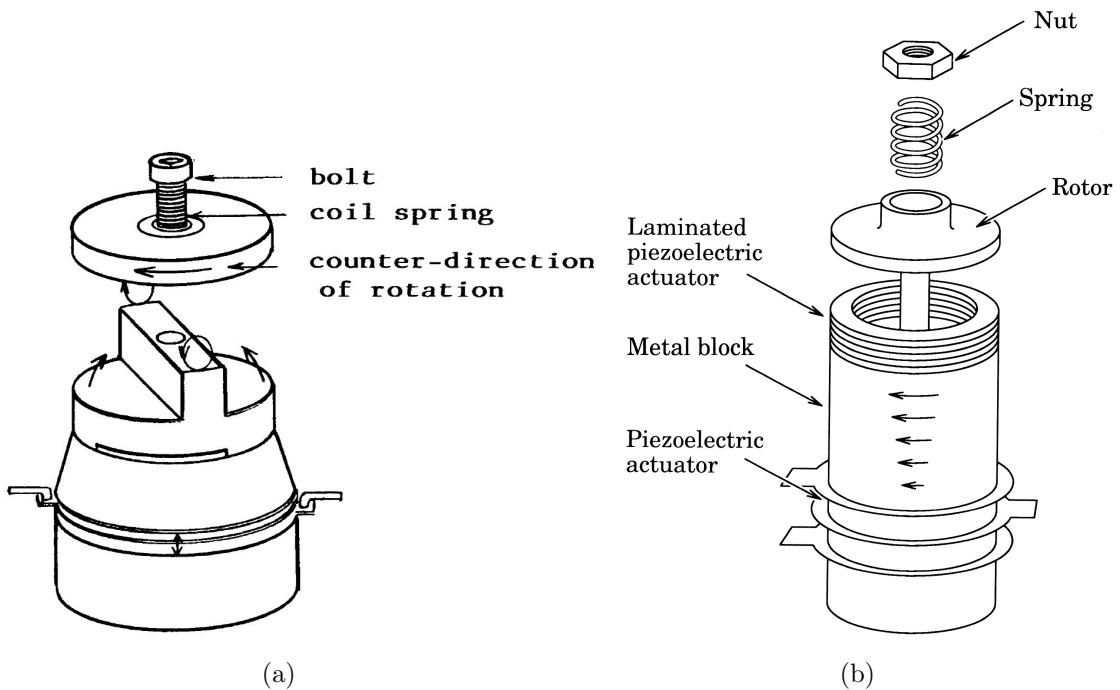


Figure 3.2: (a) Piezo Ultrasonic Resonator with Elliptical Vibration Motor, reprinted from [Kurosawa 91], (b) Hybrid transducer type ultrasonic motor, reprinted from [Sashida 93].

Traveling Wave

Standing wave ultrasonic motors have two drawbacks: the Langevin's vibrator is bulky and they are unidirectional or require a supplementary actuator in order to become bidirectional. The Traveling Wave Ultrasonic Motor (TWUSM) addresses these issues with a different operating principle that doesn't use longitudinal standing waves. In the TWUSM, the elliptical motion on the stator surface is created by a travelling wave resulting from the superposition of several standing waves. Compared to the standing wave motors, these motors are intrinsically bidirectional, the direction of rotation depends on the temporal phase between the standing waves constituting the travelling waves. The rotor and stator are constantly in contact, preventing impacts, and the contact points are distributed over the entire surface between the stator and the rotor. The wear on the rotor and the stator surface is reduced and the motor lifetime thereby extended.

In 1982, T. Sashida proposed the first TWUSM [Sashida 93]. In this motor, a ring shaped stator generated the bending travelling waves to drive the rotor plate axially pressed on the stator. This type of motor had a large industrial success thanks to its simplicity and compactness. The two motor phases are defined on the same piezoelectric plate. Its large torque and low speed characteristics allow using it in direct drive. T. Sashida founded Shinsei Corp., Japan in order to commercialize his motor. Most of the MR-compatible robotics groups use the non-magnetic version of the Shinsei's motors.

One of the most important applications of the TWUSM is the actuation of the autofocus mechanism of some camera lenses. Thanks to its ring shape, it is mounted around the lens. A more compact, more silent and faster solution compared to the previous motor and gears system. Canon Inc., Japan, introduced them first in its cameras in 1987.

Contact-less Motor

Until today developments are still made on the standing wave and travelling wave ultrasonic motor. In the 90's attempts were made to transmit the stator motion to the rotor without contact in order to reduce the wear, the main factor limiting the life of the USM. Fluid was first used as mean of transmission [Hu 95]. This USM consisted of a cylindrical stator filled with fluid, in the middle of which a rotor was floating. The travelling bending waves of the stator induced a stream in the fluid that drove the rotor.

This principle was also applied with air [Hu 97]. This motor was constituted of a cylindrical rotor inserted in a cylindrical stator. It used the travelling wave to induce an air stream in the gap. The rotor was driven by the stream and guided by acoustic levitation. This motor was able to rotate at high speeds up to 3000 *rpm*. The torque of this motor is very small, less than $2mNm$ with a 56 *mm* diameter rotor, because it is determined by the air friction on the rotor. The motor using air has the advantage of its simplicity: normal environments are filled with air and the acoustic levitation provides a contact-less guidance. This makes the linear version of this motor interesting for contact-less transportation applications [Ueha 00].

Conclusion

Ultrasonic motors were developed in order to take advantage of the properties of piezoelectric actuators, including high force and immunity to magnetic fields. They use several mechanisms in addition to the resonances to increase the movement amplitude of the piezoelectric actuator. The first USMs were standing wave motors, which are mainly unidirectional; an important limitation in haptics. The TWUSMs had a large industrial success thanks to their features: simple, compact, bidirectional and with a low speed and high torque output.

The latest ultrasonic motors are contact-less motors. These motors can only produce small torques, but thanks to the acoustic levitation, the linear version can be used for contact-less transportation. From the different types of USM, the TWUSM is the most adapted for applications in haptics thanks to its characteristics. Thus we will develop an actuator based on the travelling wave ultrasonic motor.

3.1.2 TWUSM Operating Principle

This section will focus on the operating principle of the TWUSM, as it makes its powering more complex than the other motors and creates some specific features. In the TWUSM the motion is created inside the stator. The rotor is a simple disc applied on the stator that is driven by friction.

The stator is an assembly of a piezoelectric ceramic plate and a metal ring. When a voltage is applied on the piezoelectric plate, the ceramic will contract or expand, creating with the metal ring the bending of the stator. The ceramic plate is poled alternatively, in order to obtain two standing waves of the same wavelength and spatially shifted by 90° . Two electrodes on each half side are used to control separately each phases. The standing waves can exist on the stator only if the circumference of the stator $2\pi r_m$ is equal to a multiple k of their wave length λ , where k is an integer called *mode order* as below:

$$k \lambda = 2\pi r_m \quad (3.1)$$

To know how the motion is created on the stator, a geometrical model can be used as proposed in [Pons 05]. The deformation of the stator is given by the vertical displacement of its *neutral plane* (the place in the stator where only bending occurs, without any elongation).

The deformation of a ring shaped stator as described in Fig. 3.5(a) and 3.5(b) by two standing bending waves of the same amplitude and with a spatial and temporal phase shift of $\frac{\pi}{2}$ rad can be expressed as a travelling wave thanks to a trigonometric transformation.

$$w(\phi, r, t) = A R(r) \cos(k\phi) \cos(\omega t) + A R(r) \sin(k\phi) \sin(\omega t) \quad (3.2)$$

$$= A R(r) \cos(\omega t - k\phi) \quad (3.3)$$

Where A is the amplitude of the wave, $R(r)$ is the amplitude of the wave along the radius and ω is the wave pulsation (Fig. 3.5(d)). To obtain a retrograde wave instead of a progressive

wave, the sign of one of the standing waves must be changed:

$$w(\phi, r, t) = A R(r) \cos(k\phi) \cos(\omega t) - A R(r) \sin(k\phi) \sin(\omega t) \quad (3.4)$$

$$= A R(r) \cos(\omega t + k\phi) \quad (3.5)$$

If we assume that the cross-section of the stator remains perpendicular to the neutral plane before and during the bending as shown in the Figs. 3.5(c) and 3.5(d), the movement of any points Q of the stator can be expressed from the Eq. 3.3:

$$\vec{u}_Q(\phi, r, z, t) = w \vec{e}_z - \frac{z}{r} \frac{\partial w}{\partial \phi} \vec{e}_\phi - z \frac{\partial w}{\partial r} \vec{e}_r \quad (3.6)$$

$$= A R \left(\cos(\omega t - k\phi) \vec{e}_z - \frac{kz}{r} \sin(\omega t - k\phi) \vec{e}_\phi - \frac{z}{R} \frac{\partial R}{\partial r} \cos(\omega t - k\phi) \vec{e}_r \right) \quad (3.7)$$

We can see that the point Q of the stator describes an ellipse, which will drive the rotor. There is also a radial motion coupled with the vertical motion and depending on the partial derivative of R . Practically, the width of the ring is small compared to its radius, so the derivative of $R(r)$ is small, thus the radial movement can be neglected.

The rotor is in contact with the most elevated points Q_c on the stator surface.

$$u_{Q_0}(\phi_0, r, z_0, t) \text{ is maximum for } \phi_0 = \frac{2m\pi + \omega t}{k} \text{ and } z_0 = h_{0b} \quad (3.8)$$

Where h_{0b} is the height of the stator surface from the neutral plane and m is an integer. The velocity of the point of the stator can be determined by deriving the displacement \vec{u}_Q with respect to time:

$$\vec{v}_Q(\phi, r, z, t) = \frac{\partial \vec{u}_Q}{\partial t} = A R \omega \left(-\sin(\omega t - k\phi) \vec{e}_z - \frac{kz}{r} \cos(\omega t - k\phi) \vec{e}_\phi \right) \quad (3.9)$$

If the rotor does not slip on the stator surface, its rotational speed is equal to the tangential speed of the contact point on the stator surface. Inserting the condition of 3.8 in the tangential term of the stator velocity 3.9, we can find the rotor angular velocity $\dot{\phi}_{rotor}$:

$$\dot{\phi}_{rotor} = \frac{A R k h_{0b}}{r^2} \omega \quad (3.10)$$

We can see that the rotor velocity depends directly on the travelling wave (in term of frequency, amplitude and mode number) and the stator geometry.

3.1.3 Characteristics

To drive the TWUSM, two alternative signals with a well defined frequency and phase shift are required. This is difficult to achieve due to the high voltage (at least one hundred volt) and

to the high frequency (several kilohertz) of these signals. The TWUSM has a high bandwidth; its response time is below 1 *ms*.

There are several phenomena in the TWUSM that the above model does not take into account, making its control more difficult. The rotor is pressed on the stator with a normal force to ensure the friction force between the rotor and the stator. If the output load is too high, the rotor will start to slip; this determines the *maximum output torque* of the TWUSM. The contact between the rotor and stator is not point-shaped. Usually an elastic lining material is placed on the rotor to prevent wear. Thus the rotor speed is lower than the stator maximum tangential speed. When the wave amplitude is too small, the contact between the lining material and the stator covers the entire stator surface, preventing the rotation of the rotor. The TWUSM has a *minimum speed* below which it blocks. A more complete model of the TWUSM, taking into account its dynamics as well as the stator and rotor interface is presented in [Hagood 95].

When the motor is turned off the friction between the rotor and the stator prevents the rotation of its output, the TWUSM has a *holding torque*. Thus the TWUSM is *non back-driveable*. These two last characteristics pose a safety issue, as large forces could appear when the output of the interface is blocked against a rigid obstacle and the *holding torque* will prevent releasing the blocked limb or interface output by disabling the power of the TWUSM.

Despite the presented difficulties, several attempts were made to use the TWUSM in haptic interfaces.

3.1.4 The TWUSM in Haptics

The largest difficulty that appears for any application with a TWUSM is its control. Its working principle which uses a cascaded resonant electrical and mechanical circuit, and the non linearities at the contact surface between the rotor and stator, make its control challenging. To vary the output velocity of the TWUSM, different parameters of the two input signals can be varied like their frequency, their amplitudes or their phases.

The first TWUSM drivers used phase modulation to control the output velocity. The phase signals of these drivers have a fixed amplitude and a phase between the input signal equal to $\frac{\pi}{2}$. A Proportional Integral (PI) controller is used to vary the driving frequency above the resonance frequency of the TWUSM in function of the velocity error. Near the resonance frequency, small frequency variations will induce large amplitude variations of the traveling wave and then large variation of the rotor velocity. This principle is still used in the drivers of Shinsei Corp. This relative simplicity is obtained in detriment of the performances. This driver suffers from limitations making the TWUSM inappropriate for haptics:

- They cannot reach velocity below a minimum value, also called *deadzone*, due to the stiction of the rotor and the stator for small wave amplitudes.
- The output velocity varies with the load and suffers from ripples.

- The characteristics of the TWUSM vary greatly with rising temperature. The friction between the rotor and the stator creates a significant heat.
- If overloaded, the motor blocks. This is called *pull-out* effect.

Normal Operating Conditions

These controllers use the normal operating conditions of the TWUSM and limit the slippage between the stator and the rotor. Usually, an inverse model or a look-up table determines the input parameters for the desired output velocity depending on the velocity of the TWUSM.

Tomonobu Senjyu did noticeable work on the control of the TWUSM. He investigated the problems in the position and speed control of the TWUSM. He focused on how to obtain a precise speed despite the load variation and the heating of the motor. In 1995, he proposed an adaptive controller using the frequency of the electrical input signals as control signal [Senjyu 95b] and in 1998 neural networks were used to reduce the computational power required by the adaptive controller [Senjyu 98]. In addition of the control of the frequency of the motor, he used the phase difference between the two driving signals to reach the low velocities required in position control [Senjyu 95a].

In 2000, Jurgen Maas proposed a controller able to control both speed and torque of the TWUSM [Maas 00]. It operates at the stator resonance frequency and varies the driving voltage and the phase delay between the two input signals. In his controller, the driving voltage is used to control the amplitude of the bending waves of the stator. The phase and the amplitude are not varied at the same time. The chosen set-point was : for high amplitudes, the phase between the input signals is equal to $\frac{\pi}{2}$ and their amplitudes are used to vary the velocity of the stator; at low speed, the amplitude of the bending wave is fixed to avoid stiction of the rotor, and the phase is used to modulate the rotor speed. In order to obtain a precise speed or torque output, an Inverse Contact Model (IMC) of the rotor on the stator is used. This is a lookup table that gives the speed and torque curves according to the set-point adjustment defined previously. With his controller, he performed impedance control on an active stick without a torque sensor. The maximum torque deviation was about 15 % of the maximum torque and was attributed to the temperature deviation.

F. Giraud proposed a controller using a fixed frequency and time phase between the input signals. To control the motor speed, the amplitude of the signal inputs was varied and the phase was controlled between the input signal and the bending waves to determine the resonance frequency and avoid the *pull-out* phenomenon [Giraud 04]. He controlled a force-feedback stick by admittance (Fig. 3.6(a)). The performances exhibit a 17 % overshoot with response time of 150ms. F. Giraud found that "the performance of this control is worse than those obtained with electromagnetic motors." He is currently continuing research in this area to compensate the friction of the TWUSM.

In [Flueckiger 05], a MR-compatible haptic handle (Fig. 3.6(b)) was developed. It uses a TWUSM controlled in admittance. The velocity of the motor is controlled by frequency. In

order to reach the smallest velocity, modulations of the input signal amplitude were used.

The most advanced MR-compatible haptic interface using a TWUSM is a two DOF manipulandum [Izawa 06] illustrated in Fig. 3.7(a). Impedance control was performed on the manipulandum. To control the output torque of the TWUSM, the phase between the two input signals of the TWUSM is varied according to an identified phase/torque/velocity map. This is a simplified approach of [Maas 00], as the signal input amplitudes are fixed.

The different control methods previously presented use the TWUSM in its normal operating method, where the slippage between the stator and the rotor is limited. These methods have a good power efficiency, however the control of the output torque is very difficult as it depends on the speed-torque curve of the TWUSM.

Slipping Rotor

A less usual approach is to allow slippage between the stator and the rotor to control the output torque. This idea was presented in 1995 by Makoto Kaneko [Kaneko 95]. By rapidly alternating the clockwise and counter clockwise direction rotation, it is possible to reduce the friction between the stator and the rotor by more than 10 times. A Pulse Width Modulation (PWM) is obtained by inserting a rest phase between the clockwise and counter clockwise command signal. With this PWM, the velocity of the TWUSM and the torque between the stator and rotor can be controlled independently of the velocity.

This principle was improved, instead to alternate with the clockwise and counter clockwise direction, the PWM/PS (Phase Selector) switch between a given direction (clockwise or counter clockwise) and a stationary wave mode which vertical motion limits the friction between the rotor and the stator. The stationary wave is obtained by canceling the phase shift between the two input signals. The PWM/PS was used to perform impedance control on a hand exoskeleton powered with TWUSM (Fig. 3.7(b)) [Choi 00].

The big issue with this control method is the wear between the stator and the rotor. With this control mode, the rotor slips continuously on the stator while the TWUSM is torque controlled, thus this control mode will reduce the lifetime of the TWUSM.

3.1.5 Conclusions

Only few haptic devices are actuated by a TWUSM due to the complexity of its controlling. Different methods have been tried in order to improve the velocity control or to allow the torque control of the TWUSM. Despite the sophisticated control schemes implemented these last years, the haptic performances of the TWUSM to render low impedance remain below those of the electromagnetic motor.

3.2 Electrical Analogy

In haptics, the interaction with virtual objects can be described by a force response to an applied movement or a movement response to a applied force. If these responses are linear with respect to the excitation, they can be described by their *mechanical impedance*. The notion of impedance comes from electricity and defines the relation between the voltage and the current in a linear circuit. Control algorithms like impedance or admittance control have been developed to control robots in mechanical interaction with their environment, such as haptic interfaces. These algorithms stated that control loops modify the impedance of the controlled systems. Then in order to have optimal performances with an haptic interface, its mechanical impedance must be considered during its mechanical design. The system can be expressed with its *electrical equivalent*: this representation enables us to apply tools and concepts used in the electricity.

3.2.1 Principle

The electrical analogy is based on the principle that the power is preserved from a domain to another. In all domains, the *power* is the product of an *effort* and a *flow*:

Electricity the voltage is the effort and the current is the flow.

Mechanic the force is the effort and the velocity is the flow.

This is the direct analogy. A dual representation of *effort* and *flow* exists. Because we are interested to the output force of the device and in electricity most of the circuit output voltage, a force-tension analogy is more appropriate to describe the system. An other advantage of this representation is that the electrical equivalent impedance complies with the definition of the mechanical impedance presented in the subsection 2.1.2. For these reasons, the direct (force-tension) analogy will be used in this thesis.

As proposed in [Lauria 07], the actuators can be represented as variable mechanical power sources and the mechanical components as electrical components. By using the equivalent *flow* and *effort*, a discrete mechanical model can be transformed into an equivalent electrical circuit.

Table 3.1: Equivalent flows and efforts

Mechanical		Electrical	
Value	Unit	Value	Unit
f force	$[N]$	u voltage	$[V]$
v velocity	$[m/s]$	i current	$[A]$

Masses, dampers and springs have their electrical equivalents respectively inductors, resistors and dampers. These relations are summarized in Table 3.2.

Table 3.2: Equivalent components

Mechanical			Electrical		
Value	Unit	Law	Value	Unit	Law
I inertia	$[kg]$	$f = M \frac{dv}{dt}$	L inductor	$[H]$	$u = L \frac{di}{dt}$
K stiffness	$[Nm^{-1}]$	$f = K \int v dt$	C capacitor	$[F]$	$u = \frac{1}{C} \int i dt$
D viscosity	$[Nsm^{-1}]$	$f = Dv$	R resistor	$[\Omega]$	$u = Ri$

The force source imposes its output force independently from the output velocity, and the velocity source imposes a velocity independently from the output force. Other components will be introduced later, when required.

The Newton's law and the kinematic constraints in the mechanical system become the Kirchhoff's laws in the circuit (Table 3.3). With the equivalent elements and laws, it is then

Table 3.3: Equivalent laws

Mechanical	Electrical
<p>Newton's second law $\sum \vec{f}_{ext} = M\vec{a}$ The product of a mass M times its acceleration \vec{a} is equal to the sum of the external forces \vec{f}_{ext} applied on it.</p>	<p>Kirchoff's voltages law $\sum u = 0$ The sum of the voltages u on a closed-loop is equal to zero.</p>
<p>Relative velocity $v_{a b} = v_{b 0} - v_{a 0}$ The relative velocity of b with respect of a $v_{b a}$ is equal to the difference of the absolute velocity of b $v_{b 0}$ with the absolute velocity of a $v_{a 0}$.</p>	<p>Kirchoff's currents law $\sum i = 0$ The sum of the currents i on a node is equal to zero.</p>

possible to transform any linear discrete mechanical model into its electrical equivalent circuit (Fig. 3.8). To avoid the introduction of additional values and to keep the relations with the mechanical system, the equivalent electrical circuit will be expressed in mechanical terms with the electrical symbols.

3.2.2 USM Models

As seen in the previous section, the behavior of the USM and particularly the TWUSM is complex. Because the goal of this thesis is not to improve the USM performances by control, a complex USM model is not needed. The required USM model must show the main USM limitations such as the minimum velocity or the holding torque. The USM will be modeled

with linear mechanical components and non-linearities will be expressed in term of velocity and force ranges.

Mechanical Model

Because the contact between the stator and the rotor is completely different depending on the USM operating states, two cases must be distinguished in the USM model:

USM ON , The stator of the USM can be considered as a variable velocity source v_{in} driving through viscous friction D_{usm} the rotor modelled by an inertia I_{usm} (Fig. 3.9a):

$$I_{usm}\dot{v}_{usm} = -D_{usm}(v_{usm} - v_{in}) - f_{usm} \quad (3.11)$$

where f_{usm} is the output force of the USM and v_{usm} is the rotor velocity. In order to take the USM limitations into account, v_{in} is limited to the USM velocity range:

$$v_{usm_{min}} \leq |v_{in}| \leq v_{usm_{max}} \quad (3.12)$$

The friction between the stator and rotor determines the maximum USM output force $f_{usm_{max}}$:

$$|f_{usm}| \leq f_{usm_{max}} \quad (3.13)$$

USM OFF When the motor is switched off, the rotor is applied on the whole stator surface, then a holding force f_{hold} prevents rotor motions. If the force applied on the output of the USM f_{usm} is smaller than the holding force f_{hold} , the rotor is locked (Fig.3.9b):

$$v_{usm} = 0 \quad \text{if } |f_{usm}| \leq f_{hold} \quad (3.14)$$

Although the behavior of the *USM ON* is the most important, the behavior of the *USM OFF* will be considered for safety issues. In the model of the *USM ON*, the input velocity v_{in} is considered as an ideal velocity source. The stator dynamics is high enough to be neglected in the model.

Electrical Equivalent

The electrical equivalent circuit of the *USM ON* (Fig. 3.9a) can be built from the mechanical model of the USM. The input velocity is represented by a velocity source v_{in} . The friction D_{usm} mechanically in series with v_{in} is added in parallel to the circuit. The rotor inertia I_{usm} moving with the output is then added on the output branch.

With the *USM OFF*, the holding force f_{hold} locks the rotor, then the real source constituted of the velocity source v_{in} and its output resistor D_{usm} is changed by an open circuit (Fig. 3.9b).

Models Parameters

The USM used in this research is a USR30 (Shinsei Corporation Inc., Japan). The different parameters used in the mechanical and electrical models of this motor are given in the data sheets (Table 3.4) except for the rotor inertia I_{usm} and the viscous friction D_{usm} .

Table 3.4: USR30 specifications given by the data sheets

Minimum velocity	$[rad/s]$	$v_{usm_{min}}$	1.57
Maximum velocity	$[rad/s]$	$v_{usm_{max}}$	31.4
Maximum force	$[Nm]$	$f_{usm_{max}}$	0.100
Rated force	$[Nm]$	$f_{usm_{rated}}$	0.050
Rated velocity	$[rad/s]$	$v_{usm_{rated}}$	26.18

I_{usm} is calculated from the rotor geometry and its material density. The viscous friction D_{usm} between the rotor and the stator can be identified from the slope of the steady state torque velocity curve; this curve is obtained by canceling the acceleration term in Eq. 3.11.

$$f_{usm} = -D_{usm}(v_{usm} - v_{in}) \quad (3.15)$$

D_{usm} is the slope of the force-velocity curves. The curve given in the data sheets is a truncated triangle at the maximum force $f_{usm_{max}}$ and doesn't have a constant slope in the slanted part. Because the USM limitation is in the output of small forces, D_{usm} will be determined for low force values. The force velocity curve is the line going from the "zero force"- "maximum velocity" point **c** to the "rated force"- "rated velocity" point **b** (Fig. 3.10):

$$D_{usm} = \frac{f_{usm_{max}} - f_{usm_{rated}}}{v_{usm_{max}} - v_{usm_{rated}}} \quad (3.16)$$

The theoretical minimum force $f_{usm_{min}}$ with the USM fixed end is determined from Eq. 3.15. The force dynamic range is the ratio of the full output range with the output force resolution. In the case of the USM, the needed range is from a null force to $f_{usm_{max}}$, the USM range is equal to the value $f_{usm_{max}}$. In this range, the force resolution is limited by the USM minimum force. Then the USM force dynamic range is the inverse of the USM relative minimum force. Its force dynamic range is small less than 7 for the USR30. The identified parameters of the USR30 have been summarized in 3.5.

The force-velocity curves of the model have been reported in Fig.3.10 (the hatched area). The model matches well the characteristics of the USR30, excepted for high forces and low velocities. In the specifications, the USM can not reach velocity lower than $v_{usm_{min}}$. Experimentally, lower values have been reached by applying a load on the USM, thus $v_{usm_{min}}$ is the minimum no-load velocity.

Table 3.5: USR30 calculated parameters

Rotor inertia	$[kgm^2]$	I_{usm}	$2.3 \cdot 10^{-7}$
Rotor friction	$[Nms/rad]$	D_{usm}	$9.5 \cdot 10^{-3}$
Minimum force	$[Nm]$	$f_{usm_{min}}$	0.015
Force dynamic range	$[]$		6.7

3.2.3 Thevenin's Equivalent

In haptic interfaces, the user's load may vary in a wide range making it difficult to determine the output force of the system. It is then easier to determine the output force of the haptic interface in function of the output velocity. The Thevenin's theorem states that any linear electrical system with two terminals can be expressed with its Thevenin's equivalent consisting of a voltage source with the open-circuit voltage in series with the internal impedance of the electrical system considered. For harmonic sources with a pulsation ω , complex impedances can be used. By using the electrical analogy, it can be applied to any linear 1 DOF mechatronic system:

$$\underline{F}_{out}(j\omega) = \underline{F}_{th}(j\omega) - \underline{Z}_{out}(j\omega)\underline{V}_{out} \quad (3.17)$$

Where \underline{F}_{th} is the output force when the system output is locked, \underline{Z}_{out} is the mechanical impedance of the system and \underline{V}_{out} is the output velocity. The mechanical output impedance $\underline{Z}_{out}(j\omega)$ is defined as:

$$\underline{Z}_{out}(j\omega) = -\frac{\underline{F}_{out}}{\underline{V}_{out}} \quad \text{with } \underline{F}_{th} = 0 \quad (3.18)$$

It is obtained with the system impedance seen from the output with the cancelled sources (the force sources become short circuits and the velocity sources become open circuits). The Norton's equivalent is the dual representation of Thevenin's equivalent; the system is assimilated to a real velocity source:

$$\underline{V}_{out}(j\omega) = \underline{V}_{no}(j\omega) - \frac{\underline{F}_{out}}{\underline{Z}_{out}(j\omega)} \quad (3.19)$$

where \underline{V}_{no} is the output no-load velocity. \underline{F}_{out} is the output force. The mechanical output impedance $\underline{Z}_{out}(j\omega)$ is the same than the one of Thevenin's equivalent.

Because in the mechatronic systems, the actuators are variable sources of force f_{in} or velocity v_{in} , \underline{F}_{th} can be expressed with the transfer function of the system with the locked output $\underline{H}_{th}(j\omega)$.

$$\underline{F}_{out}(j\omega) = \underline{H}_{th}(j\omega)\underline{F}_{in} - \underline{Z}_{out}(j\omega)\underline{V}_{out} \quad (3.20)$$

Then the output force of the system in function of the output velocity can be expressed with \underline{H}_{th} and \underline{Z}_{out} . This expression 3.20 of output force \underline{F}_{out} has the particularity of decoupling the influences of the input source \underline{F}_{in} and the output velocity \underline{V}_{out} . \underline{H}_{th} is the forward transfer function and should have a small phase, high gain and high bandwidth. \underline{Z}_{out} determines the sensibility of the output force \underline{F}_{out} to the output velocity variation. If the output impedance is low, the system must be considered as a force source. If its output impedance is high, its output velocity is almost not sensitive to the force variations, the system must be rather considered as a velocity source.

These complex functions can be expressed with Laplace's transform by replacing $j\omega$ by s (Fig. 3.11).

3.2.4 Comparison with a DC Motor

The complex frequency response of the *USM ON* output force \underline{F}_{usm} can be determined with the Thevenin's equivalent.

$$\underline{F}_{usm}(j\omega) = \underline{H}_{usm}(j\omega)\underline{V}_{in} - \underline{Z}_{usm}(j\omega)\underline{V}_{usm} \quad (3.21)$$

where \underline{H}_{usm} is the USM transfer function with the fixed end and \underline{Z}_{usm} is the output impedance. They can be derived from the Eq. 3.11 expressed with the complex exponentials.

$$\underline{H}_{usm}(j\omega) = \frac{\underline{F}_{usm}(j\omega)}{\underline{V}_{in}} = D_{usm} \quad (3.22)$$

$$\underline{Z}_{usm}(j\omega) = j\omega I_{usm} + D_{usm} \quad (3.23)$$

This response can be compared to the response of a DC motor whose equation of motion is:

$$I_{dc}\dot{v}_{dc} = -D_{dc}v_{dc} + f_{in} - f_{dc} \quad (3.24)$$

where v_{dc} is its output velocity, I_{dc} is the rotor inertia, D_{dc} is the influence of the counter electromotive force on the output force and f_{in} and f_{out} are respectively the input and output force. Its complex transfer function $\underline{H}_{dc}(j\omega)$ with the fixed end and the output impedance $\underline{Z}_{dc}(j\omega)$ are then:

$$\underline{H}_{dc}(j\omega) = \frac{\underline{F}_{dc}(j\omega)}{\underline{F}_{in}} = 1 \quad (3.25)$$

$$\underline{Z}_{dc}(j\omega) = j\omega I_{dc} + D_{dc} \quad (3.26)$$

The transfer functions of the USM and the DC motor are constant with a different gain due to their different inputs type, however the expressions of their output impedances are similar. In order to understand the difference which makes difficult to control the USM output force, the output impedance of the USM and DC motors with similar rated torque will be evaluated

and compared in Fig. 3.12. The USM is the USR30 and the DC motor is a DC-Micromotor Series 2342024CR (Micromotor SA, Switzerland). The USM and DC motor specifications are summarized respectively in the Table 3.4 and in the Table 3.6.

The output impedance of the USM is about 100 higher than that of the DC motor, this is due to the very high rotor friction D_{usm} . Compared to the DC motor, the USM output is then sensitive to the output velocity. The USM is mechanically more suitable to control its output velocity and must then be considered as a real velocity source rather than a force source. The output impedance of the USM must be decreased to improve the control of the USM output force.

Table 3.6: DC-Micromotor Series 2342024CR specifications given by the data sheets

Rotor inertia	$[kgm^2]$	I_{dc}	$5.8 \cdot 10^{-7}$
Rotor friction	$[Nms/rad]$	D_{dc}	$9.6 \cdot 10^{-5}$
Maximum force	$[Nm]$	$f_{dc,max}$	0.085

3.3 Conclusion

The first USM was presented in the sixties in order to take advantage of the piezoelectric actuators features in a motor, such as high torque/low speed characteristic and magnetic immunity. Until the nineties the research focused on the hardware developments of the USM, in order to simplify the mechanism and to reduce wear between the rotor and the stator thereby improving longevity. The invention of the traveling wave ultrasonic motor addressed most of the hardware expectations, and further development on the USM mainly focused on the control.

The motor is a cascaded resonating electromechanical system that drives a rotor by friction. Thus the dynamic behavior of the USM is very difficult to model and its numerous control parameters make it even more difficult to control. The haptic rendering obtained with a USM is still not satisfactory compared to that achieved with electromagnetic motors.

To explain its poor performances in force control, a mass damper model of the USM has been developed and its limitations described in terms of force and velocity ranges. This model has high output impedance making the output force very sensitive to the output motion. From the electrical analogy, the USM must rather be considered as a velocity source. Its high output impedance combined with its small force velocity range limits the USM force dynamic range: for the USR30 the calculated dynamic range is less than 7. Thus to improve its performance in force control, its output impedance must be decreased, and its force dynamic range must be improved.

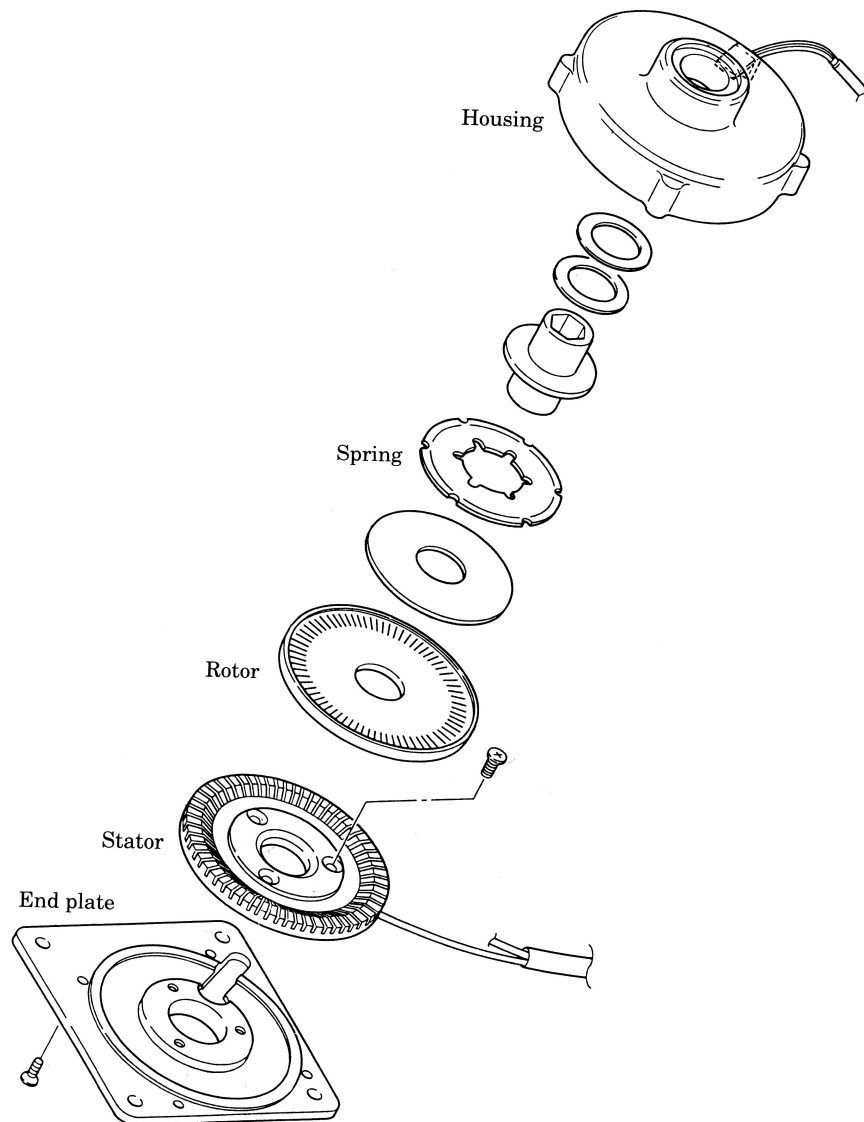


Figure 3.3: A exploded view of a Travelling Wave Ultrasonic Motor, reprinted from [Sashida 93]

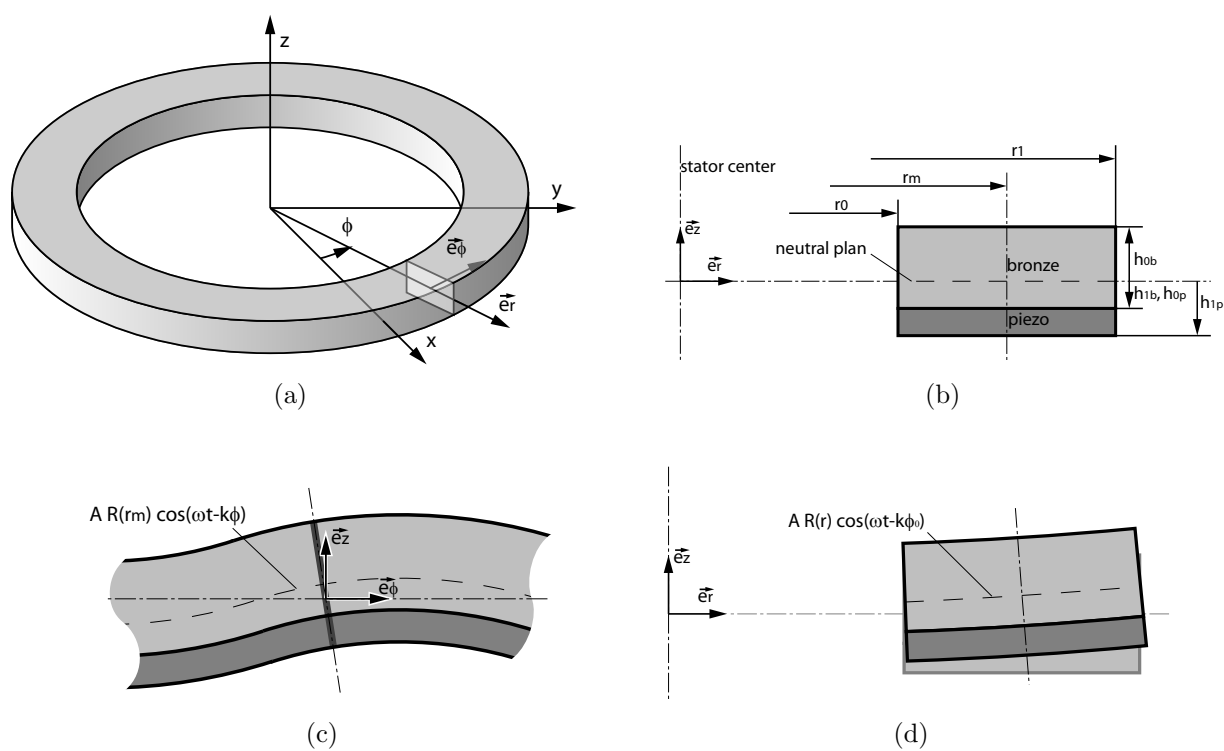


Figure 3.5: (a) Coordinates used to describe the stator. (b) Parameters of the stator section. (c) Side view of the displacement of the stator section due to the bending. (d) Front view of the displacement of the stator section due to the bending.

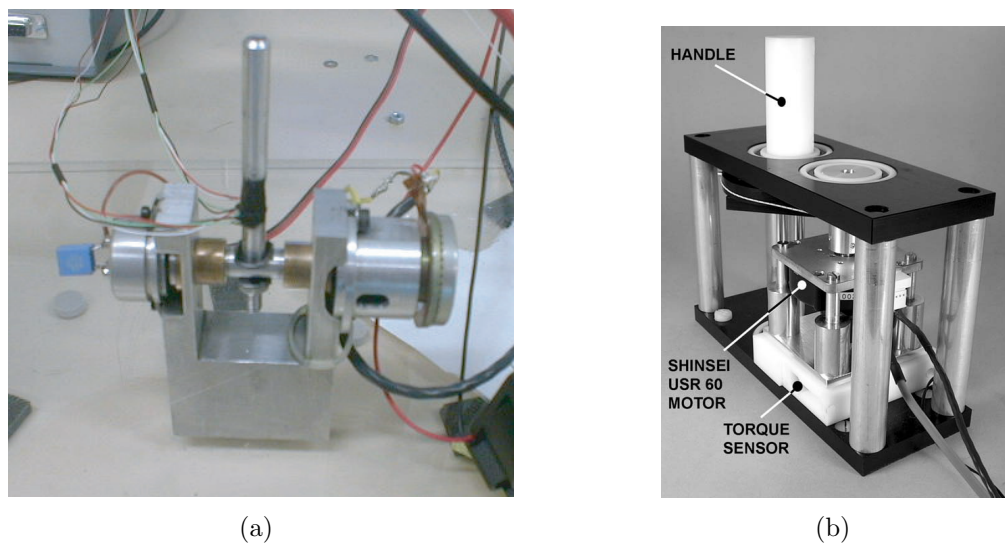


Figure 3.6: Haptic interfaces actuated by a TWUSM and used in admittance control. (a) Active stick, reprinted from [Lemaire-Semail 07]. (b) MR-compatible handle, reprinted from [Flueckiger 05].

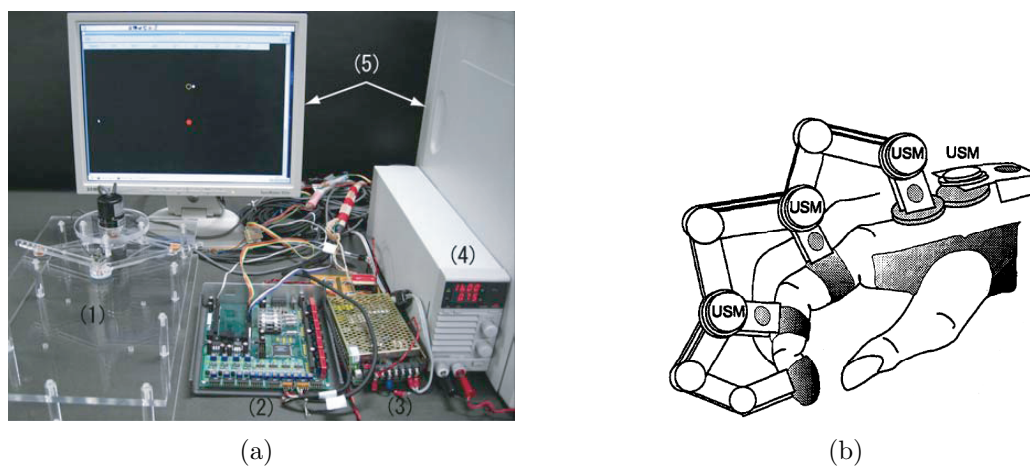


Figure 3.7: (a) MR-compatible 2 DOF manipulandum actuated by a TWUSM reprinted, from [Izawa 06], (b) Illustration of the SKK handmaster, reprinted from [Choi 99].

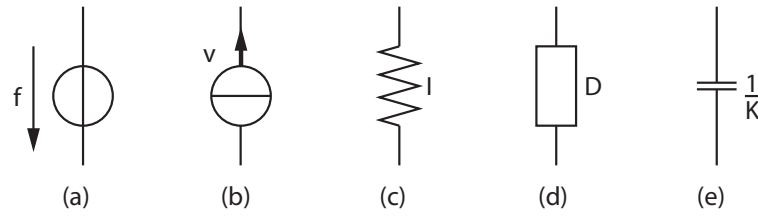


Figure 3.8: Electrical symbols used to express mechanical values: (a) the force source f , (b) the velocity source v , (c) the inertia I , (d) the viscous damper D and (e) the spring K .

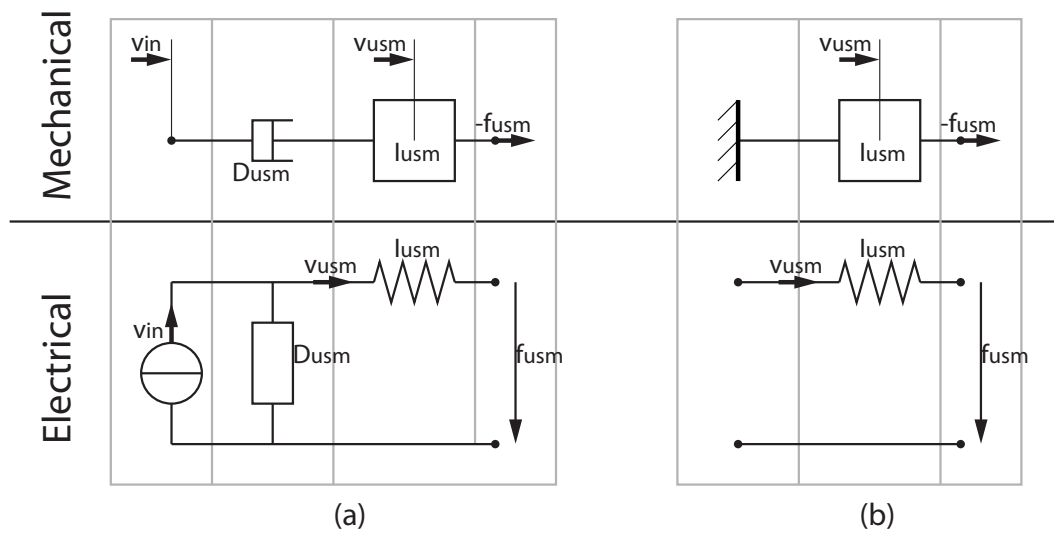


Figure 3.9: Mechanical model and its equivalent circuit of the *USM ON* (a) and *USM OFF* (b). The mechanical model is a translational model, where the different components can move only along the horizontal direction.

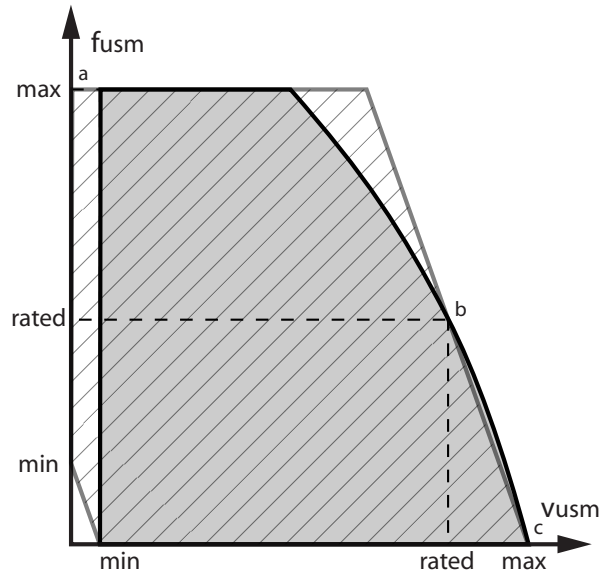


Figure 3.10: Steady states force-velocity curves of the USM (plain) and its linear model (hatched).

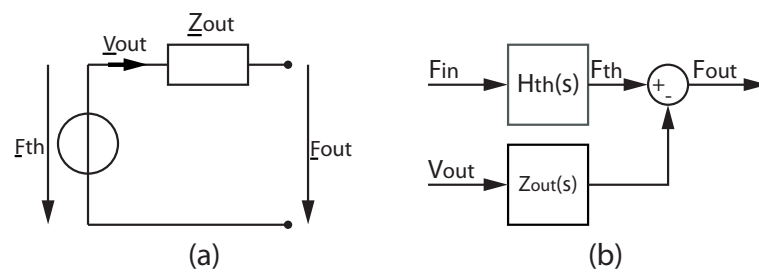


Figure 3.11: Thevenin's equivalents expressed in a circuit with complex impedances (a) and in a blocks diagram with Laplace transforms (b).

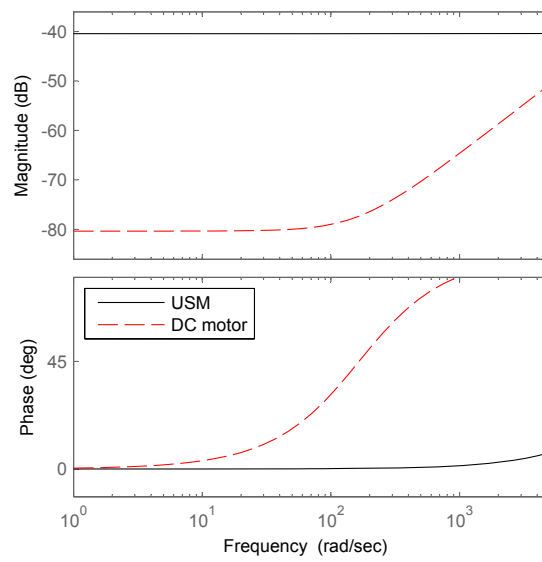


Figure 3.12: Bode plots of the output impedances of the USM and the DC motor.

Chapter 4

Proposed Mechanisms

In this chapter, different mechanical solutions will be investigated to cope with the USM limitations like the minimum velocity and to decrease the USM output impedance. These modifications must also improve the safety for the user by limiting the output force and by addressing the blocking hazards due to the USM holding force. These modifications will be evaluated with the USM linear model of section 3.2.

4.1 Series Dynamics

The *series dynamics* is a solution developed for geared DC motors used in walking robots, where geared DC motors have characteristics similar to the USM, such as a high force and a high output impedance, making difficult the control of their output force.

The idea in the series dynamics is to add a low impedance component, like a spring or a viscous damper, in series on the output to decrease the output impedance of the whole system [Hogan 04]. In the equivalent circuit, this is similar to add a component in parallel to the output (Fig. 4.1).

The goal of the series dynamics is to improve the output force control and prevent force peaks in the gears when shocks occur; Applied to USMs this solution should also improve the safety.

4.1.1 Spring

The Series Elastic Actuator (SEA) is the first series dynamics actuator. It has been proposed by G.-A. Pratt in 1995 and consists of adding a spring between the load and the output of the gear [Pratt 95] (Fig 4.1a). The motion of the output of the SEA is determined by the motion equations of the USM (Eq. 3.11) and the equation of the spring :

$$\begin{cases} I_{usm}\ddot{x}_{usm} &= -D_{usm}(\dot{x}_{usm} - v_{in}) - K_{sea}(x_{usm} - x_{sea}) \\ 0 &= -K_{sea}(x_{sea} - x_{usm}) - f_{sea} \end{cases} \quad (4.1)$$

Where K_{sea} is the stiffness of the added spring. x_{usm} is the position of the USM output. x_{sea} and f_{sea} are respectively the output position and force of the SEA. To output a force on the SEA, the USM position must be set in order to load the spring.

Steady States

The steady state characteristic of the SEA is the solution of the Eq. 4.1 with constant velocities:

$$f_{sea} = -D_{usm}(\dot{x}_{usm} - v_{in}) \quad (4.2)$$

The steady state characteristic of the SEA is the same as the USM (Fig. 4.2 hatched area), thus in steady state, the SEA and the USM have the same speed range.

$$\begin{cases} v_{sea_{min}} = v_{usm_{min}} \\ v_{sea_{max}} = v_{usm_{max}} \\ f_{sea_{min}} = f_{usm_{min}} \\ f_{sea_{max}} = f_{usm_{max}} \end{cases} \quad (4.3)$$

In the previous solution $f_{sea_{min}}$ is the asymptotic solution for $v_{in_{min}}$. The SEA can achieve smaller forces with its fixed output $\dot{x}_{sea} = 0$. The minimum force achievable $f_{sea_{min}}$ is determined by the smallest achievable position increment $\Delta x_{usm_{min}}$ and the stiffness K_{sea} :

$$f_{sea_{min}} = K_{sea} \Delta x_{usm_{min}} \quad (4.4)$$

A small position increment can be achieved by using a short impulsion on the USM signal command u_{usm} and the holding force f_{hold} to lock the output of the USM. Because $\Delta x_{usm_{min}}$ depends on many parameters and many phenomena, it has been identified experimentally. With the USR30, equipped with a 500cpr encoder used in quadrature, $\Delta x_{usm_{min}}$ is equal to $3.14 \cdot 10^{-3} \text{ rad}$, the resolution of the encoder. To improve the minimum force achievable with the SEA, K_{sea} must be low enough to fulfill this condition:

$$K_{sea} < \frac{f_{usm_{min}}}{\Delta x_{usm_{min}}} \quad (4.5)$$

In this specific case, the $\Delta x_{usm_{min}}$ is very small, then this condition can be fulfilled.

Forward Transfer Function and K_{sea}

The spring K_{sea} limits the SEA open-loop bandwidth ω_{sea} , this can be verified on the SEA electrical equivalent (Fig. 4.1a) where K_{sea} behaves like a short circuit at high-frequency. The open-loop bandwidth of the SEA ω_{sea} is given by the SEA transfer function with the fixed

end. With $x_{sea} = 0$, the SEA becomes a damped oscillator. The forward transfer function of the SEA H_{sea} is derived from the Laplace transform of Eq. 4.1:

$$H_{sea}(s) = \frac{F_{sea}}{V_{in}} = \frac{K_{sea}D_{usm}}{I_{usm}s^2 + D_{usm}s + K_{sea}} \quad (4.6)$$

The spring constant K_{sea} can be then chosen in function of the open-loop bandwidth ω_{sea} . Because the SEA controller set the actuator force proportionally to the spring deflection, in closed-loop the apparent stiffness of the SEA is increased and its bandwidth too [Robinson 99].

The bandwidth ω_{sea} is determined with the pole of H_{sea} with the smallest norm. The difficulty is the expression of this pole changes depending if the system is under- or over-damped. We propose a method to get the K_{sea} knowing the I_{usm} , D_{usm} and ω_{sea} derived from the expressions of the oscillator given in [Del Pedro 97]. For this, the damping factor λ , the natural angular frequency ω_0 and the damped natural angular frequency ω_1 must be introduced:

$$\begin{cases} \omega_0 = \sqrt{\frac{K_{sea}}{I_{usm}}} \\ \lambda = \frac{D_{usm}}{2I_{usm}} \\ \omega_1^2 = |\lambda^2 - \omega_0^2| \end{cases} \quad (4.7)$$

where ω_1 is always positive. Then the smallest roots norm can be expressed:

$$\omega_{sea} = \begin{cases} \omega_{under} = |-\lambda \pm j\omega_1| & \text{if under-damped} & \lambda < \omega_0 \\ \omega_{critical} = |-\lambda| & \text{if critically-damped} & \lambda = \omega_0 \\ \omega_{over} = |-\lambda + \omega_1| & \text{if over-damped} & \lambda > \omega_0 \end{cases} \quad (4.8)$$

where ω_{under} , $\omega_{critical}$ and ω_{over} are respectively the smallest roots norm of the under-damped, critically-damped and over-damped oscillator. For a given λ , they have this following properties:

$$\omega_{over} < \omega_{critical} < \omega_{under} \quad (4.9)$$

This allows the determination of the oscillator type by comparing ω_{sea} with λ that is equal to $\omega_{critical}$.

In the case of the USR30, the desired open-loop bandwidth is chosen for example $\omega_{sea} = 2\pi 50 \text{ rad/s}$, and the USR30 damping factor is $\lambda = 2.07 \cdot 10^4 \text{ rad/s}$. Because ω_{sea} is smaller than λ , the SEA powered with a USM must be an over-damped oscillator to comply with the desired bandwidth. The minimal stiffness K_{sea} can be derived from the expression of the root norm of the over-damped oscillator ω_o (4.8) and the desired SEA bandwidth ω_{sea} :

$$\omega_{sea} = |-\lambda + \sqrt{\lambda^2 - \omega_0^2}| \Rightarrow K_{sea} = I_{usm}(2\lambda\omega_{sea} - \omega_{sea}^2) = 2.97 \text{ Nm/rad} \quad (4.10)$$

In our case, λ is much larger than ω_{sea} then the solution for the spring can be approximated:

$$\omega_{sea} \ll \lambda \Rightarrow K_{sea} \simeq 2I_{usm}\lambda\omega_{sea} = D_{usm}\omega_{sea} \quad (4.11)$$

This result corresponds in the electrical analogy to the time constant RC of a capacity discharging through a resistor.

The bode plot of the SEA can be obtained by replacing the variable s by $j\omega$ in the transfer functions H_{sea} . The transfer function of the SEA has been evaluated for the USR30 parameters with a desired open-loop bandwidth $\omega_{sea} = 2\pi 50 \text{ Hz}$. The SEA transfer function H_{sea} is a low pass filter (Fig. 4.3(a)). Thanks to the high value of D_{usm} , the SEA has no resonance mode. The SEA actuated by a USM is thus more stable (an over-damped system) than the SEA actuated by a DC motor without gearbox (an under-damped system).

Output Impedance

The output impedance Z_{sea} is obtained by canceling the input v_{in} in Eq. 4.1:

$$Z_{sea} = -\frac{F_{sea}}{sX_{sea}} = K_{sea} \frac{I_{usm}s + D_{usm}}{I_{usm}s^2 + D_{usm}s + K_{sea}} \quad (4.12)$$

Z_{sea} is equal to the USM output impedance Z_{usm} in parallel with K_{sea}/s . The bode plot of the SEA impedance Z_{sea} is given in Fig. 4.3(b). The impedance magnitude is only decreased at high frequencies. In the low frequencies, it remains equal to D_{usm} , the USM impedance. Because the forward transfer function H_{sea} has the same poles than the output impedance Z_{sea} , their cutoff frequencies are the same.

Safety

In normal operating conditions, the added spring decreases force peaks, but it can not be used to limit the output torque at low frequencies.

When the motor is turned off $\dot{x}_{usm} = 0$, the output force of the SEA is determined by the compression of the spring:

$$f_{sea} = -K_{sea}(x_{sea} - x_{usm}) \quad (4.13)$$

A force may remain after turning off the USM, however if this force can be overcome, the output can be moved thanks to the compliance of the spring. The SEA is safer compared to the USM, but its *power off state* is not safe, because forces may remain on the output.

Conclusion

The SEA applied to the USM is a simple solution to improve the force output; however these improvements concern mainly the case where the output of the SEA is locked. In the case where a precise force must be applied with the moving output, the speed range of the USM will limit the accuracy of the output force. The second drawback of this method is that the minimum force is decreased in detriment of the output bandwidth.

4.1.2 Damper

Instead of using a spring, a viscous damper can be added between the motor and the load (Fig. 4.1b). The idea of the Series Damper Actuator (SDA) has been proposed by C.-M. Chew in 2004 [Chew 04]. The SDA can be applied to the USM.

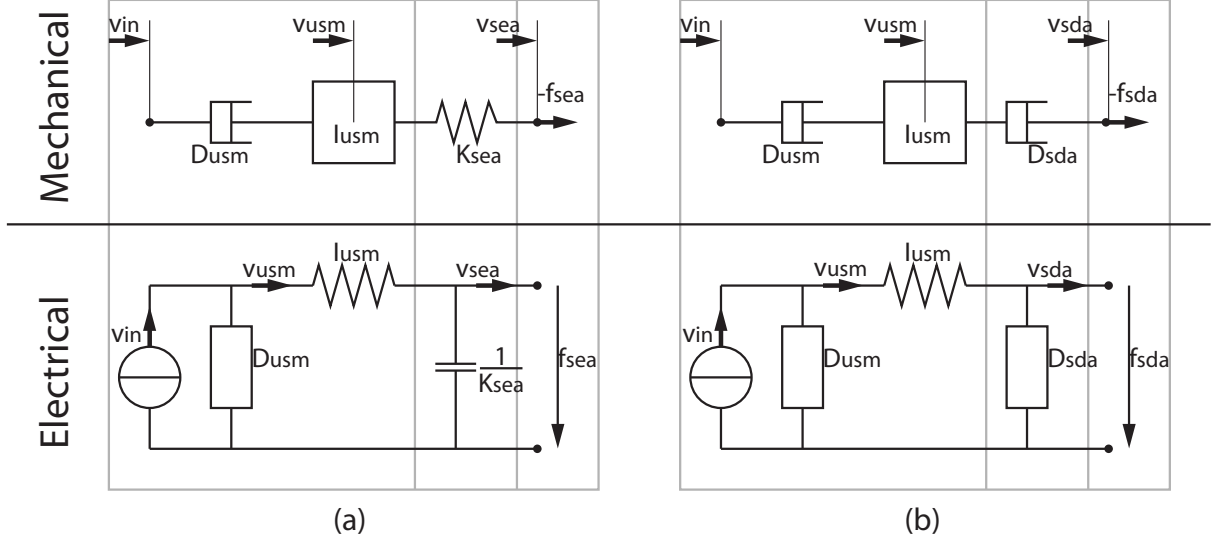


Figure 4.1: Mechanical models and electric equivalents of series dynamics applied to the USM. In the Series Elastic Actuator (a), a spring K_{sea} is connected to the USM output. In the Series Damper Actuator (b), a viscous damper D_{sda} is connected to the USM output.

The equation of motion the SDA is obtained from the one of the USM model 3.11 on which a viscous damper with a damping coefficient D_{sda} is added to the output:

$$\begin{cases} I_{usm}\ddot{x}_{usm} &= -D_{usm}(\dot{x}_{usm} - v_{in}) - D_{sda}(\dot{x}_{usm} - \dot{x}_{sda}) \\ 0 &= -D_{sda}(\dot{x}_{sda} - \dot{x}_{usm}) - f_{sda} \end{cases} \quad (4.14)$$

Steady States and D_{sda}

The steady state characteristic of the SEA is the solution of the Eq. 4.14 with constant velocities:

$$f_{sda} = -\frac{D_{sda}D_{usm}}{D_{sda} + D_{usm}}(\dot{x}_{usm} - v_{in}) \quad (4.15)$$

In the no-load conditions $f_{sda} = 0$, the velocity range of the SDA is the same than the one of the USM:

$$\begin{cases} v_{sda_{min}} = v_{usm_{min}} \\ v_{sda_{max}} = v_{usm_{max}} \end{cases} \quad (4.16)$$

The slope of the force-velocity curves of the SDA is modified by the added damper and is equal to the two dampers D_{usm} and D_{sda} connected in series. The added damper D_{sda} will decrease the forward gain of the SDA. This gain can be chosen in order to improve the force dynamic range of the SDA with the locked output. The USM gain is too high and the USM maximum force does not depend on the maximum input velocity, but on the maximum friction force on the rotor.

If the gain is decreased enough so that the input velocity range determines the zero-velocity force range, the force dynamic range will be improved. The force-velocity curve must reach $f_{usm_{max}}$ only at zero-velocity (point **a** in Fig. 4.2). This gives the following conditions on D_{sda} :

$$\frac{D_{sda}D_{usm}}{D_{sda} + D_{usm}} = \frac{f_{usm_{max}}}{v_{usm_{max}}} \Rightarrow D_{sda} = \frac{f_{usm_{max}}D_{usm}}{D_{usm}v_{usm_{max}} - f_{usm_{max}}} \quad (4.17)$$

With this damping coefficient D_{sda} , the force dynamic range with the SDA fixed output will be equal to the no-load velocity dynamic range. At no velocity $\dot{x}_{sda} = 0$, the SDA minimum output force $f_{sda_{min}}$ is minimized relatively to the SDA maximum output force $f_{sda_{max}}$:

$$\begin{cases} f_{sda_{min}} = \frac{v_{usm_{min}}}{v_{usm_{max}}} f_{usm_{max}} \\ f_{sda_{max}} = f_{usm_{max}} \end{cases} \quad (4.18)$$

Applied to the USR30 parameters, the gain and the output impedance are decreased by a factor of 3 and the force dynamic range increased from 7 to 20 (i.e. multiplied by a factor 3).

In the steady state force-velocity curves Fig. 4.2, the area covered by the SDA at no-speed is wider than that of the USM. This improvement is obtained in detriment of the high force and high speed operating area.

The added viscous damper D_{sda} reduces the effect of the non-linearities ΔD_{usm} of the USM rotor friction D_{usm} on the output force f_{sda} . If ΔD_{usm} is small, the force error Δf_{sda} due to ΔD_{usm} can be estimated with a first order development:

$$f_{sda} = \frac{D_{sda}(D_{usm} + \Delta D_{usm})(v_{in} - \dot{x}_{sda})}{(D_{usm} + \Delta D_{usm}) + D_{sda}} \quad (4.19)$$

$$\Delta f_{sda} \simeq \frac{\partial f_{sda}}{\partial \Delta D_{usm}} \Big|_{\Delta D_{usm}=0} \Delta D_{usm} = \frac{D_{sda}^2}{(D_{usm} + D_{sda})^2} (v_{in} - \dot{x}_{sda}) \Delta D_{usm} \quad (4.20)$$

The linearities of the SDA is improved as the error on the output force of the SDA Δf_{sda} decreases with the square of the static gain reduction of the output force.

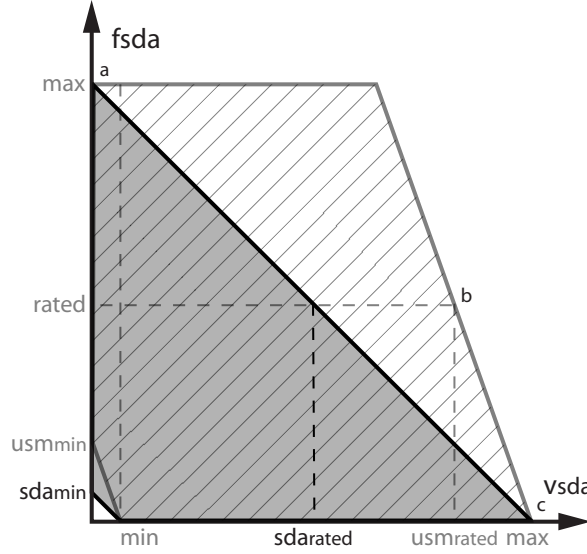


Figure 4.2: USR30 steady state force-velocity curve given by the specifications. The hatched area is the operating area of the USM and SEA. The plain area is the operating area of the SDA powered by the USM. The SDA dynamic force range is increased thanks to a smaller gain.

Forward Transfer Function

The dynamic of the SDA can be evaluated by its transfer function H_{sda} with its fixed output $\dot{x}_{sda} = 0$. The transfer function of the SDA in the Laplace domain H_{sda} is obtained from Eq. 4.14.

$$H_{sda}(s) = \frac{F_{sda}}{V_{in}} = \frac{D_{sda}D_{usm}}{I_{usm}s + D_{sda} + D_{usm}} \quad (4.21)$$

The transfer function of the SDA has a unique pole making it easier to control than the SEA. The added viscous damper D_{sda} has a limited influence on the bandwidth ω_{sda} , it even increases the bandwidth ω_{sda} :

$$\omega_{sda} = \frac{D_{sda} + D_{usm}}{I_{usm}} \quad (4.22)$$

The influence of D_{sda} is shown on the Bode's plot of H_{sda} (Fig. 4.3(a)). The response of the SDA has a smaller gain than the USM, but its value is constant on the considered frequency range. Hence, the SDA doesn't limit the USM bandwidth.

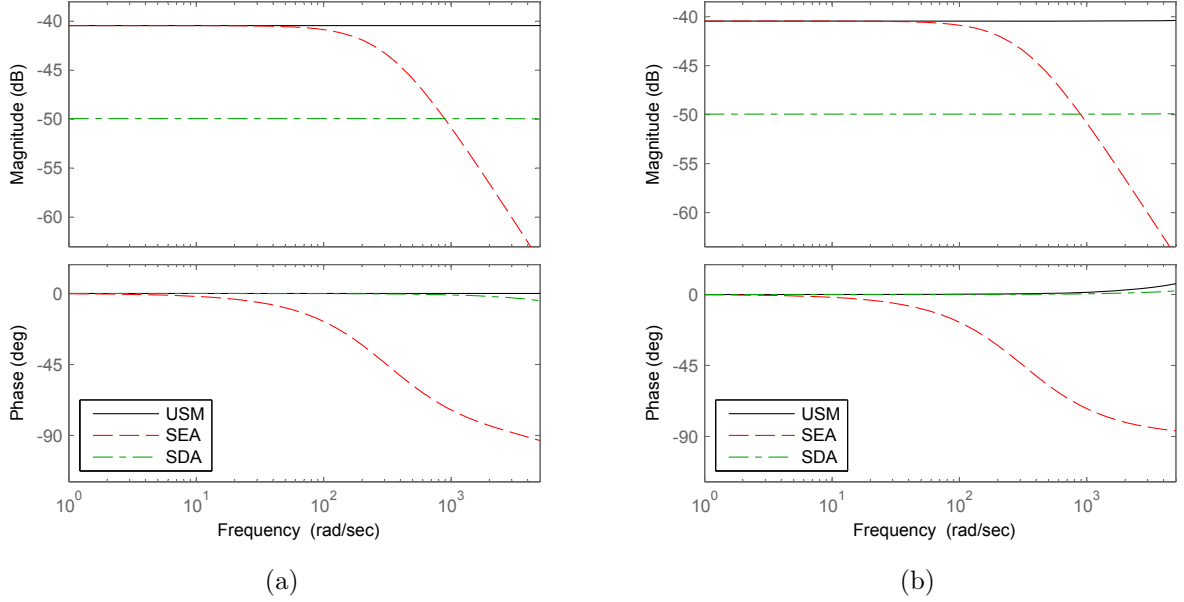


Figure 4.3: (a) Bode plots of the transfer functions of the USM, the SEA and the SDA with their locked output. (b) Bode plots of the output impedance of the USM, the SEA and the SDA.

Output Impedance

The SDA free output impedance Z_{sda} is obtained by canceling the input v_{in} in the Eq. 4.14

$$Z_{sda}(s) = -\frac{F_{sda}}{V_{sda}} = D_{sda} \frac{I_{usm}s + D_{usm}}{I_{usm}s + D_{sda} + D_{usm}} \quad (4.23)$$

Compared to the USM, the output impedance Z_{sda} is constant and smaller on the whole frequency range (Fig. 4.3(b)).

Safety

During normal operation, the maximum output force of the SDA is limited by the added viscous damper.

When the USM is turned off, the behavior of the SDA is obtained from Eq. 3.14 and 4.14:

$$f_{sda} = D_{sda} \dot{x}_{sda} \quad (4.24)$$

The output force only depends of the viscous friction of D_{sda} , the remaining forces are dissipated. Then the SDA has a *safe power off state*.

4.1.3 Conclusion

The SEA and the SDA do not modify the no-load velocity range of the USM, but they modify the force range with the loaded output. The values of the USM, the SEA and SDA with the locked output are reported in Table 4.1 on page 66.

Between the two type of series dynamics actuators, the SEA is the most simple since the added spring is a common mechanical component. The spring improves the output force by transforming the force control into a position control task for the USM, and then the position resolution of the USM determines the force resolution of the SEA. In the electrical analogy, the SEA is a velocity source with a low pass filter, if the bandwidth required for the output force is small few hertz or tens of hertz, the SEA can be a good solution to achieve a smooth output force.

From a safety point of view, the compliance of the spring allows to move the output, even if the motor is turned off, but output force may remain due to the holding force, and the SEA is not able to limit the output force of the USM.

The SDA is the second type of series dynamics actuator, it uses a viscous damper, a more complex mechanical component than the spring. The added damper decreases the nonlinearities and the minimum output force of the USM. In the electrical analogy, the SDA consists in adding a shunt on the output of the velocity source, the output impedance cannot be decreased separately from the system gain.

The added damper improves the safety of the USM by dissipating the remaining force and by allowing the output motion when the USM is turned off. The maximum output force of the system can be limited with the added damper.

The SEA has a larger force dynamic range and is mechanically simpler than the SDA. On the other hand, the SDA is safer as its maximum output force can be limited and when the motor is turned off, no force remains on the output.

With the SEA and SDA, the components added in series influence the output impedance and the forward transfer function in the same way. They impose a tradeoff with the choice of their values. Because the series components are linear with respect to velocity, they can reduce but can not suppress the nonlinearities of the USM such as the minimum velocity $v_{usm_{min}}$.

4.2 Hybrid Actuators

Extending the electrical analogy, the USM is considered as a velocity source. To obtain a force source, a force regulator must be added. Because there is no suitable MR-compatible force-controlled active actuator, the added actuator is semi-active; it will be named differently depending on its configuration:

Brake when the input of the semi-active actuator is fixed, only its output moves.

Clutch when the semi-active actuator is mounted in series with another actuator. The input of the semi-active actuator is connected on the output of the other actuator, both its input and output move.

By adding the force-controlled clutch in series on the output of the USM, a novel actuator is obtained: the **Hybrid USM Clutch Actuator** (HUCA). The combination of these complementary actuators is unique. In our knowledge, the closest concept is a USM with a built-in static clutch [Aovagi 04]. Its static clutch can only connect or disconnect the output of the USM, in the electrical analogy it corresponds to a switch. This clutch doesn't improve the force control of the USM, but only allows free motions of the output. The HUCA extends the concept and the functionalities of the actuator presented in [Aovagi 04]. In this section, the properties of the HUCA will be investigated.

4.2.1 Force-Controlled Clutch

In order to determine the behavior of the HUCA, the clutch must first be modeled. The clutch can be considered as a force limiter where the force threshold, the limiting friction f_{lim} , is controlled. The clutch transmitted force f_{tr} cannot exceed f_{lim} . Because the clutch uses the friction occurring between its input x_{cl1} and its output x_{cl2} to transmit force, f_{tr} is determined by the relative velocity or the slipping $\Delta\dot{x}_{cl}$ of the clutch input and output:

$$\Delta\dot{x}_{cl} = \dot{x}_{cl2} - \dot{x}_{cl1} \quad (4.25)$$

Cases must be distinguished depending the value of f_{tr} with respect to f_{lim} . The clutch has then two operating modes:

Locked clutch while the norm of the transmitted force f_{tr} is smaller than the limiting friction f_{lim} , there is no slipping between the input and the output. In this mode, the slipping is null $\Delta\dot{x}_{cl} = 0$, the static friction (or stiction) occurs :

$$\Delta\dot{x}_{cl} = 0 \quad \text{if } |f_{tr}| < f_{lim} \quad (4.26)$$

The slipping value $\Delta\dot{x}_{cl} = 0$ is imposed, but not the transmitted force f_{tr} . Because in this mode, the input velocity \dot{x}_{cl1} is equal to the output velocity \dot{x}_{cl2} , the clutch can be considered as a rigid link.

Slipping clutch When the absolute value of transmitted force f_{tr} is equal to the limiting friction f_{lim} , the friction between the two parts can no longer increase and the two parts slip on each other to keep the force balance, this is the kinetic friction. In this mode the norm of the transmitted force f_{tr} is imposed by the limiting friction f_{lim} and only the direction of the slipping $\Delta\dot{x}_{cl}$ is determined. Then the transmitted force f_{tr} can

be expressed in function of the slipping $\Delta\dot{x}_{cl}$ and the limiting friction f_{lim} , this is the Coulomb friction:

$$f_{tr} = -sgn(\Delta\dot{x}_{cl})f_{lim} \quad \text{for } \Delta\dot{x}_{cl} \neq 0 \quad (4.27)$$

The Coulomb friction is not defined for $\Delta\dot{x}_{cl} = 0$, because in this condition the *locked clutch* mode must be considered.

In the *slipping clutch* mode, the transmitted force f_{tr} is controlled by f_{lim} and doesn't depend on the slipping value $\Delta\dot{x}_{cl}$. The clutch can be considered as a force source.

The desired clutch response has been reported in Fig. 4.4, the horizontal part of the curve is the *slipping clutch* mode while the vertical part is the *locked clutch* mode. The absolute value of the transmitted force f_{tr} is, in any cases limited by f_{lim} independently from its operating mode. The clutch is a controlled force limiter.

The electrical equivalent of the clutch can easily be built for the positive \dot{x}_{cl1} case, this is a variable force source f_{lim} in the *slipping clutch* mode. Because the clutch can only dissipate energy, a diode is added in series to the force source to prevent the slipping to flow in the opposite direction of the imposed voltage f_{lim} . The behavior of the diode is modeled as follows:

A short circuit when the velocity is in the diode direction, the force between its two ends f_d (defined positive in the diode direction) is zero.

An open circuit when the velocity or the voltage is opposed to the diode direction, the diode is non conducting. The force f_d is negative and equal to the applied voltage.

When the clutch is locked, the diode is in open circuit. Because the clutch can operate for negative v_{in} , a variable force source $-f_{lim}$ with a diode in the opposite direction is added in parallel to the first branch. The electrical equivalent of the ideal clutch is represented in Fig. 4.4.

The previous clutch model is ideal and to evaluate its performances some features must be included. The clutch is a complex mechanical component, its inertia cannot be neglected unlike for springs or dampers, thus an input I_{cl1} and output I_{cl2} inertias must be added to the ideal model. Another important limitation of the clutch is its limiting friction range in addition of a maximum $f_{lim_{max}}$, the minimum limiting friction $f_{lim_{min}}$, often called drag torque in real system, can be non-null. Then additional equations are required to describe the clutch behaviors:

$$\begin{cases} I_{cl1}\ddot{x}_{cl1} = f_{cl1} - f_{tr} \\ I_{cl2}\ddot{x}_{cl2} = f_{tr} - f_{cl2} \\ f_{lim_{min}} \leq f_{lim} \leq f_{lim_{max}} \end{cases} \quad (4.28)$$

Where f_{cl1} is the force applied to the input of the clutch and f_{cl2} is the force on the output of the clutch. With these equations, the clutch inertias can be added to the electrical model of the ideal clutch to obtain the real clutch model (Fig. 4.5). The model of this force-controlled clutch can now be used to define the behavior of the HUCA.

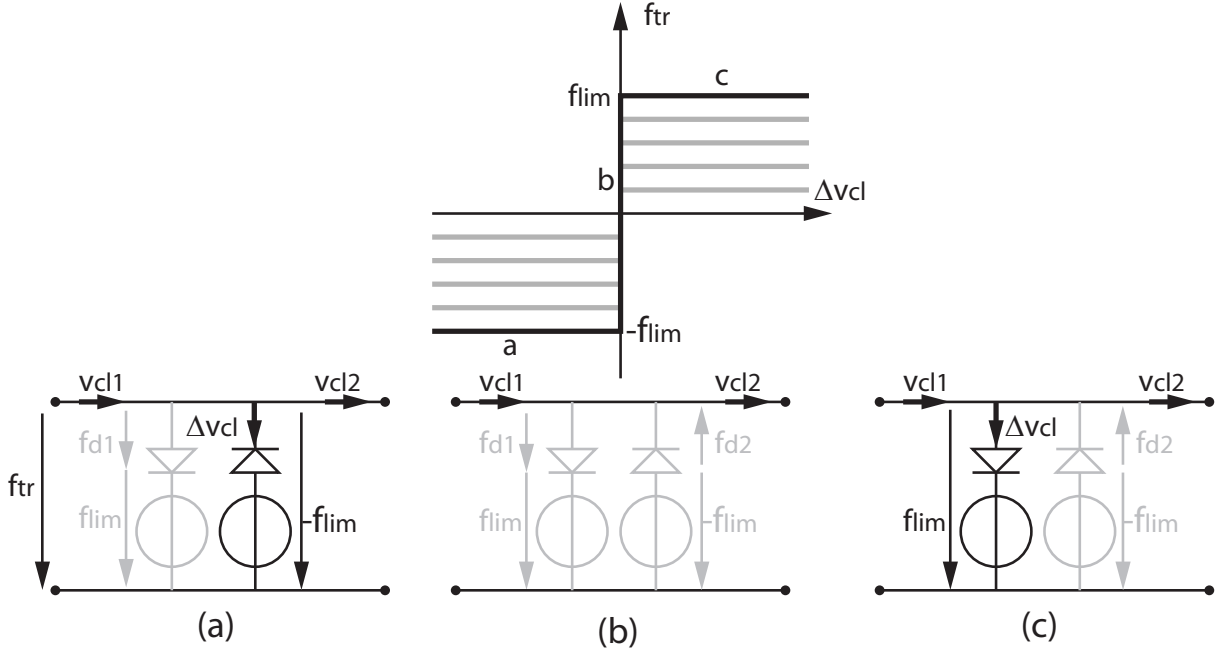


Figure 4.4: On top, the ideal clutch force-velocity curves. On bottom, the **ideal clutch circuit**, the conducting branch are drawn in black and the non-conducting in grey. (a) the $-f_{lim}$ force source branch is conducting for negative Δv_{cl} , the transmitted force is then $-f_{lim}$. (b) f_{tr} is included between $-f_{lim}$ and f_{lim} , no branch is conducting, the entire input force and velocity are transmitted by the clutch. (c) the f_{lim} force source branch is conducting for positive Δv_{cl} , the transmitted force is then f_{lim} . In the next circuits only one force source branch will be drawn to simplify the schematics.

4.2.2 Operating Modes

In the HUCA, the clutch is added in series to the USM. The output of the clutch becomes the output of the HUCA, and the output of the USM is connected to the input of the clutch, giving these relations:

$$\begin{cases} x_{cl1} = x_{usm} \\ x_{cl2} = x_{huca} \\ f_{cl1} = f_{usm} \\ f_{cl2} = f_{huca} \end{cases} \quad (4.29)$$

The electrical equivalent of the HUCA is obtained by adding the electrical equivalent of the clutch to the USM one (Fig. 4.6). The main difference with the series dynamics actuator is the additional control possibility given by the variable force source f_{lim} . The USM and the clutch have respectively two operating modes, in total this makes four operating modes for the HUCA. The modes with the *USM OFF* are not interesting, because the USM output is

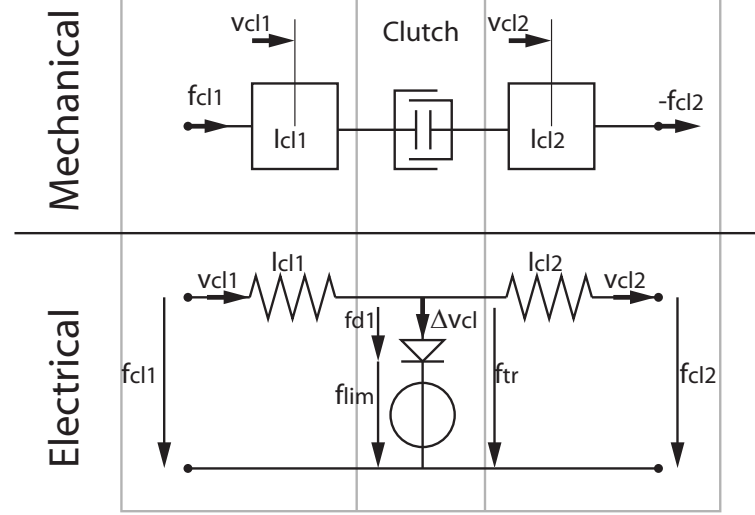


Figure 4.5: Mechanical model and electrical equivalent of the **real clutch**.

fixed $\dot{x}_{usm} = 0$, the HUCA behaves like a brake. The modes with the *USM ON* are more interesting, because both active and resistive forces can be displayed. In these modes, the equations describing the HUCA are:

$$\begin{cases} (I_{usm} + I_{cl1})\ddot{x}_{usm} = -D_{usm}(\dot{x}_{usm} - v_{in}) - f_{tr} \\ I_{cl2}\ddot{x}_{huca} = f_{tr} - f_{huca} \end{cases} \quad (4.30)$$

The value of the transmitted torque f_{tr} depends on the different clutch modes (Fig. 4.7), the HUCA behaviors must be considered separately.

Locked clutch To enable this mode, f_{lim} must be set higher than the absolute value of the transmitted force f_{tr} . The clutch behaves like a rigid link (Fig. 4.7a):

$$(I_{usm} + I_{cl1} + I_{cl2})\ddot{x}_{huca} = -D_{usm}(\dot{x}_{huca} - v_{in}) - f_{huca} \quad \text{if } |f_{tr}| < f_{lim} \quad (4.31)$$

The behavior of the HUCA is similar to the USM with an increased output inertia and v_{in} is used to control the output. In this mode, the HUCA output is velocity-controlled.

Slipping clutch To enable this mode, f_{lim} must be set low enough to allow the slipping of the clutch. Then the HUCA is described by:

$$I_{cl2}\ddot{x}_{huca} = -sgn(\Delta\dot{x}_{cl})f_{lim} - f_{huca} \quad \text{if } \Delta\dot{x}_{cl} \neq 0 \quad (4.32)$$

The HUCA output is force-controlled by the limiting friction f_{lim} . The USM must be controlled to ensure the direction of the HUCA output force:

$$\begin{cases} \dot{x}_{usm} > \dot{x}_{huca} & \text{if } f_{huca} > 0 \\ \dot{x}_{usm} < \dot{x}_{huca} & \text{if } f_{huca} < 0 \end{cases} \quad (4.33)$$

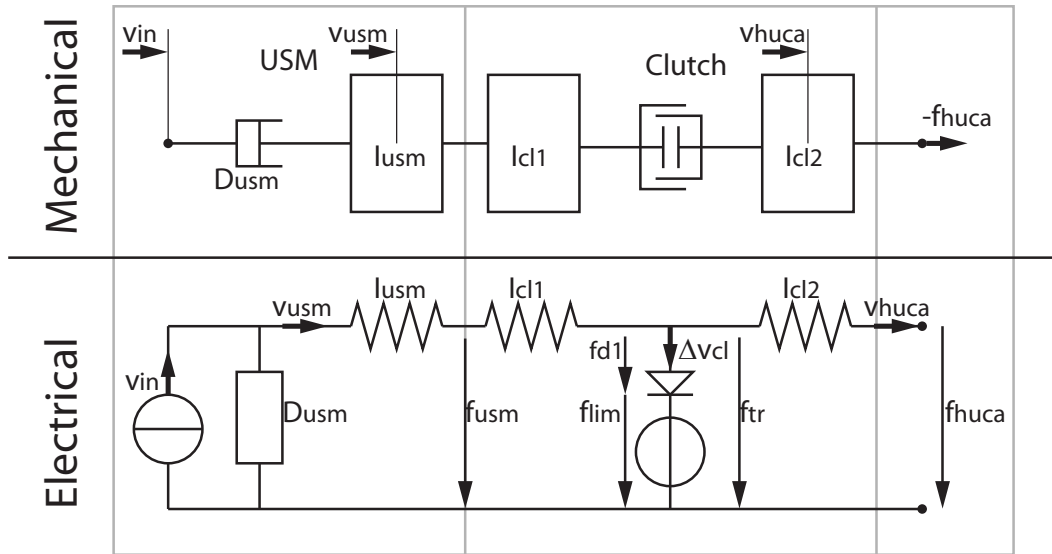


Figure 4.6: Mechanical and electrical model of the HUCA.

In the electrical equivalent, this corresponds to providing enough velocity to keep the proper diode conducting and then the proper force source connected. In this mode the USM is used as a velocity source and the clutch modulates the output force by dissipating the excess of velocity.

An interesting property of the HUCA is that it can behave like one of its constituting actuators:

- a USM when the clutch is locked
- a brake when the USM is turned off.

This is because both of them are connected serially and can lock their respective output.

4.2.3 Properties

The *locked clutch* and the *slipping clutch* modes can both output active forces. Because they differ in their operation principle, their specificities will be investigated. The literal expressions of the HUCA will be evaluated with the parameters of the USR30 and the particle brake¹

¹The particle brake operation is based on the friction of ferromagnetic particles on a rotor. This friction is proportional to the magnetic field and can be then controlled by the current. The braking torque norm does not depend on the velocity.

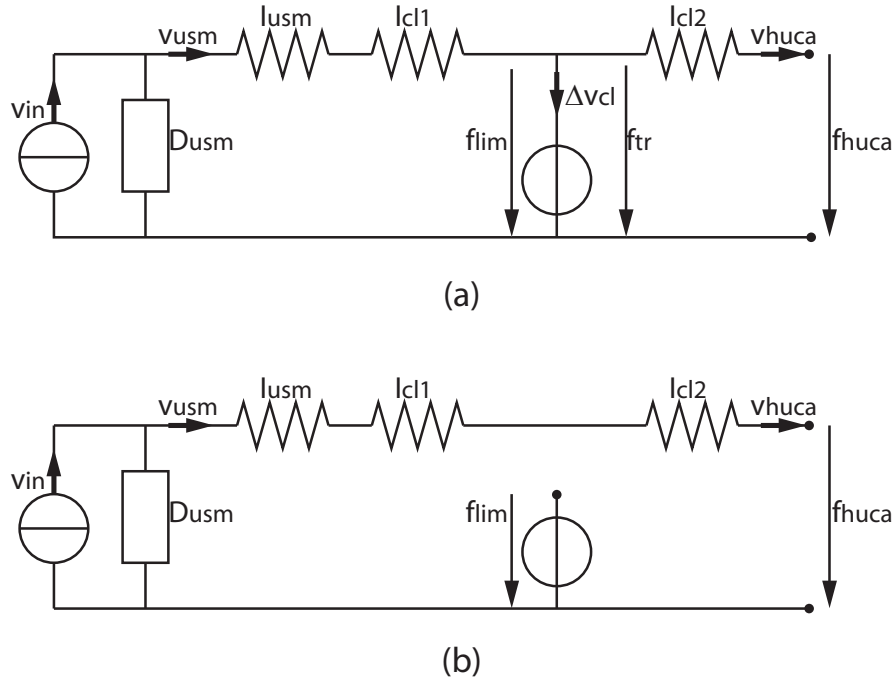


Figure 4.7: (a) The slipping clutch behaves like a force source. (b) The locked clutch is similar to a rigid connection.

S90MPA-B15D19S (from Sterling Instrument, USA) to allow the comparison of these different operating modes and the comparison of the HUCA with the other series dynamics actuators such as the SEA and SDA.

Steady States

The steady state characteristic of the HUCA is obtained by canceling the acceleration terms of the HUCA motion equation Eq. 4.33.

Locked clutch the HUCA has the same characteristics than the USM due to the cancelation of the inertias.

$$f_{huca} = -D_{usm}(\dot{x}_{huca} - v_{in}) \quad (4.34)$$

Slipping clutch the characteristic is:

$$f_{huca} = -sgn(\Delta \dot{x}_{cl}) f_{lim} \quad (4.35)$$

The force-velocity curve of HUCA is a horizontal line. Velocity variation on the output of the HUCA or the USM does not influence the output force of the HUCA in steady state. An example of the entire system curve can be obtained by combining the curves of the HUCA in both modes with fixed input values v_{in} and f_{lim} (Fig. 4.8).

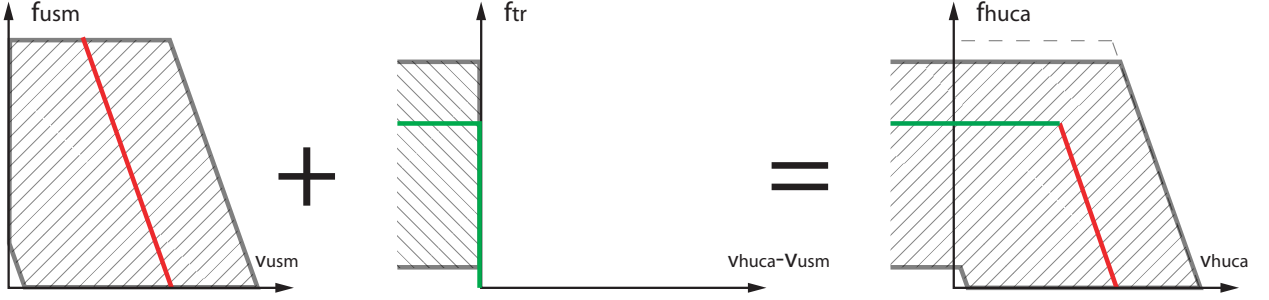


Figure 4.8: The force-velocity curve of the HUCA is the result of the addition of the clutch velocity with the USM velocity

As the HUCA is made of two actuators assembled in series, its output force range is determined by the smallest values between the USM and the clutch force range:

$$\begin{cases} f_{huca_{min}} = \min(f_{lim_{min}}, f_{usm_{min}}) \\ f_{huca_{max}} = \min(f_{lim_{max}}, f_{usm_{max}}) \end{cases} \quad (4.36)$$

The adjunction of the clutch allows to reach any velocity below the force-velocity curves of the HUCA and in the limiting friction f_{lim} range. In order to improve the HUCA force range, the clutch must be chosen with a smaller minimum limiting friction than the USM minimum force and a maximum limiting friction close to the USM maximum force. The theoretical force range obtained with the HUCA constituted by the USR30 and the S90MPAB15D19S have been reported in Table 4.1. In steady-states, the HUCA force-velocity curves (Fig. 4.9) cover more surface than the SEA and SDA (Fig. 4.2).

Forward Transfer Functions

The dynamic behavior of the HUCA with its fixed end is evaluated with its transfer functions.

Locked clutch the input is v_{in} and because the clutch is considered as an open circuit (Fig. 4.7b), the transfer function of the HUCA H_{huca_l} is the same as the USM.

$$H_{huca_l}(s) = \frac{F_{huca}}{V_{in}} = D_{usm} \quad (4.37)$$

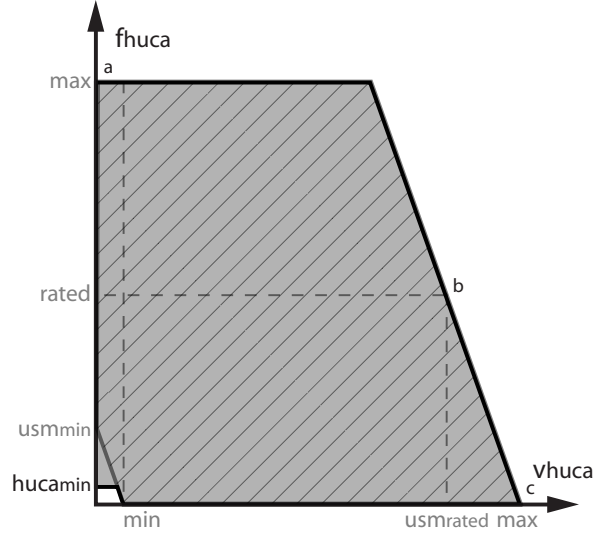


Figure 4.9: The force-velocity curves of the HUCA (plain) extends the USM operation area (hatched) to low velocity and low force operations.

Slipping clutch the input is the limiting friction f_{lim} and v_{in} is kept constant. In order to avoid being affected by the nonlinearities, small variations of f_{lim} around a constant value will be considered (small signals). In this mode, the transfer function of the HUCA H_{huca_s} is then:

$$H_{huca_s}(s) = \frac{F_{huca}}{F_{lim}} = 1 \quad (4.38)$$

With the locked output, the transfer functions in both modes do not vary with the frequency, because v_{in} and f_{lim} are considered as ideal power sources.

Output Impedance

The HUCA has two different output impedances corresponding to its operating modes.

Locked clutch the output impedance of the HUCA is the same as the USM with the added clutch inertia.

$$Z_{huca_l}(s) = -\frac{F_{huca}}{sX_{huca}} = (I_{usm} + I_{cl1} + I_{cl2})s + D_{usm} \quad (4.39)$$

Slipping clutch the clutch is considered as a force source, thus it is replaced by a short circuit to cancel it. The output impedance is determined only by the rotor inertia of the clutch I_{cl2}

$$Z_{huca_s}(s) = -\frac{F_{huca}}{sX_{huca}} = I_{cl2}s \quad (4.40)$$

The output impedance of the HUCA varies with its operating modes. It is significantly decreased with the *slipping clutch* and increased due to the clutch inertia with the *locked clutch*. The output inertia of the HUCA constituted of the USR30 and the S90MPAB15D19S has been summarized in Table 4.1. The output inertia of the *locked clutch* mode is determined mostly by I_{cl1} , because the output inertias of the USM I_{usm} and clutch I_{cl2} are 100 times smaller than I_{cl1} .

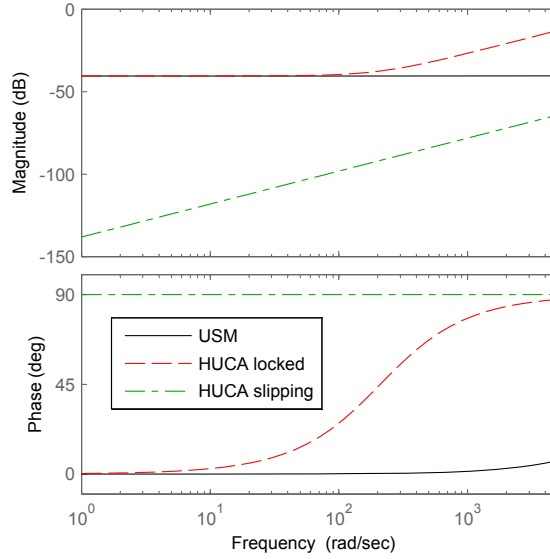


Figure 4.10: Bode plots of the output impedance of the USM and the HUCA.

Conclusion

Locked clutch in this mode the HUCA is similar to the USM with an increased output inertia. The HUCA behaves rather like a velocity source, then this mode is adapted for position or admittance control.

Slipping clutch the properties of the HUCA are mainly determined by the clutch, because the transmitted force does not depend on velocity variation, the output force control is improved. The clutch can improve the HUCA force range by decreasing the minimum output force $f_{huca_{min}}$. The HUCA output impedance is also decreased as it is equal to the clutch output impedance I_{cl2} . Even if the clutch input inertia I_{cl1} does not appear directly in the expression of the HUCA output force f_{huca} , I_{cl1} decreases the dynamic of the clutch velocity \dot{x}_{usm} . It increases the required time to invert the direction of f_{huca} . In this mode the HUCA is assimilated to a force source and can be controlled in force or in impedance.

With the added clutch, the USM has improved its ability to output force with a low output impedance without any tradeoff. By changing from one operating mode to the other, the HUCA can behave like a velocity source or a force source. This can be used to output a wide range of impedances.

4.2.4 Safety

In order to have a safe system, the clutch must cope with the USM lacks of safety such as the holding force or the force peaks due to impacts.

In normal operating modes (*slipping clutch* and *locked clutch*), the clutch improves the safety as the maximum transmitted force cannot exceed the limiting friction f_{lim} . It behaves like a controllable force limiter on the HUCA output. In addition to the limited force, the HUCA velocity is intrinsically limited by the maximum velocity of the USM. This is an important safety feature for a force-controlled system. This avoids uncontrolled acceleration of the HUCA output, when the user releases it, this is not the case with DC motors.

When the entire system is turned off, the holding force locks the output of the USM $\dot{x}_{usm} = 0$, then the HUCA behaves like a brake.

$$I_{cl2}\ddot{x}_{huca} = f_{tr} - f_{huca} \quad (4.41)$$

A force f_{huca} at least equal to f_{lim} must be applied to move the HUCA output. To have a safe power-off state with the HUCA, the remaining limiting friction $f_{lim_{off}}$ must be low enough so that the output can be moved.

With the HUCA, the different output values that represent a hazard like excessive forces, velocities or blocking hazards are addressed by their physical limitations and by a *safe power off state*.

4.3 Conclusion

Different mechanical components can be added in series in order to improve the force control and the safety. The adaptation of series dynamics to the USM has been investigated. One can

Table 4.1: Theoretical specifications of the USR30, series dynamics actuators and HUCA (with the brake S90MPAB15D19S used as a clutch).

	USM	SEA	SDA	HUCA	
Series component		2.97	$4.8 \cdot 10^{-3}$	Clutch	
		$[Nm/rad]$	$[Nms/rad]$	Locked	Slipping
Minimum force $[Nm]$	0.015	0.009	0.005	0.015	0.0045
Maximum force $[Nm]$	0.100	0.100	0.100	0.100	0.100
Force dynamic range	6.7	11	20	6.7	22
Output inertia $[kgm^2]$	$2.3 \cdot 10^{-7}$	$2.3 \cdot 10^{-7}$	$2.3 \cdot 10^{-7}$	$4.5 \cdot 10^{-5}$	$1.2 \cdot 10^{-7}$
Output friction $[Nms/rad]$	$9.5 \cdot 10^{-3}$	$9.5 \cdot 10^{-3}$	$3.2 \cdot 10^{-3}$	$9.5 \cdot 10^{-3}$	0

add passive components in series, such as springs (SEA) or viscous dampers (SDA), between the load and the USM output. Criteria for the choice of the the spring or viscous damper values have been defined in function of the USM specificities. With the series dynamics, the force range has been improved.

However this approach is limited, because it tries to transform a velocity source into a force source with the adjunction of linear components. The output impedance is modified in the same way than the forward transfer function, resulting in a loss of bandwidth for the SEA and a loss of gain for the SDA. Due to their linearities, the added components cannot completely suppress the USM non-linearities.

For these reasons, the HUCA concept has been introduced. The HUCA consists in adding a force-controlled clutch, a semi-active actuator, to the USM. This clutch is a non-linear component able to impose the output force on the output of the HUCA. Thanks to the complementarity between the clutch and the USM, the HUCA has two distinct properties depending the clutch operations modes:

Locked clutch The HUCA has high output impedance and behaves like a velocity source.

Slipping clutch In this mode, the HUCA has theoretically no viscous friction, a lower output inertia and a higher force range than any series dynamic actuators. It is considered as a force source.

The HUCA with its two different types of actuators is more complex than the series dynamics actuators. In the *slipping clutch* mode, it shows better properties to control its output force than the series dynamics actuators.

Compared to the USM, the safety with the series dynamics actuators is improved, the added spring or viscous damper allow moving the output when the motor is turned off. With the SEA, forces can remain when the USM is switched off, and the maximum output force of the SEA cannot be limited. In contrast, no force remains on the SDA when the USM

is switched off and the maximum force can be limited with the SDA. For these reasons the SDA is safer than the SEA. With the HUCA, the maximum output velocity and force are respectively limited by the USM and the clutch. In addition the HUCA has a safe power off state, and thus it is safer than the USM with series dynamics.

Therefore the proposed HUCA is safer and has better performances than the SEA and SDA series dynamics actuators.

Chapter 5

Implementation

The HUCA concept can be realized in different mechanical configurations. Factors like inertias of the clutch, the integration of the sensors and the wiring must be taken into account in the retained solution.

5.1 Clutch Configurations

Usually the input inertia I_{cl1} includes the housing of the actuator and different other components constitute most of the clutch inertia. In order to obtain good result in the real systems, the influence of the heavy parts on the output dynamic must be limited.

5.1.1 Direct Clutch

This configuration is the most simple, it corresponds to the schematic diagram presented in the subsection 4.2.2. The semi-active actuator is mounted directly on the output of the USM. This configuration has been applied to a geared DC motor and a magnetorheological clutch in a SDA[Chew 04], the clutch is controlled in order to behave like a viscous damper.

Influence of the Clutch Input Inertia

The principle of the HUCA in *slipping clutch* mode is a velocity source which output force is modulated by a clutch. Because the output force direction depends on the USM velocity (Eq. 4.32), then the velocity source V_{cl1} (Fig. 5.2) constituted of the USM and the input inertia clutch I_{cl1} must have a good dynamic. Its transfer function is obtained by setting $f_{lim} = 0$:

$$V_{cl1} = \frac{D_{usm}}{(I_{usm} + I_{cl1})s + D_{usm}} V_{in} \quad (5.1)$$

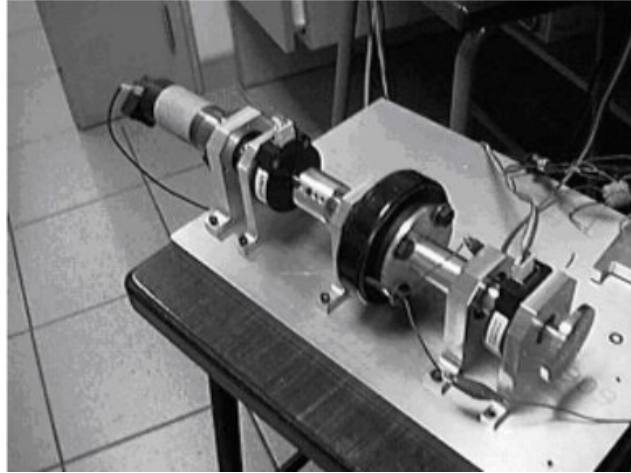


Figure 5.1: A motor-clutch actuator reprinted from [Chew 04]. The clutch is controlled to behave like a viscous damper.

The velocity source with the free end of the USM alone is:

$$V_{usm} = \frac{D_{usm}}{I_{usm}s + D_{usm}} V_{in} \quad (5.2)$$

The input clutch inertia can be two orders larger than the USM rotor inertia I_{usm} , the bandwidth of the velocity source can then be decreased from the same orders.

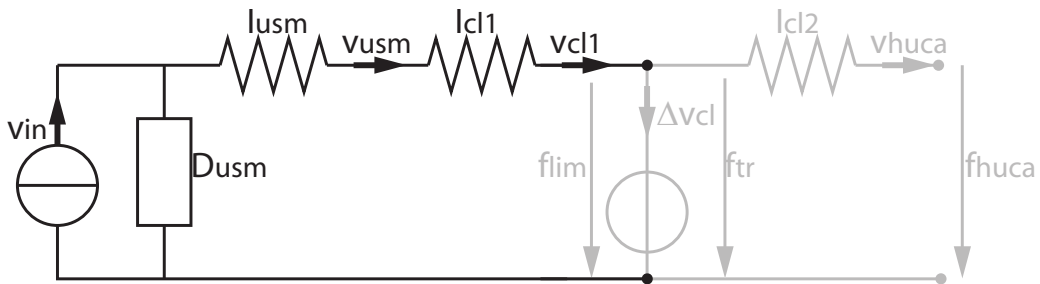


Figure 5.2: In the *slipping clutch* mode, the velocity source powering the clutch must have a good dynamic in order to change the output force direction quickly. The input clutch inertia I_{cl1} affects the dynamic of the USM velocity v_{usm} .

Conclusion

The direct clutch is the simplest solution and is constituted of only the necessary mechanism, limiting the overall inertia and plays. This system is only suitable for clutch with low inertias, if else additional mechanical elements must be used to cope the limitations due to I_{cl1} .

5.1.2 Redundant Clutches

The ElectroRheological Actuator (ERA) [Sakaguchi 98] is a motor-clutch system with two clutches which inputs rotate in opposite direction and outputs are connected together. To cope the clutch input inertias I_{cl1} limitation, the powered clutch is changed in function of the force direction instead to vary the USM velocity v_{usm} .

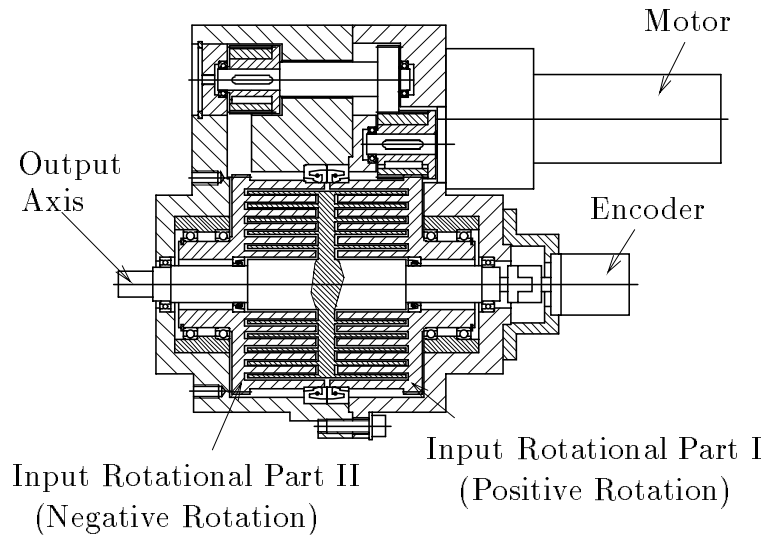


Figure 5.3: Section schematic of the ERA, reprinted from [Sakaguchi 98]. The unique motor powers two electrorheological clutches in opposite direction.

In the ERA, the two clutches are powered by the same motor. To reverse the rotation direction of one clutch, an inverter is introduced between it and the motor. The inverter is a particular transmission. To get the property of the ERA, the transmission must be modeled.

Transmission

The mechanical and electrical model of the transmission presented in this section come from [Lauria 08]. The transmission is a two ports mechanical element, that can change the force

and velocity of its output compared to the one applied on its input. Its equations are:

$$\begin{cases} f_2 = n f_1 \\ \dot{x}_2 = \frac{1}{n} \dot{x}_1. \end{cases} \quad (5.3)$$

where n is the gear ratio. \dot{x}_1 and f_1 are respectively the input velocity and force of the transmission and \dot{x}_2 and f_2 are respectively the output velocity and force of the transmission.

In addition to modifying the input force or velocity, the transmission modifies the impedances seen through the other end. If Z_1 is an impedance connected to the transmission input, Z'_1 is its reflected impedance seen from the output.

$$\begin{cases} Z_1 = \frac{F_1}{V_1} \\ Z'_1 = \frac{n F_1}{\frac{1}{n} V_1} = n^2 Z_1. \end{cases} \quad (5.4)$$

The transmission can be modeled by a *lever* (Fig. 5.4) where the positions of the pins determine the value and the sign of the gear ratio.

Its electrical equivalent is the *transformer*. In the force/voltage analogy, the electrical transformation ratio is the inverse of the gear ratio, then to avoid any confusion the gear ratio will be kept in the electrical equivalent.

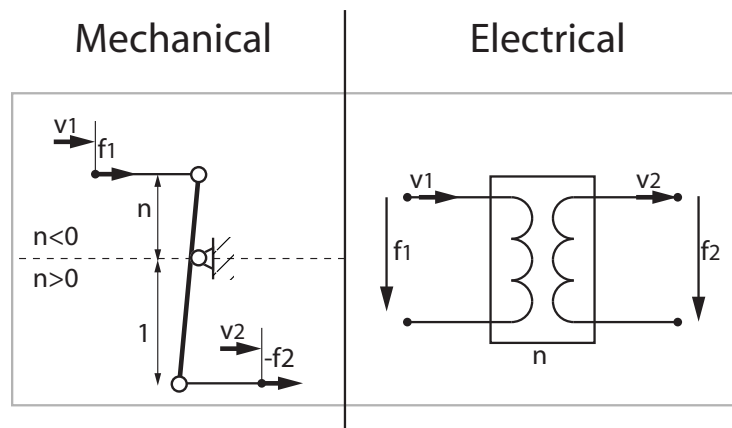


Figure 5.4: The transmission is symbolized by a lever drawn in thick line. The lever can translate horizontally and rotates in the plane, while the thin lines can only translate horizontally. The vertical motion of the lever is neglected. Its electrical equivalent is a transformer. [Lauria 08]

Remark from the author In small motions, the tangential forces and velocities of a lever must obey to the same or equivalent laws than for the torques and velocities than a coaxial shafts rotative transmission :

- The **kinematic constraints**, the gear ratio determines the transmitted velocity.
- The **power conservation** in conjunction with the imposed transmitted velocity, it gives the transmitted force or torque.
- The **forces or torque balance** gives the reaction force or torque respectively on the fixed end of the lever or the housing of the transmission.

For this reason, the lever in small motion and tangential forces is the translational equivalent of the rotative transmission.

Model

The mechanical model of the ERA (Fig. 5.5) is obtained by connecting on the *USM* output directly the *clutch1* and through the *inverter* the *clutch2*. The inverter is modeled by a transmission with a gear ratio of -1 . The outputs of both clutches are connected together on the ERA output.

The ERA electrical equivalent (Fig. 5.5) is more difficult to build. The *clutch1* and the input of the transformer must be connected serially to the output of the USM, because in the mechanical model the input of the *inverter* and the *clutch1* have the same velocity. Instead of adding negative signs on the output force and velocity of the inverter, its output branches have been inverted, then the *clutch2* is mirrored compared to the *clutch1*. The connection of the clutches outputs can be solved by observing the velocities. The output of the ERA as the same velocity than the output inertias I_{cl2} of both clutches, then the external output branches of the clutches are the output branches of the ERA. The internal clutches output branches are connected together to close the velocity loop.

Properties

With the electrical circuit, the ERA output force f_{era} can be easily obtained with the Kirchhoff's voltage law:

$$\left\{ \begin{array}{l} f_{era} = f_{tr1} - f_{tr2} - 2I_{cl2}\ddot{x}_{era}. \end{array} \right. \quad (5.5)$$

In normal operation, both clutches are used in *slipping clutch* mode. The USM velocity is constant and is set higher than the absolute value of $|v_{era}|$, then the transmitted forces f_{tr1} and f_{tr2} can be expressed with the limiting frictions f_{lim1} and f_{lim2} :

$$\left\{ \begin{array}{l} \Delta\dot{x}_{cl1} > 0 \\ \Delta\dot{x}_{cl2} > 0 \end{array} \right. \Rightarrow f_{era} = f_{lim1} - f_{lim2} - 2I_{cl2}\ddot{x}_{era} \quad (5.6)$$

where $\Delta\dot{x}_{cl1}$ and $\Delta\dot{x}_{cl2}$ are the slipping of each clutch. The ERA output force f_{era} is controlled by the two f_{lim} and doesn't depend on v_{usm} .

The advantage of this arrangement is that the clutches friction forces are self-compensated. In absolute value, smaller forces than the clutch drag force f_{limmin} can be reached with the ERA.

The ERA output impedance Z_{era} can be obtained from the Laplace's transform of Eq. 5.6 and by setting the $f_{lim1} = f_{lim2} = 0$:

$$Z_{era} = -\frac{F_{era}}{sX_{era}} = \frac{1}{2I_{cl2}s} \quad (5.7)$$

The inertia on the USM output is increased by two times I_{cl1} . This doesn't decrease the ERA dynamics, because v_{usm} is kept constant. Even the additional inertias reduces the variation of v_{usm} by increasing the output impedance of the velocity source.

Conclusion

This arrangement is very smart, for the limited output inertia and for the self compensation of the clutch drag forces. However it requires two clutches and its use with one *locked clutch* is not well adapted due to the important inertia on the USM output. The ERA is only well adapted to output force.

5.1.3 Differential-Brake

To avoid the input inertia of the semi-active actuator I_{cl1} of the direct clutch configuration, a differential-brake system can be used. The differential allows putting in series a fixed input component. By combining the differential to a brake, a clutch can be obtained [Chapuis 06].

Differential

The differential is a three ends transmission with 2 DOF. The differential can be obtained from any two coaxial shafts transmission by using its housing as third port [Müller 82]. This can also be applied to a lever, by using its fixed end as third port giving the simplified mechanical model of the differential [Lauria 08].

The previous output x_2 becomes the second input, and the housing x_3 becomes the output. The mechanical model of the differential (Fig. 5.7) corresponds to the transmission model (Fig. 5.4) with its third end moving instead to be grounded.

The Willis equation can be used with any three-port mechanisms with coaxial input/output shafts to determine the velocities relation between its inputs and output. As seen in the subsection 5.1.2, the lever is the translational equivalent of a rotative two coaxial shafts transmission. The process to transform a lever and a rotative transmission into a differential is the same: changing the velocity of the fixed end. Then the Willis equation can be extended to the lever.

$$\dot{x}_1 - n\dot{x}_2 = (1 - n)\dot{x}_3 \quad (5.8)$$

where n is the speed ratio between \dot{x}_1 and \dot{x}_2 , when \dot{x}_3 is locked, this corresponds to the transmission presented previously. Any value of n can be used except $n = 0$ or $n = 1$. For these values, a velocity term of the equation is no more defined. This corresponds in the mechanical model 5.7 to the case when \dot{x}_1 is applied at the same point than \dot{x}_2 or \dot{x}_3 . The relation between the forces can be deduced from the sum of torques on the lever used in the mechanical model:

$$f_3 = (1 - n)f_1 = \left(1 - \frac{1}{n}\right)f_2 \quad (5.9)$$

where f_3 is the output force of the differential, and f_1 and f_2 are the forces of the inputs.

Because the point of interest is the differential output, its velocity \dot{x}_3 and force f_3 will be expressed with the two input variables and their gear ratios:

$$\begin{cases} f_3 = n_1 f_1 = n_2 f_2 \\ \frac{\dot{x}_1}{n_1} + \frac{\dot{x}_2}{n_2} = \dot{x}_3. \end{cases} \quad (5.10)$$

where n_1 and n_2 are the gear ratio between the considered input and the differential output \dot{x}_3 . n_1 and n_2 can be identified with the term factors of Eq. 5.9. Because they depend both on n , n_1 and n_2 are not independent. The general differential electrical equivalent is modeled by two transformers with their outputs connected in parallels 5.7 [Lauria 08].

In the case where $n_1 = n_2 = 1$, the equations of the differential become:

$$\begin{cases} f_1 = f_2 = f_3 \\ \dot{x}_1 + \dot{x}_2 = \dot{x}_3. \end{cases} \quad (5.11)$$

Because these equations are the Kirchoff's law of a three-branch node, the electrical equivalent of a differential with unitary gear ratios is a three-branch node. To use this electrical equivalent in a general case instead of the model of Fig.5.7, the reflected components values (as seen in subsection 5.1.2) seen trough the same differential port must be used in the electrical equivalent circuit. This method simplifies the equivalent circuit by suppressing the transformers and allows to express the reflected values seen trough the port of interest.

Model

To allow comparison between the different clutch configurations, the gear ratios of the differential must be unitary; however the differential-brake system can be designed with other gear-ratios.

Because n_1 is equal to n_2 in absolute value only when $n = -1$, their value must be equal to 2. A transmission with a gear ratio $n_3 = 0.5$ is added on the output differential to have a

unitary gear ratio on the entire system (Fig. 5.8). Then the equation of the differential with the transmission becomes the same than Eq.5.11:

$$\begin{cases} f_3 = n_1 n_3 f_1 = n_2 n_3 f_2 = f_1 = f_2 \\ \dot{x}_3 = \frac{\dot{x}_1}{n_1 n_3} + \frac{\dot{x}_2}{n_2 n_3} = \dot{x}_1 + \dot{x}_2. \end{cases} \quad (5.12)$$

The transmission added on the output of the differential is not compulsory; it is required for some specific gear ratios and to improve the accessibility of the differential middle shaft.

The mechanical model of the HUCA with a differential-brake can be built by assembling its different components (Fig. 5.8). The brake is modeled by a clutch with its input grounded. Its output is connected to the input of the differential constituting the differential-brake. The USM is connected to the other input of the differential. The output of the differential is connected to a transmission as discussed below.

Its electrical equivalent (Fig. 5.8) can be build around the differential. Because this differential as unitary gear ratio, a three-branch node can be used. On the input of this node, the brake output is connected. The electrical equivalent of the brake is the clutch equivalent with its input disconnected. On the other node branch, the output of the USM is connected and the remaining branch constitutes the output of the HUCA.

Properties

The HUCA with the differential-brake differs from the HUCA with a direct clutch by the positions of the clutch inertias. With the differential-brake, due to the fixed brake housing, I_{cl1} doesn't influence the output force of the HUCA.

In the *locked clutch* mode, the ideal clutch appears like an open circuit in the electrical equivalent 5.8. Then the velocity and the force of the HUCA is equal to the one of the USM:

$$\text{If } \dot{x}_{cl2} = 0 \text{ then } \begin{cases} \dot{x}_{huca} = \dot{x}_{usm} \\ f_{huca} = f_{usm} \end{cases} \quad (5.13)$$

Then the HUCA behaves like the USM alone. This is an improvement compared to the HUCA with the direct clutch where the inertia of the whole clutch is added on the USM output in the *locked clutche* mode.

In the *slipping clutch* mode, the clutch is assimilated to a velocity source f_{lim} in the electrical equivalent of the HUCA. The brake velocity \dot{x}_{cl2} can be expressed by \dot{x}_{huca} and \dot{x}_{usm} :

$$\dot{x}_{cl2} = \dot{x}_{huca} - \dot{x}_{usm} \quad (5.14)$$

Then f_{huca} can be calculated from the electrical equivalent of the HUCA:

$$f_{huca} = I_{cl2}(\ddot{x}_{usm} - \ddot{x}_{huca}) + \text{sgn}(\dot{x}_{usm} - \dot{x}_{huca})f_{lim} \quad (5.15)$$

The output force of the HUCA is mainly controlled by f_{lim} , however the dynamic force due to I_{cl2} is not only determined by the acceleration of the output \ddot{x}_{huca} , but also by the acceleration of the USM \ddot{x}_{usm} . Then the velocity of the USM can be used to compensate the dynamic force of I_{cl2} .

The output impedance of the HUCA with the differential-brake is the output impedance of the USM Z_{usm} in parallel with the brake rotor inertia I_{cl2} .

$$Z_{huca_s} = Z_{usm} // I_{cl2}s = \frac{I_{cl2}(I_{usm}s^2 + D_{usm})}{(I_{usm} + I_{cl2})s + D_{usm}} \quad (5.16)$$

The output impedance with the differential-brake becomes smaller than I_{cl2} .

The drawback of the HUCA with the direct clutch is the loss of bandwidth of the increased inertia on the output of the velocity source powering the clutch; this problem is solved with the differential-brake. The equation determining \dot{x}_{cl2} , the velocity powering the brake can be determined with the force loop on the electrical equivalent of the HUCA 5.8:

$$D_{usm}(\dot{x}_{usm} - v_{in}) + I_{usm}\ddot{x}_{usm} - I_{cl2}(\ddot{x}_{cl2}) - \text{sgn}(\dot{x}_{cl2})f_{lim} = 0 \quad (5.17)$$

Its Laplace's transfer function is computed from 5.17 with the HUCA locked output $\dot{x}_{huca} = 0$ and the clutch turned off $f_{lim} = 0$:

$$V_{cl2} = -\frac{D_{usm}}{(I_{usm} + I_{cl2})s + D_{usm}} \quad (5.18)$$

With the differential-brake, the velocity source powering the ideal brake is the USM with the added inertia I_{cl2} instead of I_{cl1} in the case of the direct clutch. Because I_{cl2} is small, the bandwidth of this velocity source is not decreased significantly compared to the USM alone.

The other advantages of the differential-brake:

- Different gear ratios can be set between its two inputs. This is an additional parameter to adjust the force or velocity ranges between the USM and the brake. In the differential elastic actuator DEA, a harmonic drive has been used as a differential with a high reduction ratio to increase the motor torque and to connect serially a spring [Lauria 07].
- The two actuators have their housing fixed making the electrical connection easier, otherwise slip rings will be required to ensure the electrical connection of rotating parts.

Like most of mechanical components, the differential may introduce friction forces in the system. Because the USM is a velocity source, it will be less sensitive to friction compared to the brake. Then the output of the HUCA and the brake must be connected to the end of the differential between which the less friction occurs. The differential may have some backlash.

Conclusion

Although the increased complexity, the differential-brake offers several advantages over a direct clutch, the most important is to fix the housings of the two actuators. This limits the moving inertias and simplifies their wiring. Because both actuators are in parallel in the electrical equivalent, the output impedance of the HUCA is decreased. The dynamic force due to I_{cl2} is null with the *locked clutch* and can be compensated with the *slipping clutch*.

The different gear ratios between its three ends can be used to adapt the ranges of the different components. Because the differential-brake allows the use of brakes with a large housing inertia and keep good performance in both *locked clutch* and *slipping clutch* modes, it will be preferred to the other clutch solutions.

5.2 Sensors

To allow the interaction with the user and to control the internal states of the actuator, sensors must be added to the HUCA. The required sensors depend on the desired type of control (subsection 2.1.1). Initially, the HUCA is designed to be controlled in impedance and requires only a motion sensor on its output. The USM and the clutch are controlled in open-loop. To improve the velocity output by the USM, a second motion sensor can be added to the USM to perform a closed-loop motion control.

The two HUCA operating modes allow to use it in admittance control. This control schemes requires the measure of the HUCA output force, then a force sensor must be integrated in the HUCA.

Because the HUCA will be used in a MR environment, the considered sensors must be MR-compatible. Compared to the actuation, that brings a large amount of power inside the MR room, the sensors require much less electrical power for their operation. The sensing poses less compatibility problems than the actuation [Gassert 08b].

In this section, the MR-compatibility and the integration of the required sensors will be discussed.

5.2.1 Motion

In the MRI environment, the measure of the position is the usual way to determine the motion. This can be done by the mean of potentiometers [Gassert 06b, Mraz 03] or by optical encoders [Elhawary ss, Khanicheh 05]. These two types of sensors are constituted by a powered base and a moving part: in the encoder, an optical scale or a code wheel and in the potentiometer, a sweep.

The optical encoder is preferred to the potentiometer as it is a contact less measurement that doesn't introduce friction in the system. Its incremental principle provides a good resolution and a good immunity to the EM noise of the scanner.

To integrate the position sensors in the HUCA, their moving parts must be added on the measured parts of the HUCA and the base is fixed to the mechanical ground. The installation of position sensor requires only some free space. The influence of the position sensors on the dynamics of the HUCA is limited due to the small inertia of their moving part.

In addition to the one added on the HUCA output, the other sensor is added on the USM output in order to perform a position or velocity feedback control on it. With these two position sensors, the motion of the clutch can be calculated, and then the state of the HUCA is entirely known.

5.2.2 Force

In the force sensor, the measured force is applied to an elastic body that converts the load stress into a strain. This strain is transformed into an electric signal by a transducing element. This principle is used by the MR-compatible force sensors that differ by their transducing elements.

The MR-compatible force sensors have been used first to measure the user force in fMRI studies on the human force control [Kawato 03, Kuhtz-Buschbeck 01]. Most of them use commercial load cells made without ferromagnetic metal [Hidler 06, Krainak 07]. Their transducing elements are strain gauges that could emit or be affected by the EM noise.

To have a better EM immunity, sensors measuring optically the strain have been developed. Thanks to the optical fibers, the light sources and the photodiodes of these sensors are kept out of the MR-room. The strain measurement can be done by measuring the variation of light received by the fibers due to the motion of the emitting fiber [Tada 02, Riener 05] or due to the motion of the mirror reflecting the measured light beam [Chapuis 04]. In [Sutherland 03], the photoelastic effect is used to measure the strain. Because the optical strain measurement is less sensitive than strain gauge, it requires a more compliant elastic body. Force sensors based on optical strain measurement will be preferred to the one based on electrical strain gauges for their EM immunity.

The measure of the force requires inserting the force sensor between the elements withstanding the measured force. Mechanically force sensing is a serial process, making its application more complex than the motion measurement (a parallel process). Ideally the force sensor must be inserted on the output point 1 on Fig. 5.9, the closest from the force application point. However this is not always possible to move the sensor base due to its wires or its optical fibers, then they can be added between the base of an actuator and the mechanical ground. With the direct clutch only the USM can be used (point 2 on Fig. 5.9), while for the differential-brake the brake housing can also be used (point 3 on Fig. 5.9). To see from the position 2 or 3, which is the best alternative, there are several factors to consider.

The force sensor by its elastic body is a stiff spring K_{sens} that has been represented by capacitor on the electrical equivalent on Fig. 5.9. When inserted between an actuator and the ground, it allows the motion of the actuator housing. The dynamics of the system will be modified.

To study it, the USM housing must be added in the USM model. The stator assimilated to a velocity source is now represented by the symbol of a piezo, its output is v_{in} added from the motion of its input. The input of the stator is connected to the USM housing inertia I_{usm0} . Without the force sensor, this housing is connected to the mechanical ground. In the electrical equivalent, the ideal velocity source was already represented, only the housing inertia I_{usm0} must be added to the velocity source output. The other end of I_{usm0} is an open circuit as the housing doesn't move.

Added inertia To limit the inertia on the output impedance, the force sensor must be added on the actuator with the smallest housing inertia, usually I_{usm0} is smaller than I_{cl2} . Thanks to the differential, the influence of the added housing inertia is limited. In the electrical equivalent, this inertia is always in parallel with another lower impedance.

If the gear-ratios of the differential are not the same, the smallest reflected inertia seen from the differential output must be chosen.

Interactions with power source The force sensor and the actuator housing inertia constitute an oscillator connected to a power source. Connected to the USM (point 2 on Fig. 5.9), the oscillations of this system can be damped thanks to the USM friction D_{usm} .

When the force sensor is connected to the brake (point 3 on Fig. 5.9), the oscillator is connected to a force source in the *slipping clutch* mode. Then the oscillations pass through this source and are not damped. Because the value of the measured force depends on the strain of the elastic body, oscillations may affect the force measurements.

Friction If in the differential brake, there is an important difference of friction between the differential inputs, the sensor must be placed on the input with the less friction to minimize its influence on the measurement. Normally this must be on the brake side.

The integration of the force sensor depends on different parameters, and then there isn't a straightforward solution. With the differential-brake system, the force sensor must be mounted on the USM side to have a good dynamics and on the brake side to limit the effect of the friction on the measurement.

5.3 Conclusion

From the HUCA concept different types of clutches can be used and sensors must be added in order to have a complete system. The clutch configuration depends on the inertia of the semi-active actuator. If the semi-active actuator has a low inertia, it can be mounted directly on the USM output; otherwise the differential-brake must be used to hide its housing inertia. The HUCA can be used with a unique position sensor at its output, but the integration of a second position sensor and force sensor can improve its performance and allow admittance

control. The position sensors must be added preferentially on the HUCA and USM output, because their positions are used in the control loops. If possible, the force sensor must be mounted on the HUCA output; otherwise it can be mounted between the mechanical ground and the housing of the HUCA actuators by considering the housing inertia and the friction of the system.

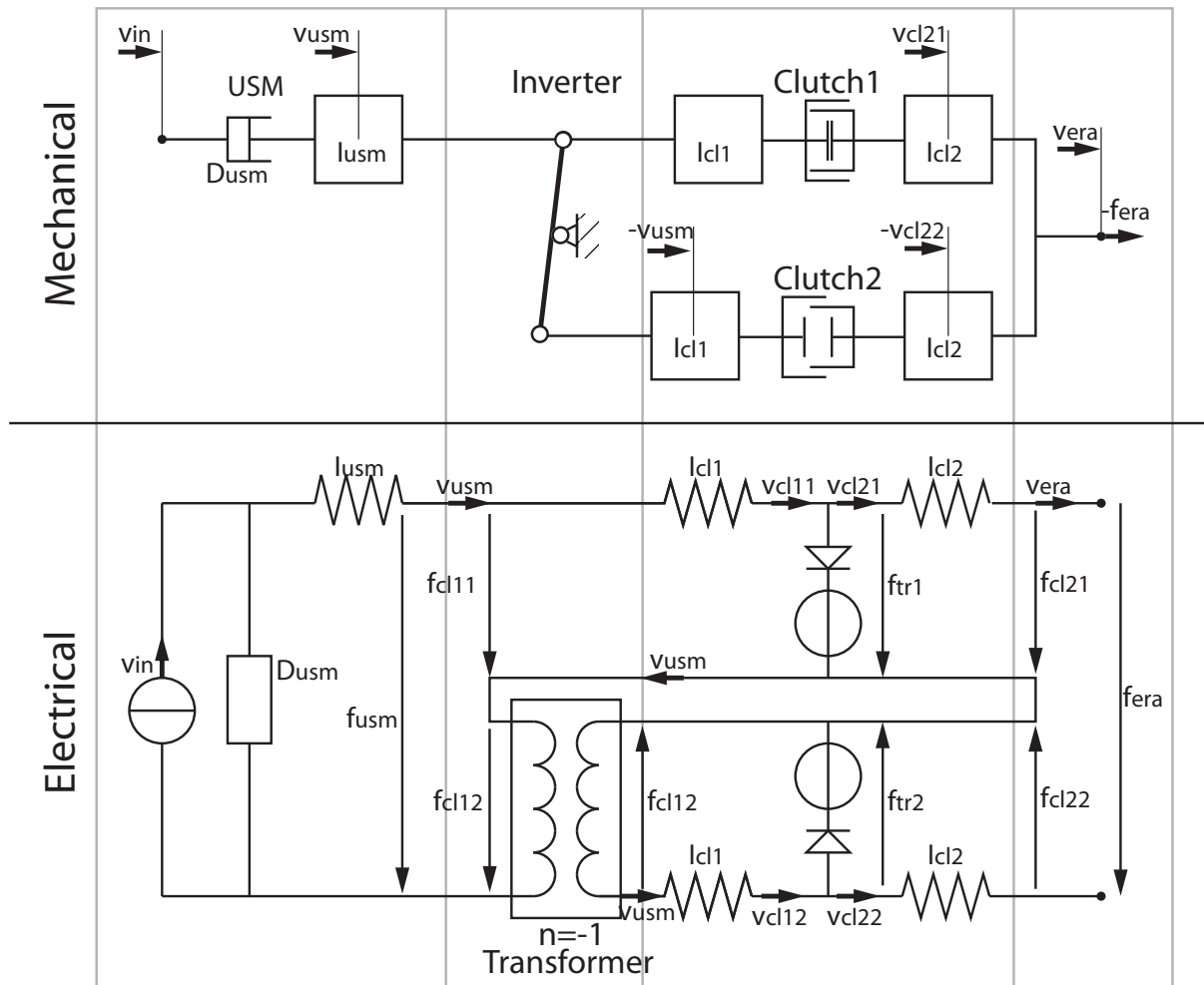


Figure 5.5: ERA mechanical and electrical models. The ERA is constituted of two clutches powered in opposite direction by a unique motor running at constant velocity.

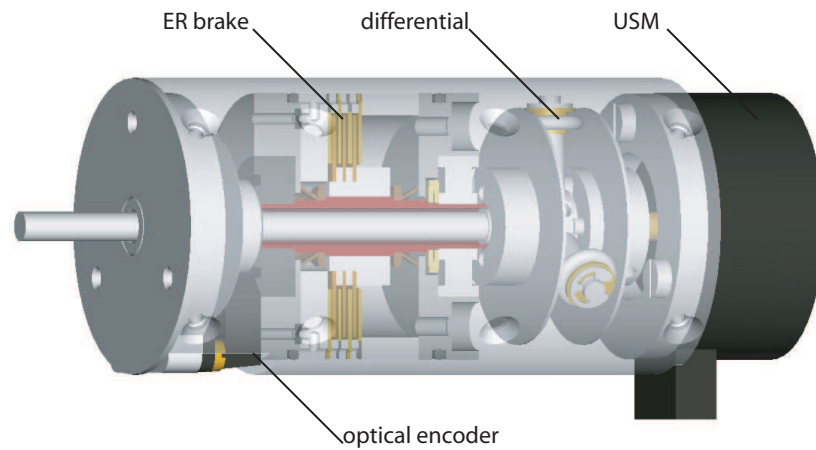


Figure 5.6: Schematic of the integrating the differential-brake system, instead of a clutch, reprinted from [Chapuis 06]

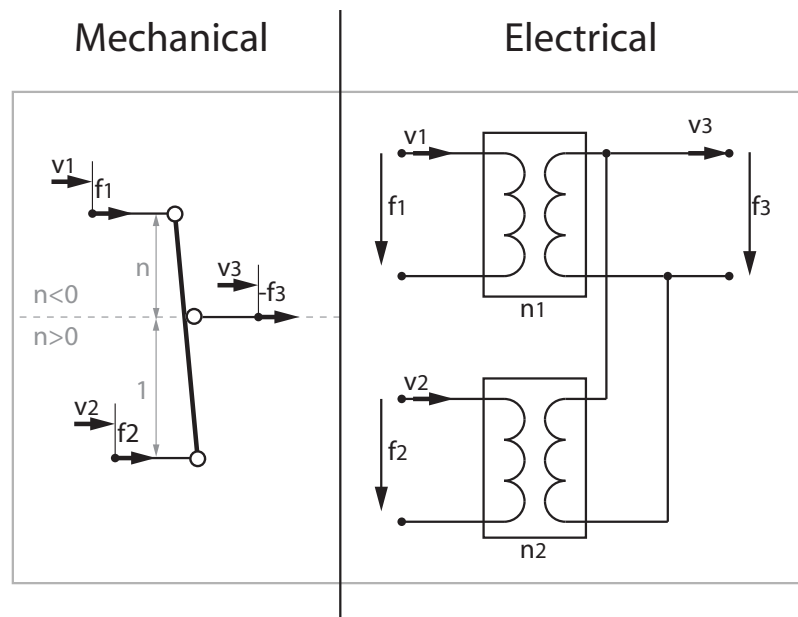


Figure 5.7: Mechanical and electrical models of the differential. The differential can have different gears ratios for each input.

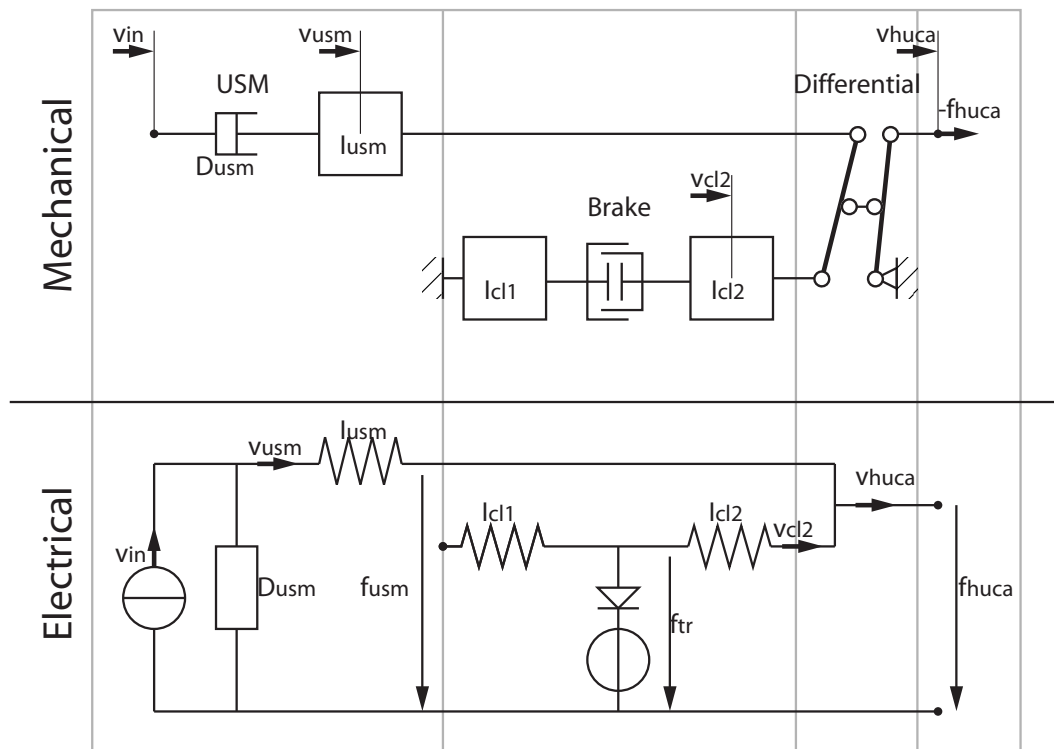


Figure 5.8: HUCA constituted of a differential-brake system.

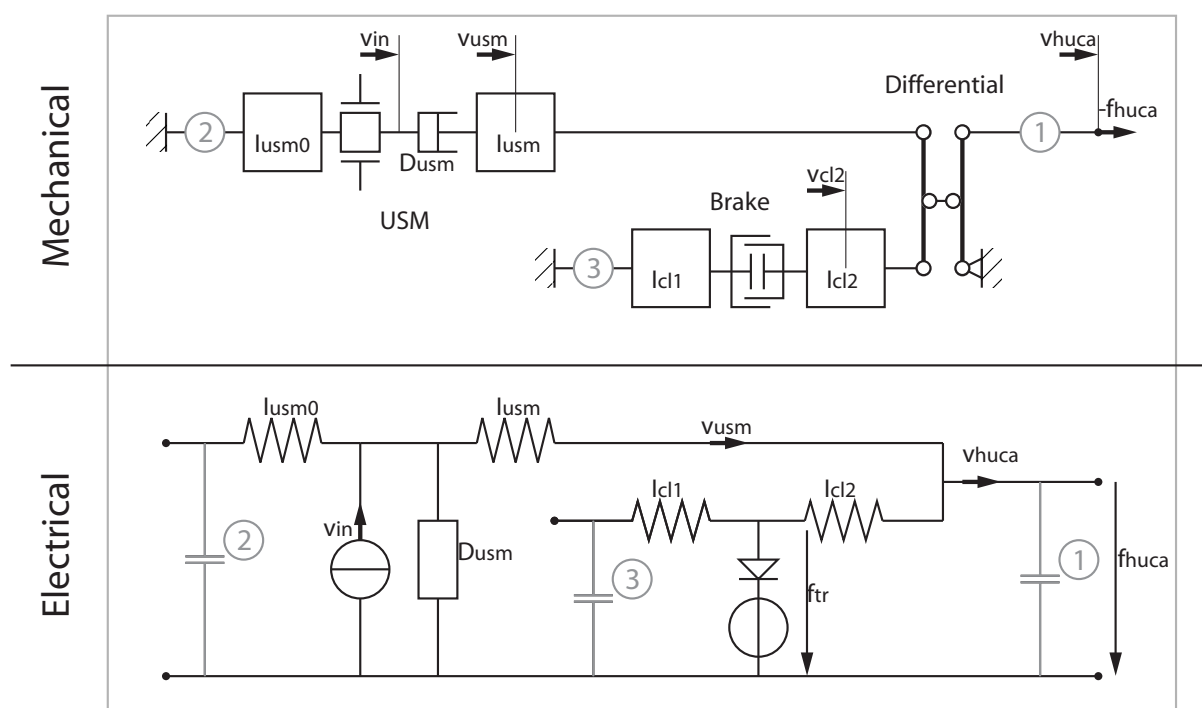


Figure 5.9: There is 3 preferential positions for a force sensor in the HUCA with a differential-brake: (1) at the output, (2) between the USM and the mechanical ground or (3) between the brake and the mechanical ground. The mechanical model has been completed with the symbol of a piezo representing the stator (the velocity source v_{in}) and a inertia I_{usm0} representing the housing.

Chapter 6

Prototypes

Two haptic knobs powered by HUCA's have been realized. The knob has been chosen for its mechanical simplicity and its large interest in haptics. The first prototype has been developed in order to verify the HUCA concept and the related solutions. In addition, it can be used as a test bench to investigate control strategies [Chapuis 07]. Non MR-compatible components have been used in order to shorten the development time. The second prototype has been designed to operate in the MR environment and its MR-compatibility must be tested [Chapuis 08]. The design and the components of these two prototypes are discussed in this chapter.

6.1 Non MR-Compatible Haptic Knob

The goal of this prototype is to verify the validity of the HUCA concept and also the differential-brake. Different haptic effects will be implemented on this knob to demonstrate the ability of the HUCA in impedance control.

6.1.1 Design

The heart of the HUCA is the USM; the other components have been chosen in order to fit it.

USM

The USM is a USR30-E3N (Shinsei Corporation Inc., Japan) with a rated torque of 50 *mNm*. It has been chosen, because its torque range is adapted to the interaction with the fingers and because it is non-magnetic (for the future MR-compatible prototype).

Brake

In this prototype a differential-brake system is used because no clutches are small enough for the USR30 and to validate the concept itself.

While it exists different types of force-controlled brakes, most of them use a magnetic principle.

Hysteresis brake The braking force is created by a variable magnetic field passing through a high hysteresis magnetic material. The braking force does not show any viscosity, and its drag torque is very small. However, its braking force in function of the current shows hysteresis, making difficult the control of dynamic force.

Powder/particles brake In the powder brake, the variable magnetic field passes through a magnetic powder in contact with the rotor. The friction of the powder will be proportional to the strength of the magnetic field. This brake has a higher drag torque than the hysteresis brake, but its braking torque, proportional to the current, is easier to control.

MagnetoRheological fluid brake The principle of this brake is similar to the powder brake, excepted that the particles are suspended in a fluid. The braking force is created by the shear stress in the fluid rather than the friction.

A powder brake has been chosen for its availability in small size and torque. The selected brake is S90MPA-B11D121S (Sterling Instrument, USA), which has a very low drag torque compared to its maximum limiting torque $f_{lim_{max}}$ of $34mNm$. The brake torque range is a little low compared to the USR30, but the small drag torque is privileged.

Differential

The differential has been designed in order to have the same gear ratios for each input. None of the USM and the powder brake has a hollow shaft restricting the access to the differential middle shaft. A transmission is required to reach the differential output.

A friction wheel differential is used for its low force ripples and its limited play, two qualities sought in haptics. It consists of a stack of three disks (Fig. 6.1). The two external disks are the inputs, and the middle disk is the output. To ensure that the angular velocity of the middle disk is the average of the external disks, planetary wheels are added. Each side of the planetary wheel rolls on the external disks and their shafts are mounted radially on the middle disk. To control the normal forces on the planetary wheels, i.e. the transmittable torque, a spring has been used to press the two external disks together. A timing belt is placed around the output disk to transmit the motion to the output knob.

In order to reduce the rolling resistance, the three planetary wheels rolling between the two external disks are mounted on ball bearings and different materials have been tested for the planetary wheels. O-rings made of natural rubber have been used first, their low

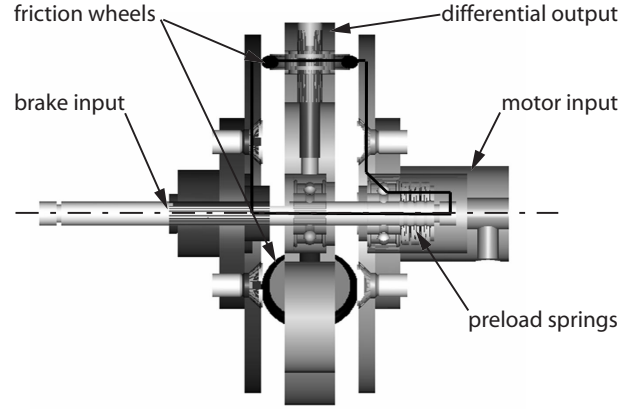


Figure 6.1: Cross section view of the friction wheel differential.

stiffness induce high rolling resistance and compliance in the actuator. Better results have been obtained with aluminum wheels rolling on an aluminum surface. The poor slippage property of aluminum $\mu = 1 \sim 1.4$ ensures a high transmittable torque and the high hardness prevents deformation while the wheels roll, which limits the rolling resistance and compliance in the transmission. However, this solution adapted to a haptic application suffers from wear and is not appropriate for an intensive use as required in industrial applications.

With the friction wheel differential, the gear ratio of the inputs to the output is 0.5. In order to have a transmission ratio of 1 for the entire system, the gear ratio of the timing belt transmission is chosen equal to 2 giving the following equations for the system:

$$\omega_{usm} + \omega_{brake} = \omega_{huca} \quad (6.1)$$

$$t_{huca} = t_{usm} = t_{brake} \quad (6.2)$$

Where ω_{usm} , ω_{brake} and ω_{huca} are the angular velocities of the USM, the brake and the knob, and t_{usm} , t_{brake} and t_{huca} are their respective torques.

Sensors

This haptic knob is designed to be used in impedance control, therefore the measurement of the output position is required. A code-wheel (HEDS5140-A11) mounted on the output shaft and an optical encoder (HEDS91040A, both from Agilent Technologies, Inc., USA) are used to determine the output angle. The resolution of this system is 500 *cpr* (count per round) without quadrature.

Control system

In order to control the haptic knob, a PC equipped with a DAQ card (NI-PCI6221, National Instrument Corp., USA) is used. This DAQ card is used to read the output position given by the encoder and to send commands to the USM and brake drivers. The USM driver is a D6030 (Shinsei Corporation Inc., Japan); a PWM circuit is used to amplify the voltage for the brake. The control and the different haptic effects were implemented with Labview8.0. The fastest control loop achieved with this system has a sampling period of 10 *ms*.

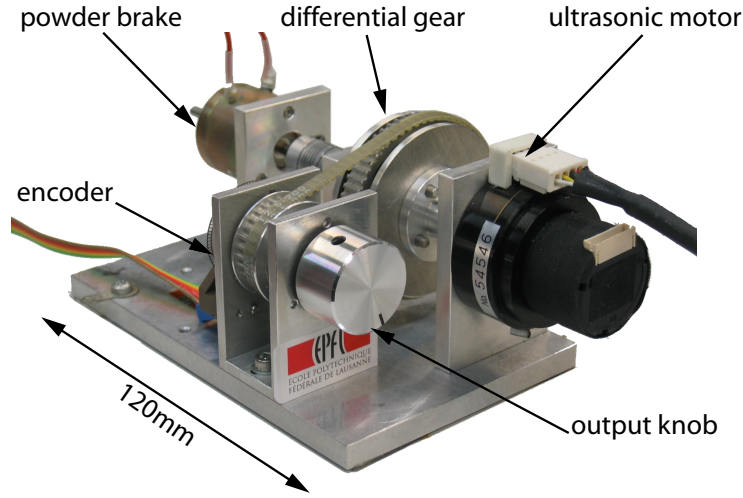


Figure 6.2: Photography of the haptic knob with a powder brake.

6.1.2 Preliminary Control Tests

Two haptic effects were implemented:

- *walls* as they require displaying high stiffness and low friction at the same time
- *springs*, which require displaying both resistive and active forces.

Spring

The spring effect is interesting as it requires rendering active and resistive forces in both directions. To set an output torque t_{set} on the HUCA output, the clutch must be *slipping*. For the sample k , the motor velocity ω_{usm} is used to define the direction of the output torque t_{huca} , while the limiting friction torque t_{lim} defines the amplitude of t_{set} :

$$\begin{cases} t_{lim}(k) = |t_{set}(k)| \\ \omega_{set}(k) = K_v t_{set}(k) \end{cases} \Rightarrow t_{huca}(k) = \text{sgn}(\omega_{usm} - \omega_{huca}) |t_{set}(k)| \quad (6.3)$$

where K_v is a chosen constant. The value set to ω_{set} is chosen proportional to t_{set} . The inertia has been neglected in the expression of t_{huca} for simplicity reasons. The virtual spring is obtained by setting a spring torque to t_{set} :

$$t_{set}(k+1) = -K\theta_{huca}(k) \quad (6.4)$$

where K is the stiffness of the virtual spring and θ_{huca} is the position of the knob. Unfortunately in the haptic knob, there is only one encoder to measure θ_{huca} . ω_{usm} and t_{lim} can only be indirectly observed by their command signals u_{usm} and u_{lim} . Fig. 6.3 shows the position of the knob and the command signals of the HUCA rendering a spring while in interaction with a user. The implementation of the spring demonstrates that the HUCA with the *slipping clutch* can be controlled by impedance.

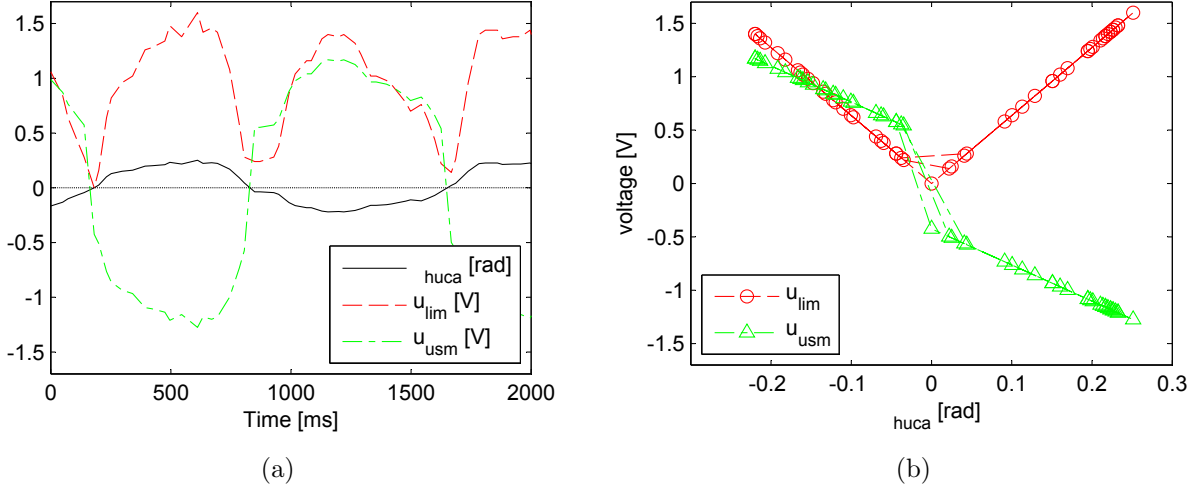


Figure 6.3: Implemented spring (a) the knob position θ_{huca} and actuator input voltages (u_{lim} for the clutch and u_{usm} for the USM) along the time, (b) the actuator input voltages along the knob position.

Wall

The virtual wall effect is ideal to test the impedance range that the HUCA can render. The free motion outside the walls corresponds to null impedance while the contact against a stiff wall is equal to infinite impedance.

In this effect, there is no active force, the USM is turned off. Two virtual walls have been implemented between $\pm 2\pi/10$ rad on the haptic knob. The clutch is *slipping*, between these two walls and is *locked* when the position of the virtual walls is reached. To avoid the feeling

of a sticky wall, the clutch is released when it detects the backward motions allowed by the compliance of the timing belt. This is the equation determining t_{lim} for the positive wall at the next sample $k + 1$:

$$\begin{cases} t_{lim}(k + 1) = t_{lim_{max}} & \text{if } \theta_{huca}(k) \geq \theta_{wall} \text{ and } \omega_{huca}(k) \geq 0 \\ t_{lim}(k + 1) = 0 & \text{otherwise} \end{cases} \quad (6.5)$$

where $t_{lim_{max}}$ is the maximum limiting friction torque and θ_{wall} is the wall position. Fig. 6.4a shows the knob position during the wall effect. The flat surfaces on the curves correspond to the knob reaching the wall.

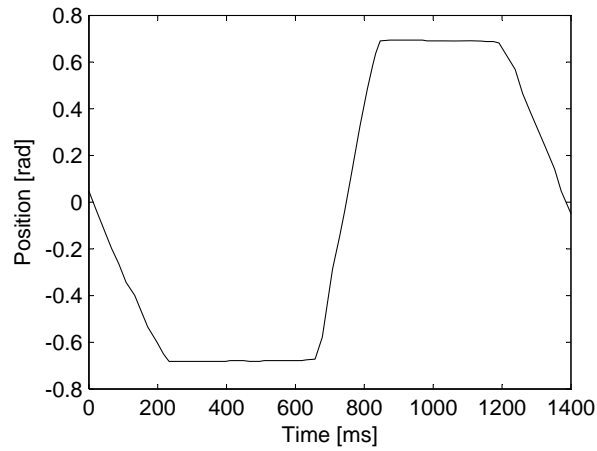


Figure 6.4: Knob position θ_{huca} along the time while the HUCA renders walls.

The wall effect shows that the switching between the operating modes is an efficient way to render very low and very high impedances with the HUCA.

6.1.3 Conclusion

In this haptic knob, the differential-brake used as a clutch has run as expected. Impedance control with a unique position sensor on the HUCA output has been successfully performed. The wall effect has shown the ability of the HUCA to render a large range of impedance by changing its operating modes. With these different implemented effects, the HUCA has shown interesting haptic properties not only for the MR-compatible application, but also for haptics in general.

However, the HUCA requires a second position sensor and an additional torque sensor in order to operate with its full possibilities. The USM has been placed over the timing belt transmission to limit the influence of the transmission friction on the knob. The modification has been done on the second version of the non MR-compatible haptic knob (Fig. 6.5).

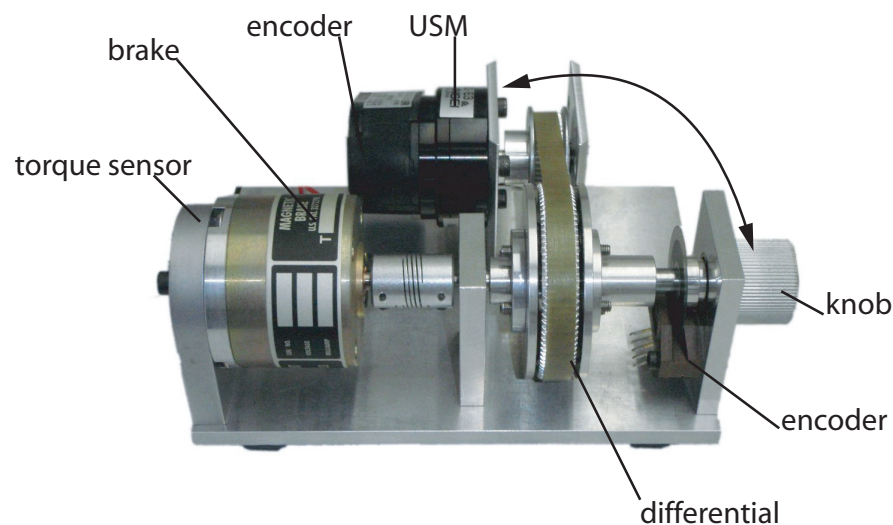


Figure 6.5: Photography of the second version of the haptic knob with a powder brake. The main differences with the previous versions are the inversion of the position of the USM with the position of the knob (to reduce the friction between the brake and the output) and the added encoder and torque sensor.

6.2 MR-Compatible Haptic Knob

The MR-compatible haptic knob requires important developments. A torque sensor is required to know the output torque when the clutch is *locked*. An MR-compatible force-controlled clutch must be developed and integrated into the HUCA. Its design must be adapted to an use in a MR environment.

6.2.1 Design

A compact design using a cylindrical base has been chosen for the MR-compatible haptic knob. Except the powder brake, the standard components of the non MR-compatible version can be reused.

Cylindrical Base

The MR-compatible haptic knob is conceived for fMRI studies. It must be compact to be placed at the entrance of the scanner bore. In the MR-compatible version, the different HUCA components are mounted concentrically into a cylindrical base. This design has several advantages:

- The cylinder gives a good concentric reference to the axis of each component, eliminating the need for couplings. The system is simplified and the moving inertia is reduced.
- A cylindrical base has a good torsional stiffness to support the reaction torques of the HUCA actuators.
- The housing diameter matches standard cylinders dimensions reducing manufacturing operations.

With the cylindrical base, the size of the setup is reduced, and the HUCA resembles a gear box mounted on a motor (Fig. 6.6(a)).

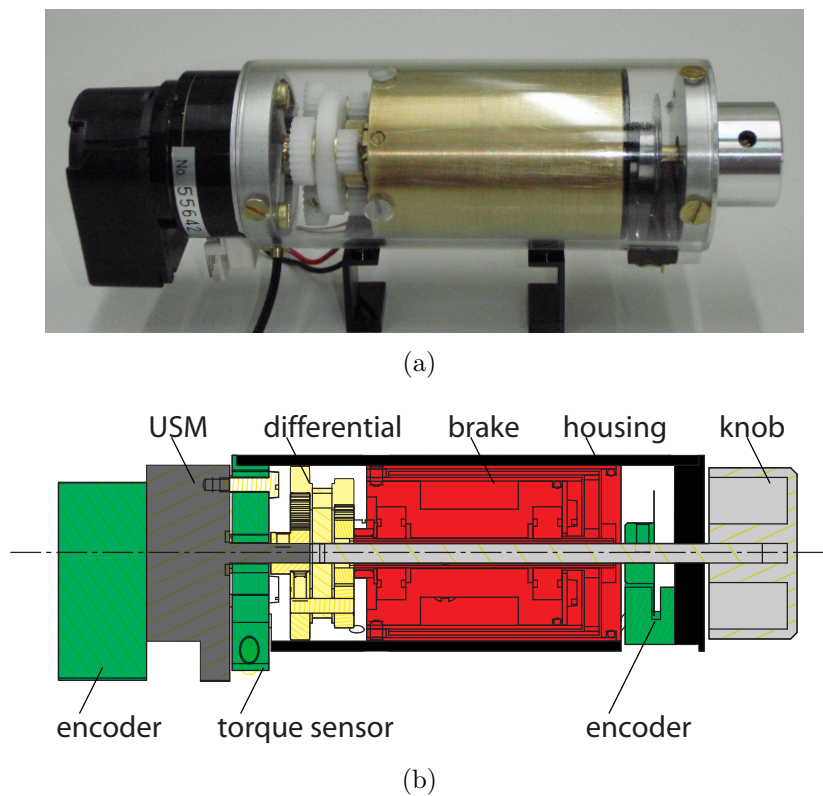


Figure 6.6: fMRI compatible hybrid actuator for interaction with the fingers. Actuator diameter: 40 mm, length: 132 mm without the knob. (a) Picture, (b) cross-section view with the placement of the different components. The output shaft of the HUCA passes through the brake.

Standard Components

The MR-compatible HUCA uses the following standard components. The USM is a USR30-E3N (Shinsei Corporation Inc., Japan) MR-compatible ultrasonic motor. To measure the positions of the HUCA, optical encoders from Agilent Technologies, Inc., USA. have been used:

- on the HUCA output, an optical encoder HEDS-9100 with an optical disc HEDM-5120, (1000 *cpr*)
- on the USM, an optical encoder HEDS-5540, (500 *cpr*).

Optical encoders can be used in MR-environment, if their wires are properly shielded and filtered [Gassert 08b].

6.2.2 MR-compatible Torque Sensor

An MR-compatible torque sensor has been developed and added to the hybrid actuator in order to measure the torque applied by the subject at the output.

Because the rotation of the knob is unlimited, the torque sensor cannot be mounted on the output. The torque sensor then has been placed between the USM and the mechanical ground (Fig. 6.6(b)). It must be adapted to the torque range of the USM, which lies between 50 *mNm* (rated torque) and 100 *mNm* (maximum torque).

The torque sensor is based on the optical measurement of the deflection of an elastic body [Chapuis 04]. The light intensity reflected on the receiving fiber varies with the motion of a mirror placed on the moving part of the elastic body (Fig. 6.7(a)). The optical head including the emitting and receiving optical fibers is a FUE999C1004 (Baumer Electric AG, Switzerland) with a high sensitivity range of 0.5 *mm*. The radial position of the optical head (14 *mm*), its high sensitivity range and the wanted measurement range of ± 0.1 *Nm* determine the stiffness of the elastic body $K_{sens} = 5.6$ *Nm/rad*. The elastic body is made of aluminum and has been machined by Electric Discharge Machining (EDM). This process allows to achieve very thin blades relative to their height (for this torque sensor 0.31 *mm* \times 7.5 *mm*) producing elastic bodies with very low cross-sensitivity.

Its calibration requires positioning the mirror in the middle of the high sensitivity range; this is done for practical reasons by adjusting the position of the optical head. The gain of the light amplifier FWDK 10U84Y0 (Baumer Electric AG, Switzerland) must be set to avoid saturation in the measuring range. In Fig. 6.8, the calibration curve of the torque sensor is shown. The gain of the light amplifier has been set for a torque range of ± 50 *mNm*. The torque sensor shows a non-linearity of less than 2.5%.

The transducing principle used in this torque sensor is well adapted for large torques or force applications like the interaction with the arm movements [Gassert 06a]. Because the deflection is imposed by the high sensitivity range of the optical head, this can lead to

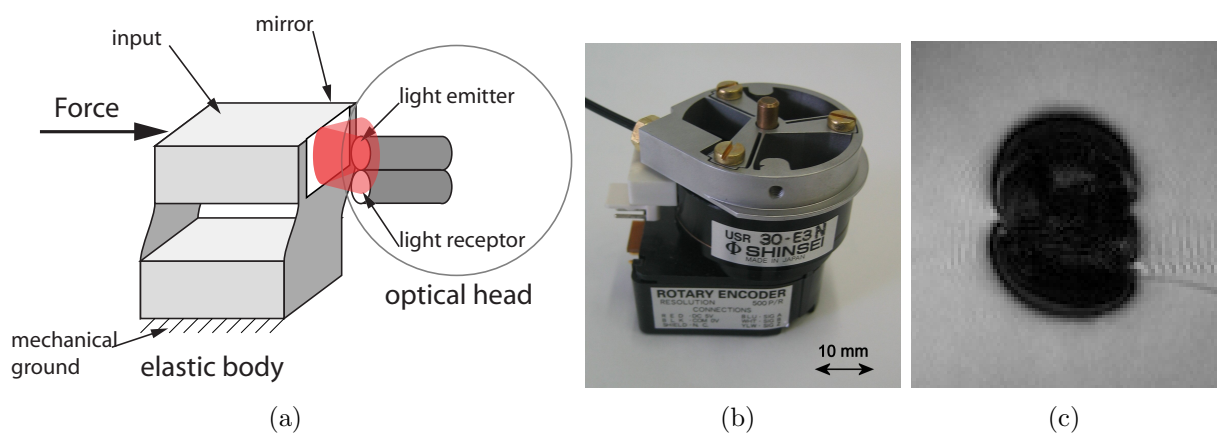


Figure 6.7: MR-compatible torque sensor. (a) Principle, the deflection of the elastic body is measured with the reflected light intensity. (b) The developed torque sensor is designed to be mounted on the USR30. (c) MR image of the torque sensor immersed in a gadolinium-doped aqueous solution imaged with a GE-sequence, reprinted from [Gassert 08b].

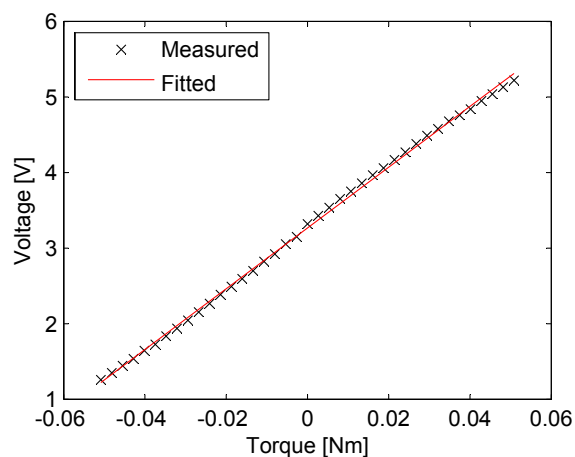


Figure 6.8: Calibration curve of the torque sensor developed for the USR30. The gain of the light amplifier has been adjusted for an operation between ± 0.05 mNm.

a too compliant elastic body for small ranges. In this case a method based on the strain measurement should be preferred.

Because the electronics of the torque sensor is outside the MR room, its constituting materials (aluminum and brass) determine its MR-compatibility. The electrical conductivity of these materials dims locally the RF pulses, thus preventing from the imaging of the neigh-

boring area (Fig. 6.7(c)). Because this effect is local, the torque sensor can be used outside the scanner bore, if its motion is limited.

6.2.3 ERF Differential-Brake

The MR-compatible clutch is the most important component in the HUCA as it modifies the output characteristics of the USM.

Actuation Principles

In addition to the semi-active actuation principle, some of the active principles presented in section 2.3 can be used to control the friction force inside the clutch by changing the normal contact force between the moving surfaces.

ERF This is the only MR-compatible semi-active actuation principle. Because the resistive force is created by the shear stress inside a fluid, this principle has a good property to the wear and low force ripples.

Electrostatic The attracting force between two electrodes is controlled by their electrical charge. The electrodes are made of flexible print circuit boards and rub on each other. Because the Coulomb force is weak, the insulator layer must be very thin making it sensitive to the wear.

Static Piezoelectric If the piezoelectric actuator is used in a clamp, its small strain (about 0.1 %) requires a movement amplification mechanism, as well as an accurate adjustment between the actuator and the moving parts. A drum brake has been realized with this principle [Gogola 99].

Reasoning Piezoelectric Another way to control the friction force with a piezoelectric actuator is to use the piezoelectric levitation. The levitation force decreases the normal contact force created by a preloaded spring. This principle has been implemented on a brake [Koyama 07]. It can be applied directly on the USM stator [Choi 00]. However, when the clutch is turned off, the clutch is locked, what is unsafe.

From the different actuation principles suitable to actuate the clutch, the ERF has been chosen, because it is the most promising principle in terms of performances, resistance to wear and safety. For its operation, the ERF requires a housing filled with ERF constituting an important inertia, thus the differential-brake configuration is preferred to the direct clutch.

ERF

The ERF is considered as a Bingham fluid which rheology is modified by the electrical field:

$$\tau = \tau_y + \mu_{pl}\dot{\gamma} \quad (6.6)$$

where τ is the shear stress and $\dot{\gamma}$ is the shear rate. τ_y is the yield stress and μ_{pl} is the plastic viscosity. When an electrical field E is applied, τ_y and μ_{pl} change:

$$\begin{cases} \tau_y = AE^2 \\ \mu_{pl} = \mu_0 - BE^2 \end{cases} \quad (6.7)$$

where μ_0 is the viscosity of the ERF without electrical field. A and B are constants of the ERF. The sought qualities of the ERF are:

- A large variation of τ_y in respect of E , this phenomenon is used to vary the limiting friction torque t_{lim} in the ERF brake.
- A small μ_{pl} , this values makes the output torque sensitive to the velocity variation. It decreases with the electrical field and can even become negative.

In Fig. 6.9, the characteristics of the ERF are drawn. The used ERF is the LID 3354S from Smart Technology ltd., UK. In the brake, the fluid shear stress τ is used to create the braking torque between the rotor and the stator.

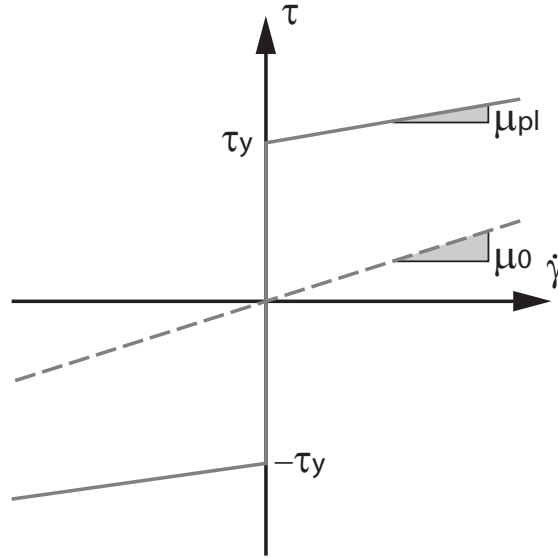


Figure 6.9: ERF fluid characteristics. Its shear stress τ is given in function of the shear rate $\dot{\gamma}$. When there is no electrical field, the ERF is similar to a Newtonian fluid (dashed line) with a viscosity μ_0 . With an applied electrical field, τ_y the yield stress increases and the plastic viscosity μ_{pl} decreases.

The current density of the ERF J can be approximated by a quadratic function of the electrical field E :

$$J = PE + QE^2 \quad (6.8)$$

where P and Q are respectively a linear and a quadratic conductivity constant of the ERF.

Brake

Several modifications and improvements have been brought to the initial ERF brake [Chapuis 06] in order to obtain the operating prototype [Chapuis 08]. This brake has addressed several points, sometimes conflicting:

Torque range of the brake must be similar to the one of the USM. The dimensions of the rotor and the stator (the electrodes) have been determined with Eq. 6.7.

Seals the ER fluid chamber must be tight without creating friction on the output shaft to limit the drag torque. From the different tested joints, axial seals (v-ring) have shown the lowest friction thanks to their higher compliance compared to the radial ones.

Small gap To limit the voltage required to create the required electric field, the gap between the two electrodes (the rotor and the stator) must be small. The mechanical adjustment is critical as any contact between the rotor and the stator will lead to a short circuit. Cylindrical electrodes have been assembled by brazing. This method gives a good accuracy. The achieved gap is 0.5 *mm* on the electrode radius.

Electrical connection The brazing ensures a good electrical connection between the electrodes and their supports. The rotor is electrically connected by a slip ring constituted of a graphite cylinder applied on the rotor shaft. The rotor and its shaft are together connected.

Electrical insulation Short circuits are avoided by using only non conducting materials (polymer and ceramic) around the brake and between the rotor and stator.

The cylindrical base design of the HUCA requires a hollow shaft brake to connect the output knob to the differential (Fig. 6.6(b)). In Fig. 6.10, a CAD cross-section view of the ERF brake illustrates the different adopted solutions.

High Voltage Driver

A high voltage analog amplifier able to deliver several hundreds volts with high dynamics is required in order to power the ERF brake. The maximum voltage to the brake has been limited to 1 *kV*, as it is difficult to find electronic components that can support higher voltage. In this circuit, a DC/DC converter (PHV12-1.0K5000N, Traco Power AG, Switzerland) provides the negative high voltage -1000 *V*, while the voltage applied to the brake u_{brake} is controlled through a high power npn bipolar transistor (BU2525AF, Royal Philips Electronics, Netherlands) mounted in common emitter configuration. Because this transistor has a low base-emitter current gain (~ 13), an operational amplifier (OPA131P, Texas Instruments

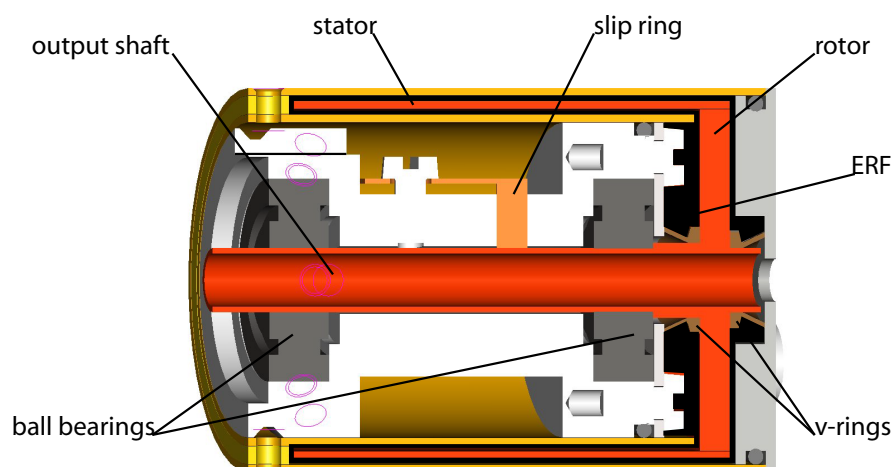


Figure 6.10: Cross section of the ERF brake. The space occupied by ERF is in black.

Inc., USA) has been added on the transistor base to increase this gain and to compensate for the base-emitter voltage V_{BE} . An insulation amplifier (ISO122P, Texas Instruments Inc., USA) is used to insulate and shift the input signal to the negative high voltage (Fig. 6.11).

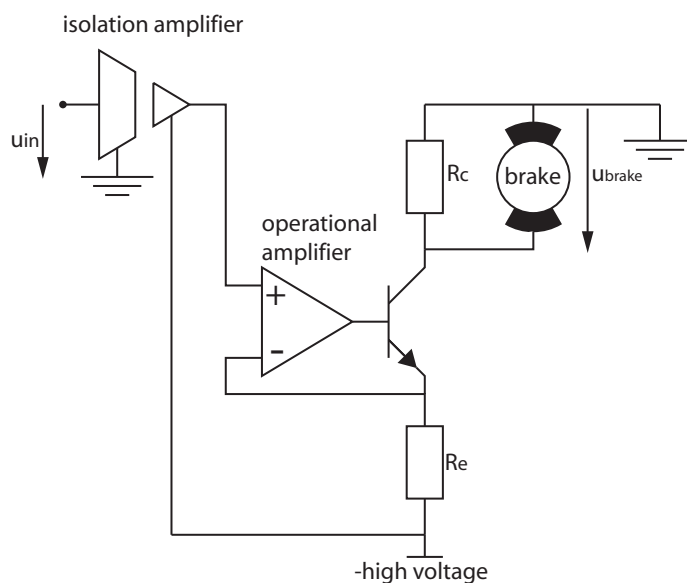


Figure 6.11: Simplified electronic schematic of the high voltage driver.

Measurements

The ERF brake and the high voltage driver characteristics must be identified first, because the torque range of the brake influences the design of the differential.

The voltage u_{brake} applied to the brake by the driver shows a linear behavior with a maximum voltage of 947 V (Fig. 6.12). At the maximum voltage the current in the brake i_{brake} is about 0.446 mA a low value favorable for a use in a MR environment. In the non saturated part, the non-linearity is about 9% of the output range.

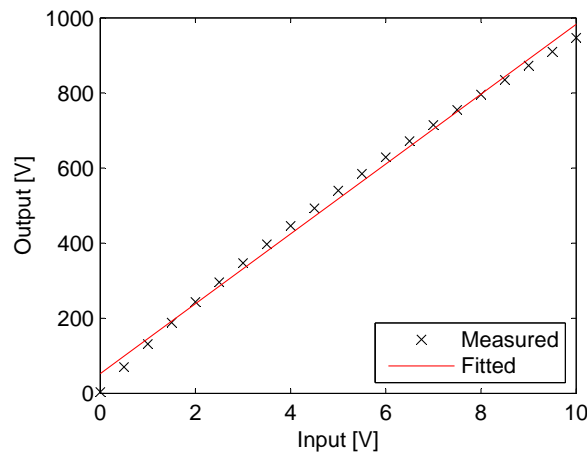


Figure 6.12: Output voltage u_{brake} in function of the command signal u_{in} of the HV-driver with the ER brake connected.

The limiting friction torque t_{lim} of the ERF brake has been measured with a dynamometer. Because there is a difference between the static and the dynamic limiting torque, the following response is given for the dynamic torque. They have been measured while the brake was *slipping*.

Fig. 6.13(a) shows the torque response t_{lim} of the brake to the applied brake voltage u_{brake} , this curve is a combination of a quadratic response at low voltage and saturation at high voltage. The response t_{lim} in function of the applied brake current has a better behavior (Fig. 6.13), that can be approximated with a quadratic function. The maximum dynamic t_{lim} is of 68.7 mNm, while the maximum static t_{lim} has been measured at 176 mNm. The drag torque has been estimated of about 5 mNm. A shunt resistor has been integrated in the driver to allow the control of the brake current I_{brake} .

As the maximum static t_{lim} is too high compared to the USM one, they must be adjusted. A solution could be to build a smaller ERF brake. However its fabrication is difficult, thus the torque adaptation by the differential is the best solution.

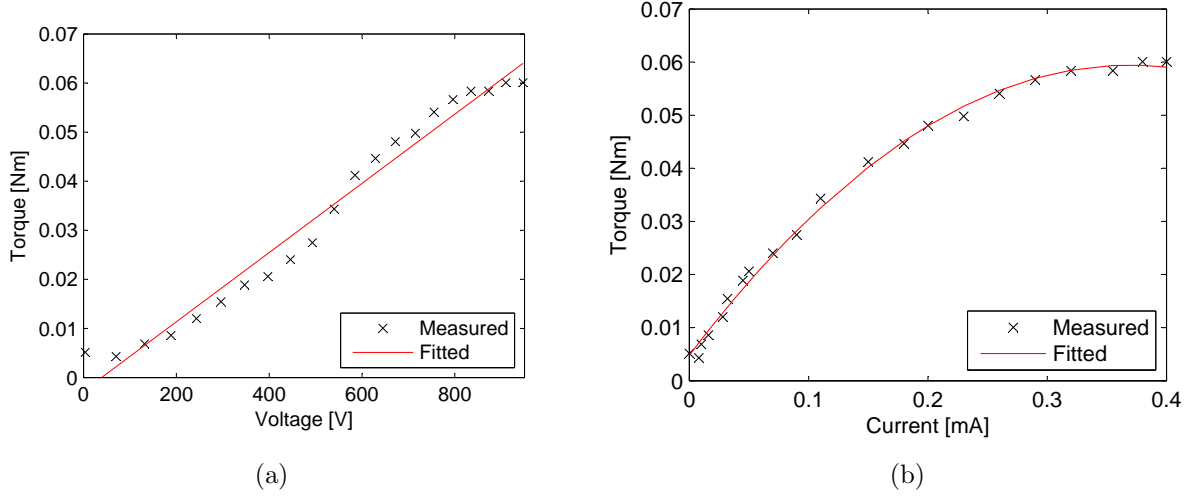


Figure 6.13: Response of the dynamic brake torque t_{lim} , (a) in function of the voltage u_{brake} applied to the brake and (b) in function of the brake current i_{brake} .

Epicyclic Differential

The brake torque range is adapted to that of the USM by changing the transmission ratio of the differential gear. This will change the braking torque and the USM torque reflected on the HUCA output.

With the differential (Fig. 6.14(b)), the HUCA velocity and torque are given by the following equations:

$$\begin{cases} \omega_{huca} = \frac{1}{n_{usm}}\omega_{usm} + \frac{1}{n_{brake}}\omega_{brake} \\ t_{huca} = n_{usm}t_{usm} = n_{brake}t_{brake} \end{cases} \quad (6.9)$$

where n_{usm} , ω_{usm} and t_{usm} are the respective gear ratio, the velocity and the torque of the USM, and n_{brake} , ω_{brake} and t_{brake} are the gear ratio, the velocity and the torque of the brake. t_{usm} and t_{brake} are not independent, and their relation can be obtained by combining the two lines of Equ. 6.9:

$$t_{usm} = \frac{n_{brake}}{n_{usm}}t_{brake} \quad (6.10)$$

The gear ratios n_{brake} and n_{usm} must be chosen such that the maximum brake torque given by its maximum limiting torque $t_{lim_{max}}$ reflected on the USM falls between the rated torque $t_{usm_{rated}}$ and the maximum torque $t_{usm_{max}}$ of the USM:

$$t_{usm_{rated}} < \left| \frac{n_{brake}}{n_{usm}} \right| t_{lim_{max}} < t_{usm_{max}} \quad (6.11)$$

In addition to the torque matching conditions, the differential must act as a speed increasing gear for the brake ($|n_{brake}| < 1$) and as reduction gear for the USM ($|n_{usm}| > 1$).

To achieve this, the friction wheel differential in [Chapuis 06] has been replaced by an epicyclic gear differential. It is composed of two epicyclic gears which planet gears are connected by the same shaft to a common planet carrier-crank arm. The two sun gears are the respective input of the USM and the brake, while the carrier-crank arm is the output of differential (Fig. 6.14(b)). The obtained gear ratios are $n_{usm} = -1.58$ and $n_{brake} = 0.61$. These values meet the requirements of Equ. 6.11. The change of the gears ratios have the beneficial effect to reduce the brake inertia I_{cl2} reflected on the output of the HUCA.

Measurements have been carried out to evaluate the differential-brake characteristics. The minimum displayable torque of the HUCA is determined by the brake drag torque reflected on the output t'_{limmin} that has been reduced to approximately 2.7 mNm with the epicyclic differential. The transmissible torque created by the entire system is limited at a maximum of 94.4 mNm by the mechanical constraints on the differential.

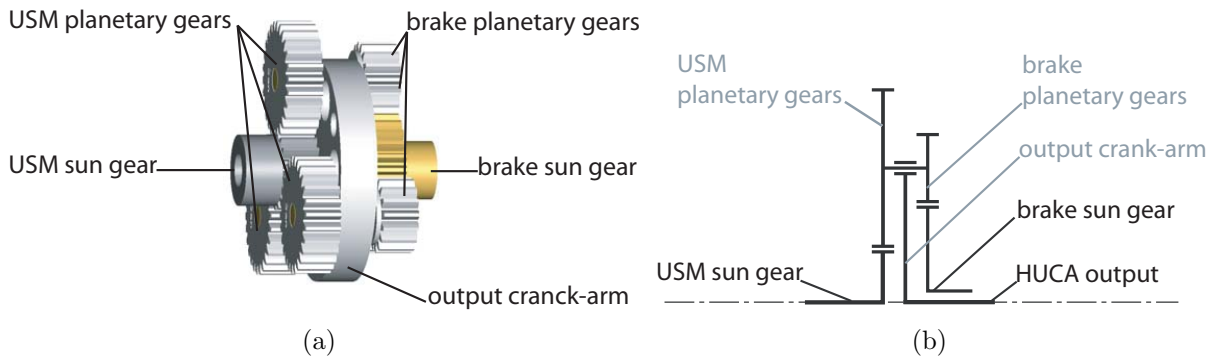


Figure 6.14: (a) Epicyclic differential. (b) Scheme of the differential arrangement.

6.2.4 MR Compatibility Testing

The MR-compatibility of the entire hybrid actuator has been tested inside a 3T MR system (Siemens Allegra) at the University Hospital in Basel, Switzerland. The GE-EPI¹ sequence has been used to produce the images required by the tests. A first test performed with only the ERF brake has investigated the effect of the high voltage on the MR environment. A square signal u_{brake} of 1 Hz frequency oscillating between $0 - 990 \text{ V}$ (the maximum driver voltage) has been applied to the brake placed at the entrance of the scanner bore. This position corresponds to the hand region, where the HUCA should be typically placed during experiments. No noticeable influence on the image quality could be found.

¹The GE-EPI (Gradient Echo-Echo planar) is a fast imaging sequence used for fMRI studies.

A second series of tests has been performed with the USM and the ERF brake operating alternatively and simultaneously. In neither of these tests, the imaging quality has been affected by the operation of the USM and the ERF brake. The compatibility has been assured by using low-pass filters adapted to the high voltage power. The result of the statistical test is presented in Fig. 6.15. The Fig. 6.16 show the subtraction of two slices: the operation of the HUCA does not create noticeable change between the two slices. Then it is MR-compatible.

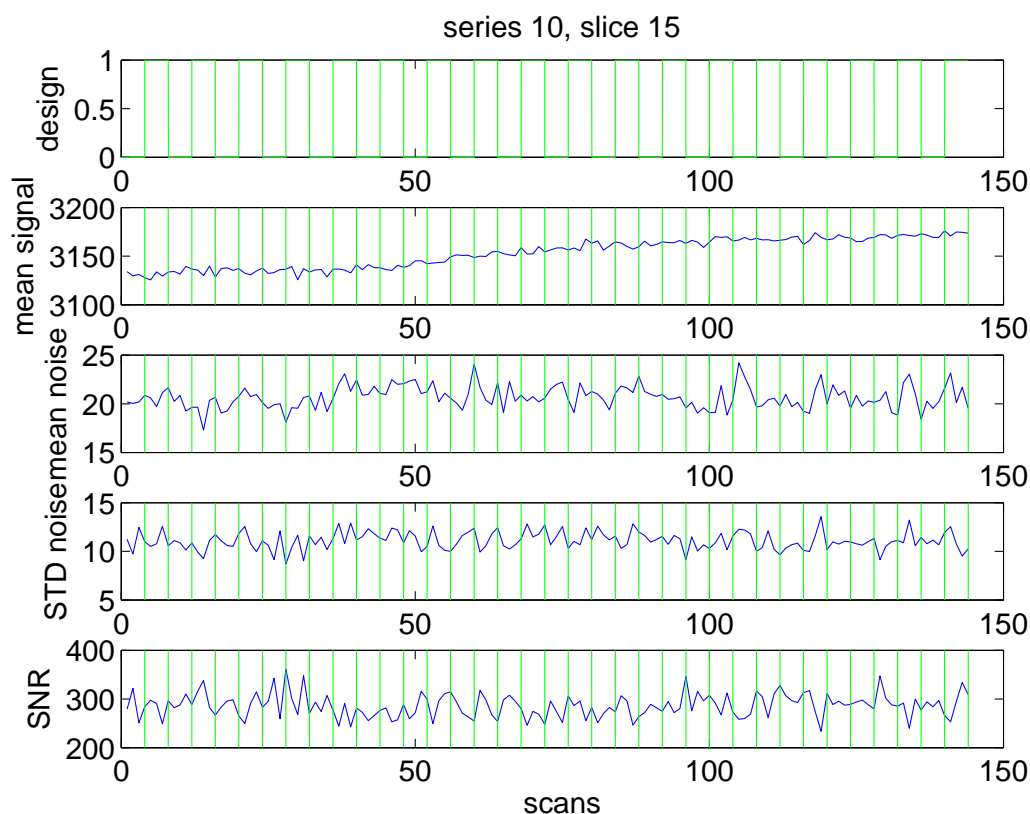


Figure 6.15: Results of the phantom compatibility test with the HUCA. The first row shows the block design, consisting of 18 repetitions of a 10 s rest condition, followed by a 10 s condition of either the powered ERF brake, the actuated ultrasonic motor, or both. The mean of the signal of an 11×11 voxel square located in the center of the image (row 2) was divided by the standard deviation of an 11×11 voxel square in the lower left corner of the image (STD noise, row 4) to obtain the SNR time-series (row 5). A t-test between the SNR in the rest and active conditions revealed no significant difference between the two conditions ($p = 0.55$).

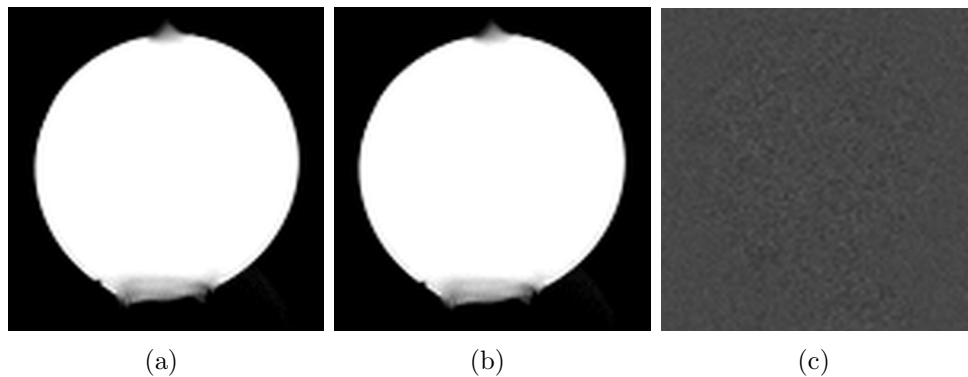


Figure 6.16: Comparison of the slides extracted from the statistical MR-compatibility test series, Fig 6.15. The slice from the active condition (a, the HUCA is operating) shows no RF interference. The slice of the rest condition (b, the HUCA turned off) shows neither shifts nor deformations. Their subtraction doesn't show difference even with an increased contrast (c).

6.2.5 Conclusion

The different critical points of the development of the MR-clutch have been addressed, by an appropriate design of the ER brake, by the development of a high voltage analog amplifier driver and by the use of an epicyclic differential to adapt the torque range of the different HUCA actuators. This differential has the beneficial effect to reduce the reflected inertia and the drag torque of the brake on the HUCA output.

The haptic knob has been tested in an MR-environment. It is able to run properly at the entrance of the scanner bore and its operation does not disturb the imaging of the scanner, demonstrating its MR-compatibility.

6.3 Conclusion

The non MR-compatible haptic knob has been rapidly developed thanks to the use of standard components and has shown the ability of the HUCA to be controlled in impedance. While the MR-compatible version has required more developments including a dedicated torque sensor, an electrorheological brake and an epicyclic differential to adapt the torque of the brake to the USM. The MR-compatibility of the prototype of the HUCA has been validated. The two requirements of the HUCA have been verified on two distinct versions, and then to fully validate the HUCA concept, controls experiments must be run on the MR-compatible prototype.

Chapter 7

Evaluation of the Performances

The HUCA must be controlled in order to evaluate its performances. The characteristics of its actuator are identified in order to implement efficient closed-loop velocity and torque controls. With these control schemes, impedance and admittance control can be implemented and the displayable impedances can be studied. The transparency and the capacity of the HUCA to display hard walls are studied and finally its performance are compared to a hydrostatic transmission one. Because of different gear ratios in the HUCA, the control values will be expressed seen from the output, the reflected values on the output will be marked with a " ' " .

7.1 Setup Configuration

These experiments have been done with the MR-compatible haptic knob presented in the section 6.1. The connection of the HUCA components with the control system is illustrated in Fig. 7.1.

The *high-voltage driver* powers the brake, while the USM is controlled by the *USM driver* D6030 (from Shinsei Corporation Inc., Japan). The control has been implemented on a PC equipped with a *DAQ card* NI-PCI6052E (from National Instrument Corp., USA), in addition an *encoder card* APCI-1710 (from ADDI/DATA GmbH, Germany) is used to read the HUCA encoders. To protect the USM driver from wrong manipulations, a *protection circuit* has been added between the *DAQ card* and the *USM driver*. Its operation is described in the subsection 7.2.1. The control software is implemented using Simulink XPC-target from Mathworks, it has been preferred to Labview thanks to its higher and more precise sampling rate. The sampling time T_s used for the control loop is 1 *ms*.

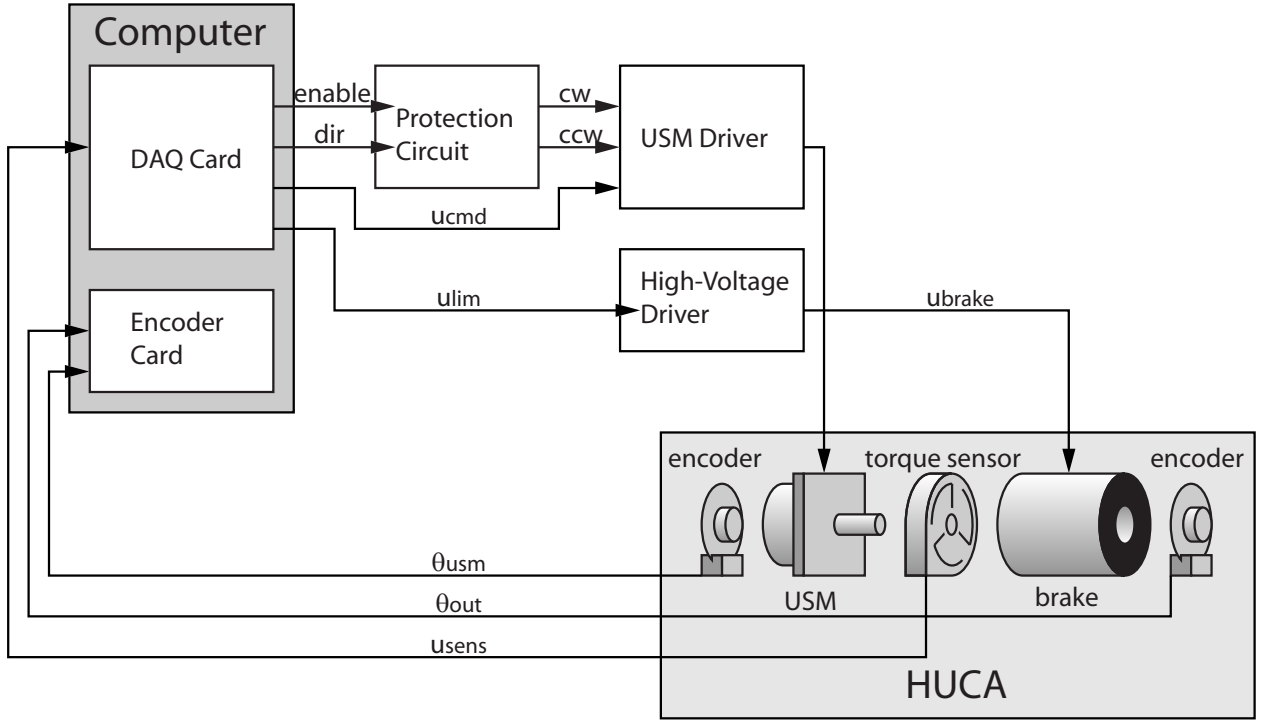


Figure 7.1: Connection of the HUCA to its control system.

7.2 Velocity control

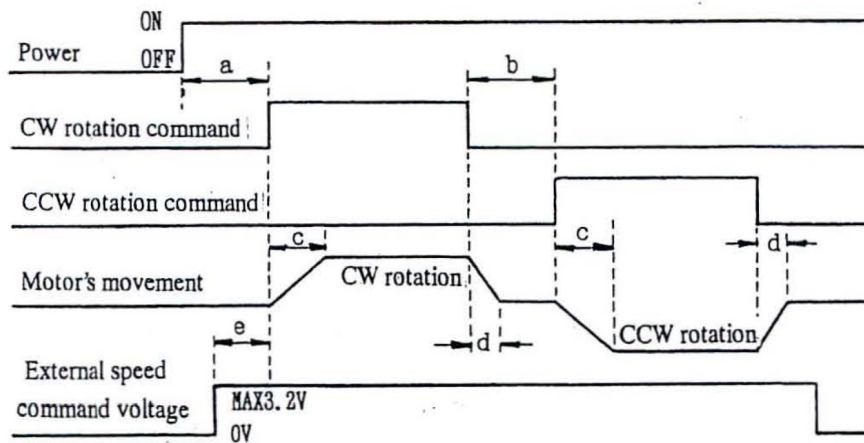
The achievable performance of the closed velocity control depends mainly on the open loop characteristic of the USM and its driver. It is important to characterize them in order to design the appropriate velocity controller. The experiments have been performed with the HUCA with the *locked clutch* and the output free.

7.2.1 USM Characteristics

The USM driven by the D6030 has the particularity to be controlled by 3 different signals. Two are digital signals that each enables a rotation direction, clockwise *CW* or counterclockwise *CCW*. The last is the command voltage u_{cmd} , a positive analog signal controlling the USM velocity. These three signals are calculated from the signal u_{usm} :

$$\begin{cases} CW = true, & CCW = false & \text{if } u_{usm} < 0 \\ CW = false, & CCW = false & \text{if } u_{usm} = 0 \\ CW = false, & CCW = true & \text{if } u_{usm} > 0 \\ u_{cmd} = |u_{usm}| \end{cases} \quad (7.1)$$

The command signals CW and CCW , determining the rotation direction, have to respect a particular timing, illustrated in Fig. 7.2, otherwise the USM driver may be damaged. A dead time of 10 ms must be introduced in the command signals before switching direction of the USM. The time required by the USM to start (the starting response time) is of about 50 ms , while the time needed to stop (the stopping response time) is of about 1 ms . With these different time constants, the time required to reverse the rotation direction is $\sim 60 ms$ meaning that an alternative signal with a period smaller than 120 ms will be canceled. This gives a theoretical bandwidth of 8.3 Hz , however if the signal has a constant sign the bandwidth achieved is much higher.



- a) 100msec or more time duration is required from driver power source ON to CW/CCW start command ON.
- b) 10msec or more time interval is required when switching from CW to CCW or vice versa.
- c) Starting response time (under no inertia load) is approximately 50msec.
- d) Stopping response time (under no inertia load) is approximately 1msec.

Figure 7.2: Time chart of the USM driver D6030 reprinted from www.shinsei-motor.com.

In order to see the dynamic of the USM in open-loop a bias has been added in the command signal to avoid the influence of the time constant. Fig. 7.3(a) shows the bode plot of the USM velocity without the HUCA in function of the command signal u_{usm} . Its response is flat until 20 Hz , and a resonance can be noticed about the 200 Hz .

To get the static gain, a slowly varying ramp signal u_{usm} has been sent to the USM driver, Fig. 7.3(b) shows the velocity response in steady state.

The velocity response of the system shows four distinct behaviors depending on the absolute value of u_{usm} .

- **Dead zone** Below $u_{usm_{min}}$, the velocity of the USM is null.
- **Hysteresis loop** Between $u_{usm_{min}}$ and $u_{usm_{start}}$, the USM starts to rotate only if $u_{usm_{start}}$ is reached and its velocity is $\omega'_{usm_{start}}$. Smaller velocity can be reached by decreasing u_{usm} when the USM is already rotating.
- **Linear zone** Between $u_{usm_{start}}$ and $u_{usm_{max}}$, the velocity is proportional to u_{usm} with the following relation:

$$\omega'_{usm} = G'_{usm}(u_{usm} - \text{sgn}(u_{usm})u_{usm_{min}}) \quad (7.2)$$

where G'_{usm} is the velocity gain of the USM reflected on the output.

- **Saturation** Over $u_{usm_{max}}$, the USM velocity doesn't increase any more.

The different experimental threshold voltages and related velocities are summarized in Table 7.1.

Table 7.1: Experimental command voltages and related reflected velocities determining the different behaviors of the USR30 USM.

Index	$ u_{usm} [V]$	$ \omega'_{usm} [rad/s]$
<i>Dead zone</i>		
min	0.27	0
<i>Hysteresis loop</i>		
start	0.75	5.3
<i>Linear $G_{usm} = 11.0 \text{ rad/s}$</i>		
max	2.39	23.3
<i>Saturation</i>		

The USR30 used with the driver D6030 has a high bandwidth and a linear characteristic for medium and high velocities. Its performances are degraded at low velocity where hysteresis loops and dead zone occur. The time required to start the motor or to reverse its rotation direction limit the frequency of the alternative input signal. This limitation is specific to the D6030 as with the high-performance USM driver [Bullo 02] these response times are much smaller.

7.2.2 Closed-Loop Control

The non-linearities of the USR30 at low velocity can be reduced by using a closed-loop velocity control. A proportional velocity control has been implemented, the main difficulty is the estimation of the velocities from the measured position. Because the HUCA is equipped with

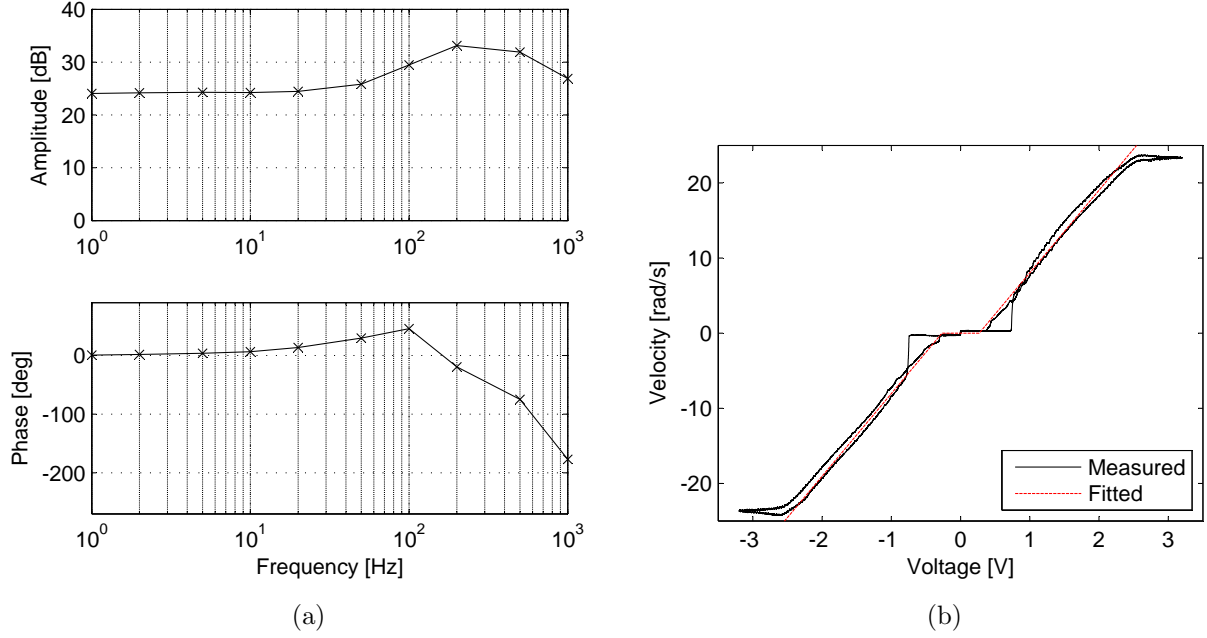


Figure 7.3: (a) Bode plot of the USM velocity in function of the command signal u_{usm} , a offset has been added to avoid the influence of the dead time and starting response time. (b) Steady state HUCA output velocity ω_{huca} response in open-loop to the command signal u_{usm} sent to the motor driver D6030, with the *locked clutch*.

optical encoders measuring a position, the estimated velocity ω_e is calculated with a finite differentiation. Its resolution r_ω depends on the ratio of the optical encoder resolution r_θ with the sampling time T_s :

$$r_\omega = \frac{r_\theta}{T_s} \quad (7.3)$$

With a 500 *cpr* optical encoder used in quadrature, a gear ratio n_u of 1.58 and a T_s of 1 *ms* the velocity resolution reflected on the output is $\sim 2 \text{ rad/s}$. In addition to this low resolution, the high-frequency digital noise due to the increments of the encoders degrades the estimated velocity signal preventing the increase of the proportional gain. To address this problem, two features have been added to the velocity control:

- A low-pass first order filter has been included into the finite differentiation [Longchamp 95]:

$$\omega_e(k) = \frac{\theta_m(k) - \theta_m(k-1) + \tau\omega_e(k-1)}{\tau + T_s} \quad (7.4)$$

where ω is the estimated velocity, θ_m is the measured position and τ is the time constant of the filter. A τ of 100 *ms* has been chosen in this system. This filter increases the

resolution $\sim 0.02 \text{ rad/s}$ of the estimated velocity and suppress the high-frequency noise due to the encoders increments.

- To decrease the required proportional gain, a static feed-forward term has been added.

With these two features a proportional gain K_p of 25 can be used in the velocity control. A dead zone has been added to prevent limit cycles for velocity near from zero.

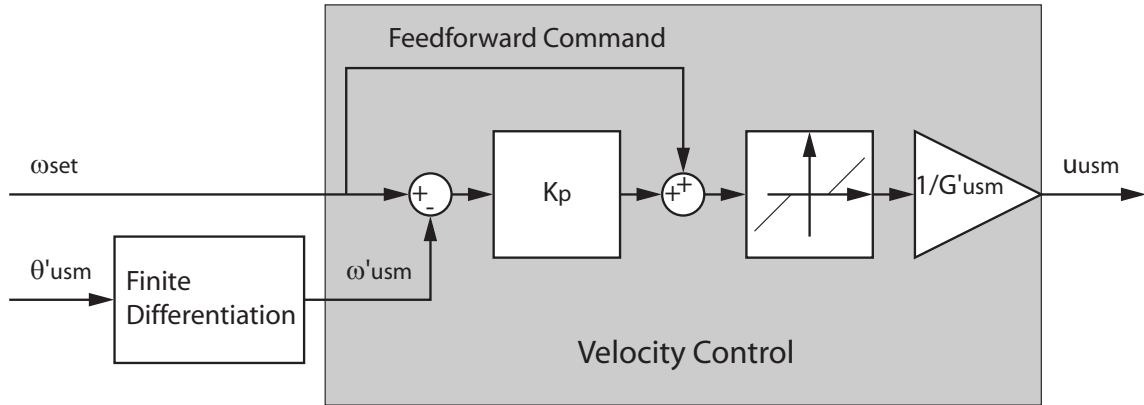


Figure 7.4: USM velocity control scheme. The finite differentiation include a first order low pass filter to remove the noise of the encoder increment and to increase the USM estimated velocity ω'_{usm} resolution. A feed-forward command is added to decrease the required proportional gain.

7.2.3 Performances

The static response of the USM in closed-loop is evaluated by sending a slowly varying ω_{set} . In Fig. 7.5(a), the velocity of the HUCA ω_{huca} with the locked clutch is reported in function of ω_{set} . Compared to the open-loop response Fig. 7.3(b), the response is more linear, and non-linearities occurs for velocity below 0.55 rad/s (Fig. 7.5(b)) instead of the 5.3 rad/s in open-loop. Its step response shows asymmetric response between the start time constant 61 ms and its stop time constant 31 ms , this is consistent with the time chart of the D6030 (Fig. 7.2). Fig. 7.6(b) shows a time response for a given frequency, the USM can follow the sine, except for low velocities where small bumps can be observed. The harmonic response of the output of the HUCA in closed-loop velocity control has been reported in Fig. 7.7. The bandwidth of the system in closed-loop is of about 5 Hz for a signal without offset and of 10 Hz for a signal with offset. This bandwidth is low compared to the open-loop bandwidth of the USM. This can be explained by three factors:

- The low encoder resolution requires a low-pass filter with a cutoff frequency of 10 Hz in this case. With a higher resolution encoder the cutoff frequency can be increased.

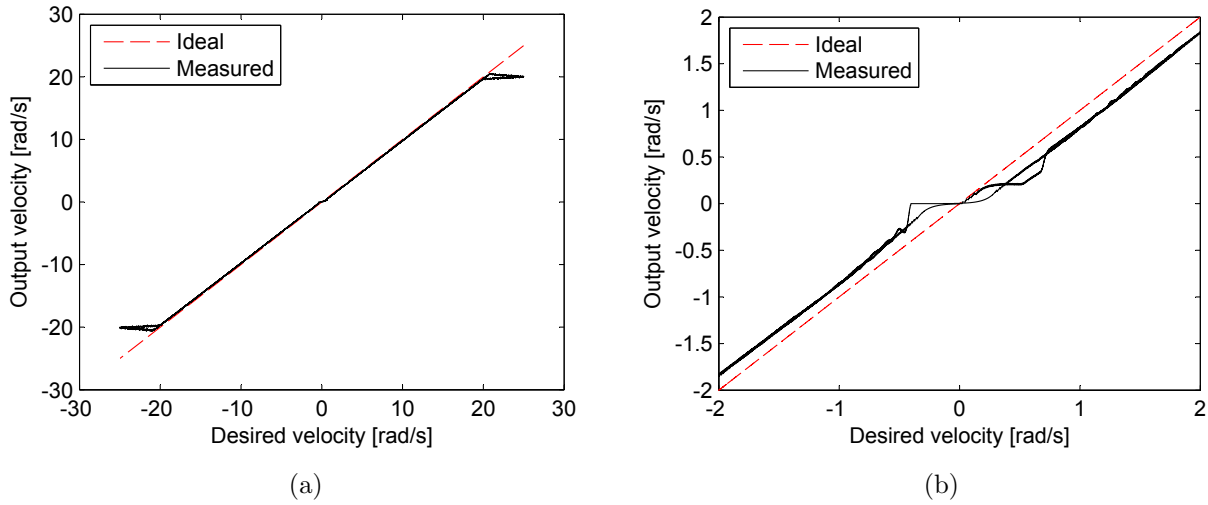


Figure 7.5: (a) Steady state HUCA output velocity ω_{huca} response in closed-loop in function of the desired velocity ω_{set} with the *locked* clutch. (b) Close view of the non-linearities at low velocity.

- For an alternative signal, about 60 *ms* is required to change the rotation direction. The responses of signals above ~ 8.3 *Hz* are null and the bandwidth can in this case not be improved by increasing the low-pass filter cutoff frequency.
- The differential has a 0.09 *rad* (5 deg) play on the output. The HUCA output tends to bounce with a frequency between 10 *Hz* to 20 *Hz*.

The properties of the USM with a close-loop velocity control can achieve more accurate output velocity, thus it will be preferred to the open-loop control in applications of the HUCA.

7.2.4 Conclusion

The closed-loop velocity control of the USM allows to reduce significantly the non-linearities at low velocity, making its use in a series dynamics actuator (cf. section 4.1) interesting. The bandwidth achieved is relatively low, this can not be improved for alternative signals as it depends on the USM driver response times. For constant sign velocity signal, the bandwidth can be increased by reducing the play in the differential and by increasing the cut-off frequency of the low pass filter included in the finite differentiation algorithm.

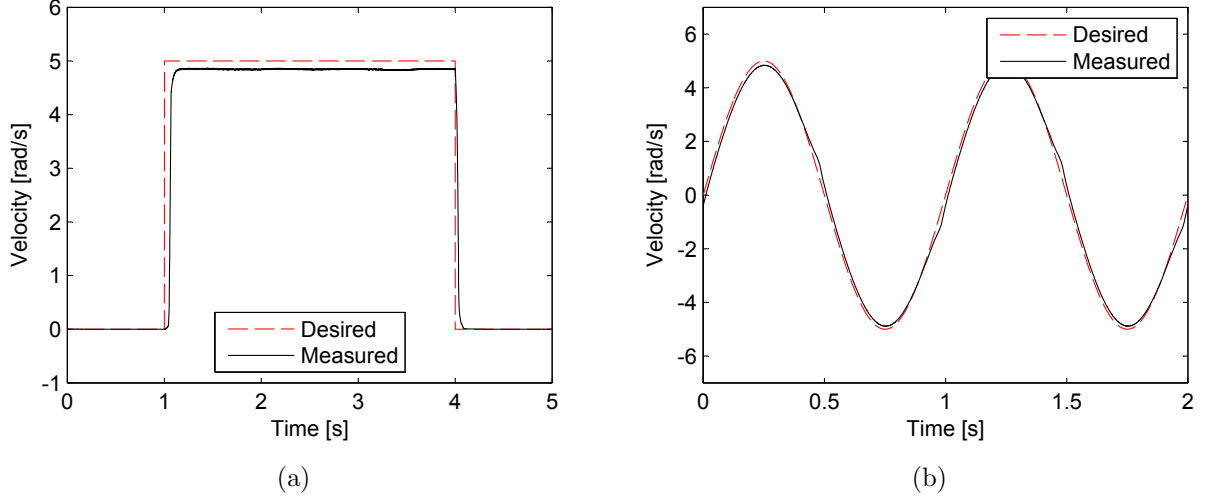


Figure 7.6: (a) Velocity response of the output of the HUCA to a velocity step in closed-loop and with the *locked-clutch*. (b) Velocity response of the output of the HUCA to a velocity sine of 1 *Hz* and 5 *rad/s* of amplitude. The sine is well followed, except at low velocities, small bumps due to the non linearities are observed.

7.3 Torque control

To output an accurate torque, the characteristics of the clutch must be identified. The experiments in torque control have been carried out with the HUCA output locked. The measured torque t'_{sens} is defined in the same direction than the transmitted torque t'_{tr} and the HUCA output torque t_{huca} .

7.3.1 Clutch Characteristics

The clutch in the HUCA is constituted by a differential-brake system. To determine its characteristics, the torque applied by the USM is measured with a sensor. In *slipping mode*, the expression of the clutch transmitted torque t'_{tr} and the HUCA slipping $\Delta\omega'_{cl}$ are derived from Eq. 4.27, 4.25:

$$t'_{tr} = -sgn(\Delta\omega'_{cl})t'_{lim} \quad (7.5)$$

$$\Delta\omega'_{cl} = \omega_{huca} - \omega'_{usm} \quad (7.6)$$

With the output of the HUCA locked, the expressions of the t'_{tr} becomes:

$$t'_{tr} = sgn(\omega'_{usm})t'_{lim} \quad (7.7)$$

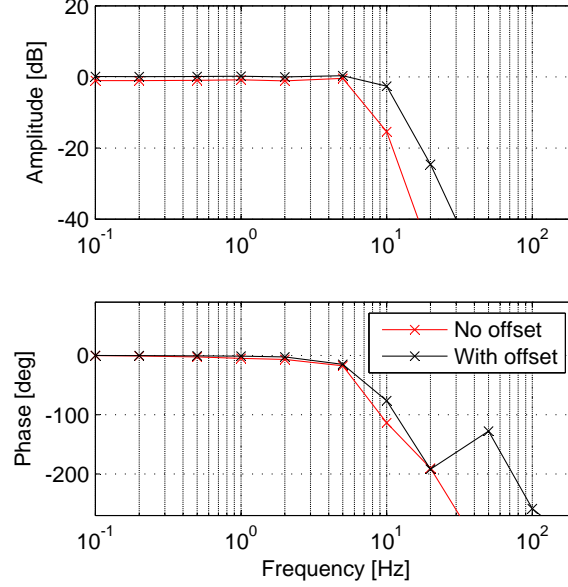


Figure 7.7: Bode plot of the harmonic response of the HUCA output in closed-loop velocity control.

The slipping of the clutch is the opposite of the USM velocity.

To get the static response of the clutch, a command voltage u_{lim} in the range of 0 – 9 V has been applied to the high-voltage driver of the clutch. For each command voltage, the USM rotates at controlled velocities included between 0 to 19 rad/s . In Fig. 7.8, the limiting torque t'_{lim} response in function of the command voltage u_{lim} and the USM velocity ω'_{usm} is illustrated for velocities up to 5 rad/s . For an applied voltage of 9 V, t'_{lim} saturates over 0.05 Nm, thus this curves is not plotted in the Fig. 7.8 for its clarity. As expected, the plastic viscosity is low $|D_{huca}| < 1 mNmrad/s$, the different curves do not show slopes. However the static friction increase faster than the static yield stress, creating for torques above 0.03 Nm stick-and-slip instabilities for low slipping velocities ω'_{usm} :

$$|\omega'_{usm}| > 50 [rad/sNm] t'_{lim} - 0.92 [rad/s] \quad (7.8)$$

This velocity limit is represented in solid line in Fig. 7.8. To avoid these instabilities, the velocity set to the USM has to imposes a slipping larger than this limit:

$$|\omega'_{usm}| = K_v t'_{lim} \quad (7.9)$$

where K_v is a chosen torque velocity gain, its value is fixed equal to 40 rad/sNm . This operation line is represented in Fig. 7.8 in a dash-dotted line. Along this line, the torque gain of the clutch G'_c has been identified equal to 0.0091 Nm/V.

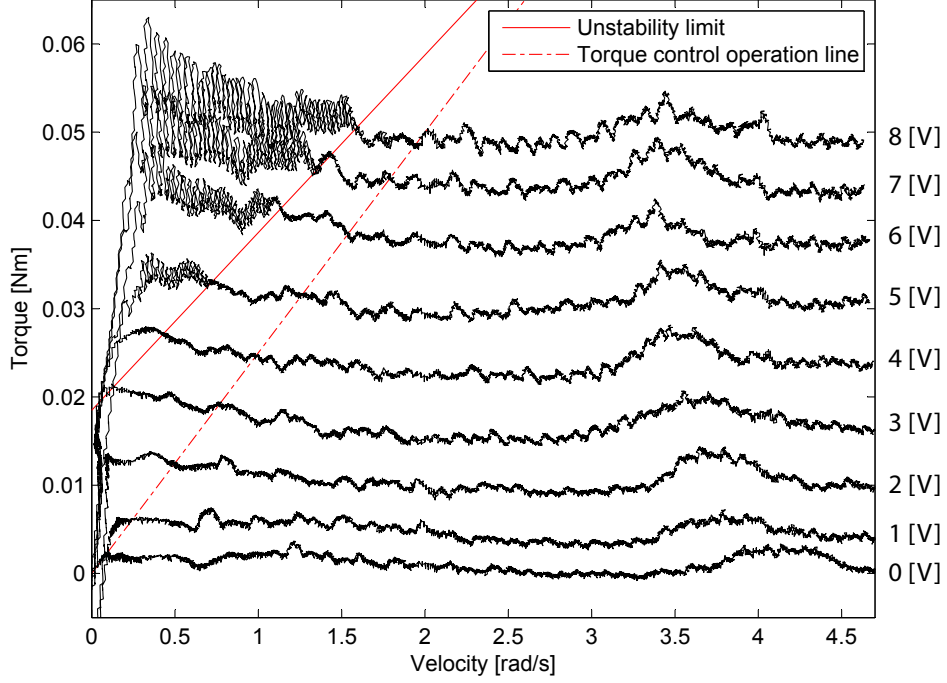


Figure 7.8: Clutch transmitted torque t'_{lim} response for different command voltage u_{lim} and different ω'_{usm} USM velocity while the HUCA output is blocked. The torque-velocity operation used in the torque control scheme is represented in dash-dotted line

7.3.2 Open-Loop Control

To control the output torque of the HUCA, the clutch must be *slipping*. Then the output torque of the HUCA can be derived from Eq. :

$$t_{huca} = -I'_{cl2}\Delta\dot{\omega}'_{cl} - \text{sgn}(\Delta\omega'_{cl})t'_{lim} \quad (7.10)$$

where I'_{cl2} is the brake output inertia reflected on the HUCA output and t'_{lim} is the limiting friction of the brake reflected on the output.

There are different ways to set the ω'_{usm} to obtain the t'_{huca} in the desired direction. In the HUCA force control, it has been set in order to have the clutch slipping $\Delta\omega'_{cl}$ proportional to t_{set} :

$$\omega_{set}(k+1) = \begin{cases} \omega_{huca}(k) + K_v t_{set}(k) & \text{if } |K_v t_{set}(k)| < \omega_{lim} \\ \omega_{huca}(k) + \text{sgn}(t_{set}(k))\omega_{lim} & \text{if } |K_v t_{set}(k)| \geq \omega_{lim} \end{cases} \quad (7.11)$$

where ω_{set} is the desired ω'_{usm} value, K_v is the torque velocity gain, and ω_{lim} is the maximum slipping, its value is 3 rad/s .

- For a t_{set} null, ω'_{usm} is equal to the output velocity ω_{huca} canceling the clutch slipping Δ_{cl} . This reduces the effect of the drag torque and dynamic torque of the brake by limiting the brake motion.
- The slipping of the clutch $\Delta\omega'_{cl}$ proportional to t_{set} ensures a smooth torque direction change.
- For high torques, the instability due to the stick-and-slip are avoided by the increasing of the slipping of the brake
- For very high t_{set} , the slipping is limited to ω_{lim} to avoid an excessive motor velocity and to limit force ripples on the output due to the differential.

In open-loop, t'_{lim} is set equal to the absolute value of t_{set} :

$$t'_{lim} = |t_{set}| \quad (7.12)$$

7.3.3 Closed-Loop Control

In closed-loop, a proportional feedback on the torque error measured with the torque sensor can be added. Since the displayable torque cannot be opposed to the velocity, a condition must be added to prevent setting t'_{lim} to a value opposed to t_{set} .

$$t'_{lim}(k) == \begin{cases} |t_{set}(k) + K_f(t_{set}(k) - t'_{sens}(k))| & \text{if } \frac{K_f(t'_{sens}(k) - t_{set}(k))}{t_{set}(k)} > -1 \\ 0 & \text{otherwise} \end{cases} \quad (7.13)$$

A closed-loop torque control has been implemented with a proportional gain K_f equal to 1. Higher K_f can not be used as it creates instabilities, even with a filtering of the signal t'_{sens} and a derivative term in the control. These instabilities can come from the stick-and-slip effect and the play in the differential. The final, closed-loop torque control is illustrated in Fig. 7.9.

7.3.4 Performances

The performances of the closed-loop torque control have been evaluated with the output of the HUCA locked. Its static characteristic is obtained by imposing a torque ramp, Fig. 7.10(a) shows the HUCA torque response. Despite some small oscillations, the HUCA is able to follow the set torque t_{set} . For low torques a drag torque can be observed. This drag torque is also visible in the torque step response of the HUCA (Fig. 7.10(b)). The drag torque has been estimated of 0.005 Nm. This is due to a remanence effect that prevents the limiting torque to drop to its lowest value while the clutch is locked. With the free output, drag torque of 0.001 has been estimated in the transparency subsection 7.5.1.

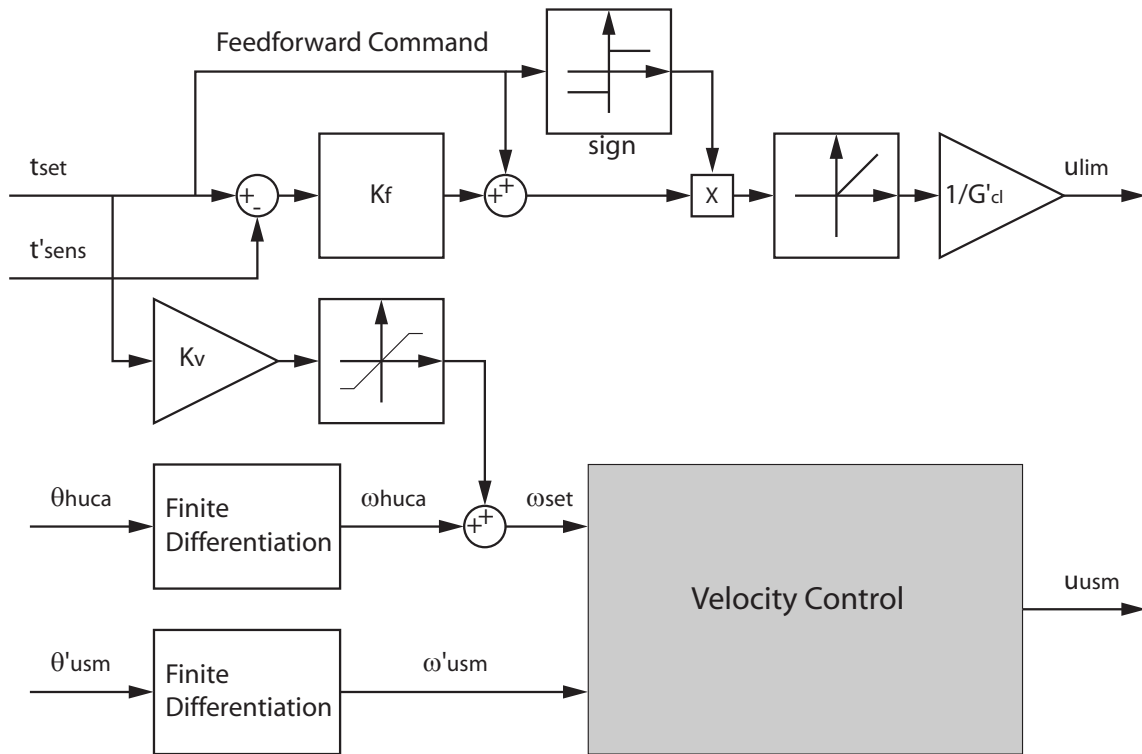


Figure 7.9: The torque control scheme includes a closed-loop on the transmitted torque t'_{lim} and on the control of the USM velocity ω'_{usm} to display the output force in the correct direction.

In the step response, the rise time of the output torque is equal to 53 ms while the fall time is 27 ms , these values are similar to the ones of the velocity control.

The effect of the drag torque is less visible with a set torque with a sinusoidal shape. Fig. 7.11(a) shows the HUCA torque response to a sine signal in open-loop, while Fig. 7.11(b) shows the closed-loop torque response to the same torque command. The response in closed-loop has been improved by reevaluating the static gain of the clutch G'_{cl} and by the use of a proportional control.

Because the output torque of HUCA depends on the velocity control, its bandwidth in force control should be at most in the same range. Fig. 7.12 shows the bode plot of the output force of the HUCA in closed-loop. The bandwidth of the HUCA torque control in closed-loop is 10 Hz for command signal with and without offset. This is slightly better than the HUCA velocity control bandwidth, since the HUCA output is locked, only a small USM motion is required to output a torque with the HUCA.

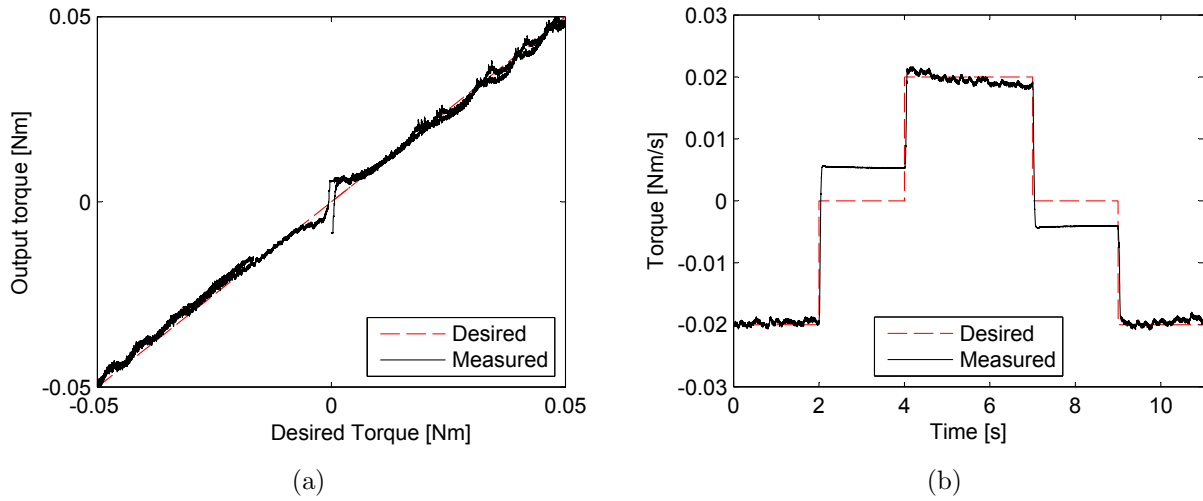


Figure 7.10: (a) Static response of the HUCA output torque controlled in closed-loop. (b) Step response of the HUCA output torque controlled in closed-loop. In both responses, the HUCA shows a drag torque of $\sim 0.005 \text{ Nm}$

7.3.5 Conclusion

As expected, the ER brake doesn't show a noticeable viscosity and its limiting friction can be controlled with u_{lim} . However, the static friction increases faster than the dynamic friction, creating stick-and-slip instabilities for high torques. Closed-loop torque control can be performed with the HUCA. The bandwidth of the HUCA in torque control is similar to the HUCA in velocity, as in this system the torque is dependent of the velocity. Higher bandwidth can be reached, if the motor rotates at constant velocity [Furusho 99].

7.4 Indirect force control

The indirect force control is based on the principle that the haptic interface can behave like a second order mechanical system [Moix 05]:

$$t_{user} = I\dot{\omega} + D\omega + K\theta \quad (7.14)$$

where t_{user} is the torque applied to the virtual system. Because the t_{huca} , t_{set} and t'_{sens} are defined as the torque applied by the interface to its environment, t_{user} is opposed to these torques.

I , D and K are respectively the inertia, the viscous damping and the stiffness to be rendered. ω and θ are the velocity and the position of the interface output.

There are two possibilities to control the interface in function of this equation:

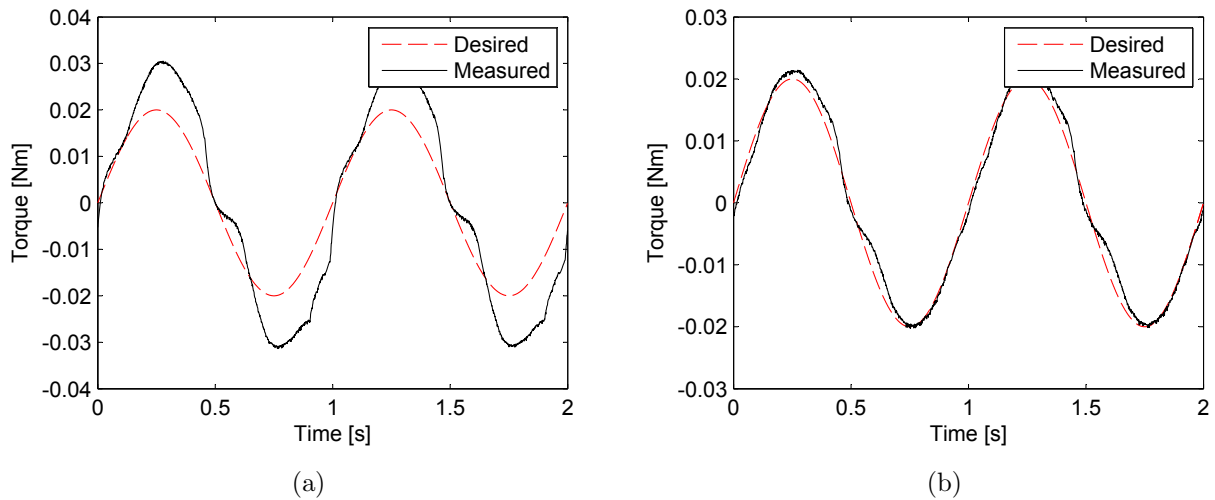


Figure 7.11: (a) Torque response of the HUCA in open-loop to a sine command. The static gain is too high and the curve is deformed for low torques. (b) Torque response of the HUCA in closed-loop to a sine command. With a smaller static gain, the torque is in the same range as the desired torque. The proportional gain smooths the torque curve at low torques.

- In *impedance control*, by measuring the position (and velocity) and by setting a torque.
- In *admittance control*, by measuring the torque applied to the system and by setting a velocity (or position).

In this section, the capacity of the HUCA in these two control schemes will be investigated.

7.4.1 Impedance control

In the impedance control scheme, the torque is set in function of the desired impedance and the measured position [Hogan 85].

This control scheme requires a low output impedance interface:

- because only the output position is measured, the friction force and the dynamic force of the system is not taking into account by the control.
- the impedance control increases the felt impedance of the interface. To have a large displayable range, the impedance of the interface must be initially low.

Thanks to its low impedance in the *slipping mode*, the HUCA can be controlled in impedance. The limitations of this control are:

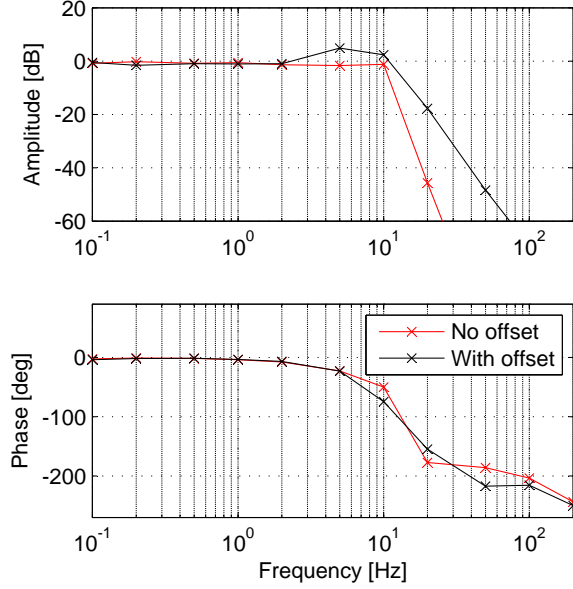


Figure 7.12: Bode plot of the torque response of the HUCA in closed-loop. The bandwidth for commands signal with and without offset is about 10 Hz.

- the display of high impedance is limited by the control effort that tends to destabilize the system.
- while displaying large impedance, the motion of the interface can make violent movements due to the application of high torques to the low impedance output.

Applied to the HUCA, t_{set} can be expressed with Eq. 7.14:

$$t_{set}(k+1) = -I\dot{\omega}_{huca}(k) - D\omega(k)_{huca} - K\theta_{huca}(k) \quad (7.15)$$

where $\dot{\omega}_{huca}$ is the angular acceleration of the HUCA output. It is estimated by applying two times the filtered finite differentiation of Eq. 7.4. The output torque is set with the open-loop torque control described in the subsection 7.3.2, the closed-loop control is not as it creates instabilities.

The HUCA controlled in impedance are evaluated by setting different values of I , D and K . They are evaluated separately. While one is evaluated, the two other are set to zero. For positive values, there is no lower limit for I and D . However the impedance felt by the user is the sum of the HUCA output impedance and the set impedance, then the lowest displayable impedance is the HUCA output impedance ($I_{huca} = 7.6 \cdot 10^{-6} \text{ kgm}^2$ and $D_{huca} = 0.26 \cdot 10^{-3} \text{ Nms/rad}$). The minimum value of K is the value below which, the spring force is too small to move the output of the HUCA back. The maximum displayable

impedance is limited by system stability. Table 7.2 summarizes the range of displayable values. The maximum displayable inertia is high as it is three orders more than the HUCA inertia. Compared to the conventional electrical motors, the HUCA output velocity is dynamically bounded by ω_{set} , and its clutch is a damper that dissipates power. These two factors improve the system stability.

Table 7.2: Stable Set Impedance Range for the HUCA in Impedance Control.

	Minimum	Maximum
Inertia I $[kgm^2]$	0	$5 \cdot 10^{-3}$
Viscous damper D $[Nms/rad]$	0	0.1
Stiffness K $[Nm/rad]$	0.01	1

Controlled free Movements

The bounded velocity is an interesting property of the HUCA, this subsection explains how it can be exploited.

The impedance control uses the open-loop torque control of subsection 7.3.2. The value set to the USM in the linear range is:

$$\omega_{set}(k+1) = \omega_{huca}(k) + K_v t_{set}(k) \quad (7.16)$$

If its output is released, the clutch will automatically switch from the *slipping mode* to the *locked mode*, and its output velocity $\omega_{huca}(k+1)$ will tends to $\omega_{set}(k+1)$. Then the maximum acceleration of the system depends of $\omega_{set}(k+1)$ and can be estimated by finite differentiation:

$$\frac{\Delta_{max}\omega_{huca}(k+1)}{T_s} = \frac{1}{T_s} (\omega_{set}(k+1) - \omega_{huca}(k)) = \frac{K_v}{T_s} t_{set}(k) \quad (7.17)$$

where $\Delta_{max}\omega_{huca}(k+1)$ is the maximum difference of velocity of the output at the next sample. The maximum acceleration of the system is proportional to $t_{set}(k+1)$ and the ratio $\frac{T_s}{K_v}$ can be assimilated to an inertia equal to $2 \cdot 10^{-5}$ with the control parameters.

The torque control of the subsection 7.3.2 takes profit of the bounded velocity property of the HUCA. By a smart setting of the USM velocity, it allows to control in the same time:

- the output torque if the user is interacting with the interface.
- the maximum acceleration of the system if the system is released.

This can explain the high impedance achieved in impedance control, the accelerations of the HUCA are limited by the inertia $\frac{T_s}{K_v}$ that is higher than I_{huca} .

In impedance control, the apparent inertia of the system $\frac{T_s}{K_v}$ can be adjusted so that the motion of the system unconstrained and the output force of the system interacting with the user corresponds to the same second order mechanical model. This can be done by setting:

$$K_v = \frac{T_s}{I} \quad (7.18)$$

In practice, the K_v obtained with this method is too small, the difference of velocity between the USM and the HUCA output is not large enough to overcome the system imperfections: the play in the differential and the velocity control errors.

7.4.2 Admittance control

In the admittance control scheme, the motion of the output is set in function of the desired impedance and the measured torque on the output [Newman 92].

$$I\dot{\omega}_{huca} = -D\omega_{huca} + \theta_{huca}K - t'_{sens} \quad (7.19)$$

To control the position of the output, the clutch is locked and the closed-loop velocity control of subsection 7.2.2 is used. Because there is some play and friction on the differential, the velocity achieved with the USM ω'_{usm} is not exactly equal to ω_{set} . The admittance control is performed directly on ω_{set} :

$$-t'_{sens}(k) = \frac{I}{T_s}(\omega_{set}(k+1) - \omega_{set}(k)) + D\omega_{set}(k+1) + KT_s \sum_n^{k+1} \omega_{set}(n) \quad (7.20)$$

The admittance control will be expressed with the USM velocity. Since feedback is only applied on the velocity, drift of the spring position may happen with this controller.

With Eq. 7.20, it is then possible to determine the velocity $\omega_{set}(k+1)$ to set to the USM. Like for impedance, the ranges of displayable inertia I and damping D have been determined separately. In both case, the minimum value is determined by instabilities appearing during movement direction changes. Their maximum values are the values for which a motion can still be obtained, the motor is locked for higher I or D .

The evaluation of the range of the stiffness K cannot be done without a term I or D to limit the dynamics and the velocity of the output. Different value of K have been tested with a $D = 0.01 \text{ Nms/rad}$. Because the HUCA is stable with this D , there is no minimum unstable K . The HUCA output is locked above the maximum value of K .

7.4.3 Conclusion

The HUCA shows good performances in impedance control. Since the clutch dissipates the excess of power and since its output accelerations is limited even when the HUCA is released, the stability of the system is improved. With the limited acceleration, an apparent inertia

Table 7.3: Stable Impedance Range for the HUCA in Admittance Control.

	Minimum	Maximum
Inertia I [kgm ²]	$0.5 \cdot 10^{-3}$	0.5
Viscous damper D [Nms/rad]	0.01	1
Stiffness K [Nm/rad]	0 ^a	1 ^a

^aObtained with a $D = 0.01$ Nms/rad.

can be set to the system when its output is moving freely. The performances of the HUCA in admittance control are lower as they are affected by the performances of the velocity control of the USM and the mechanical play of the differential. The range of impedance achieved is higher than the one in impedance control.

The possibility to control the HUCA in impedance and admittance allows the HUCA to display a wide range of impedances. The overlap of the impedance ranges of the two control schemes suggests that a smooth transition between the impedance control and the admittance control is possible.

7.5 Transparency and Walls

When zero force is set in torque control or in impedance control, the HUCA is in an active transparency mode. It is then necessary to evaluate the active transparency properties and to compare them to the initial HUCA output values. The haptic wall effect will be implemented and evaluated with the active and passive transparency.

7.5.1 Transparency

The HUCA can render the transparency passively thanks to its back-drivability. However, the transparency of the HUCA can be actively improved by limiting the motion of the clutch to reduce the effect of the drag torque. This is done by setting ω_{set} and t'_{lim} :

$$\begin{cases} \omega_{set}(k+1) = \omega_{huca}(k) \\ t'_{lim} = 0 \end{cases} \quad (7.21)$$

The active transparency conditions can be obtained by setting $t_{set} = 0$ in the force control of the HUCA. Fig. 7.13(a) shows the measured remaining torque while the HUCA is used in passive transparency, Fig.7.13(b) shows the same with the active transparency. The damping and the drag torque have been estimated from these figures and reported in Table 7.4. Because of the play and nonlinearity at the end of the motion, the estimation has been done for output positions between ± 0.6 rad. The output inertia cannot be estimated as the parts of the curves with the higher acceleration are affected by the play of the differential. The active transparency reduces efficiently the drag torque and the damping. However torque peaks up

Table 7.4: Transparency of the HUCA

		Passive	Active
Damping	[Nm/s]	$0.11 \cdot 10^{-3}$	$-0.01 \cdot 10^{-3}$
Friction	[Nm]	$1 \cdot 10^{-3}$	$0.16 \cdot 10^{-3}$

to 0.004 Nm appear, when the motion direction changes due to the delay in the velocity control of the USM.

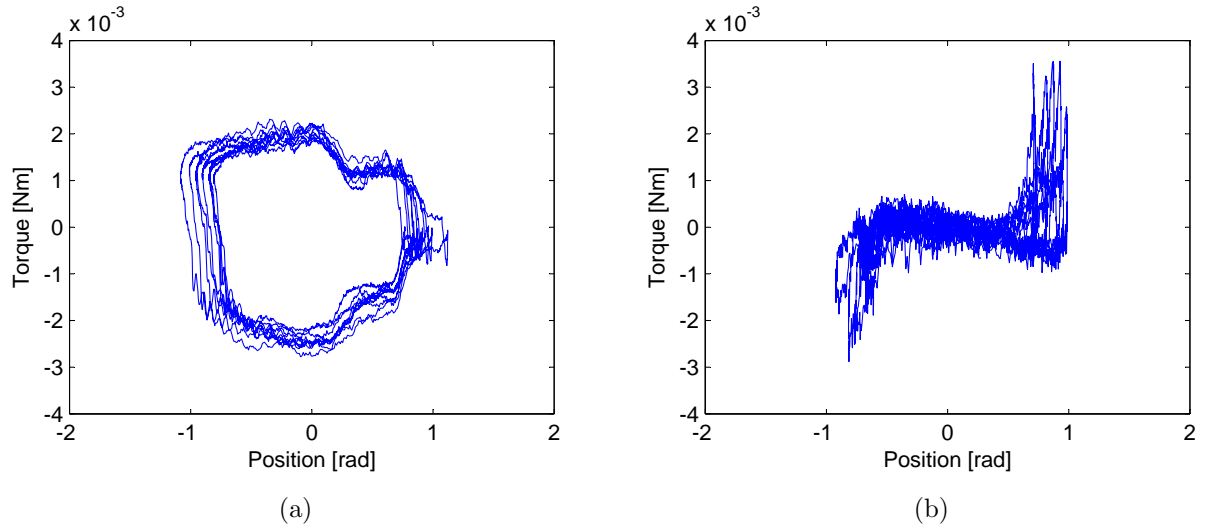


Figure 7.13: (a) Measured output torque in function of the output position with the HUCA in passive transparency. (b) Measured output torque in function of the output position with the HUCA in active transparency.

7.5.2 Wall

The wall haptic effect consists in rendering transparency and a contact with a stiff wall at a given position. This effect is very difficult to render due to the opposite nature of the transparency where a null force is imposed and the wall where the position is imposed and is considered as a benchmark problem [Colgate 93]. This effect can be rendered in conjunction with the passive or active transparency. When the wall is reached, the USM must be stopped and the clutch must be locked.

$$\begin{cases} \omega_{set}(k+1) = 0, & u_{lim}(k+1) = u_{lim_{max}} & \text{if } \theta_{huca} > \theta_{wall} \text{ and } (\omega_{huca} > 0 \text{ or } t_{sens} < 0) \\ \text{transparency} & & \text{otherwise} \end{cases} \quad (7.22)$$

where θ_{wall} is the position of the wall. Angles above this value are considered inside the wall. Two additional conditions have been added to detect if the motion of the knob is entering inside the wall or if a torque is applied on it. These conditions allow the releasing of the clutch when the knob leaves the wall, avoiding the feeling of a sticky wall.

Walls implemented with the passive transparency are illustrated in Fig. 7.14(a), and other using the active transparency in Fig. 7.14(b). The passive walls show a higher drag torque, but the displayed torque is smoother and the walls rendered are stiffer than the active one:

$$\begin{cases} K_{wall_{passive}} = 2.7 \text{ Nm/rad} \\ K_{wall_{active}} = 0.7 \text{ Nm/rad} \end{cases} \quad (7.23)$$

where $K_{wall_{passive}}$ and $K_{wall_{active}}$ are the measured stiffness of the walls. $K_{wall_{passive}}$ corresponds to the HUCA output stiffness. The walls with the active transparency appear softer due to a larger travel of the output into the wall: $\Delta\theta = 0.011 \text{ rad}$ for the passive and $\Delta\theta = 0.036 \text{ rad}$ for the active. This difference of travel can be explained by the time required by the USM to stop.

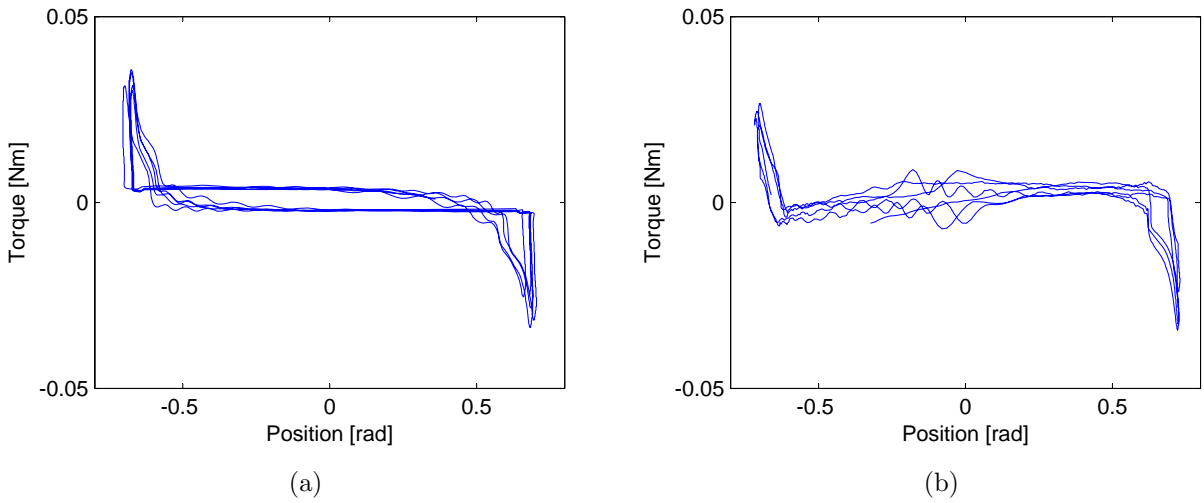


Figure 7.14: (a) Measured output torque in function of the output position when the HUCA is displaying walls using the passive transparency. (b) Measured output torque in function of the output position for walls using the active transparency.

7.5.3 Conclusion

Thanks to its back-drivability, the HUCA can display passively transparency. In this mode, the drag torque of the clutch is predominant. With the active transparency, this drag torque

is significantly reduced, but force peaks can appear for fast velocity changes on the output, it is then more adapted for smooth motion. The wall effect can be added to the transparency. The wall implemented with the passive transparency show stiffer wall, than with the active transparency.

7.6 Comparison with the Hydrostatic Transmission Interfaces

The HUCA has been developed as an alternative to hydrostatic transmission interfaces that are used in the *LSRO*. From the different interfaces developed at the *LSRO*, the finger interface [Honold 06] has the most similar force range as the HUCA. The finger interface has been designed to interact with the motion of the thumb and the index during the pinching movements. Fig. 7.15 shows the different parts constituting the slave part of the finger interface.

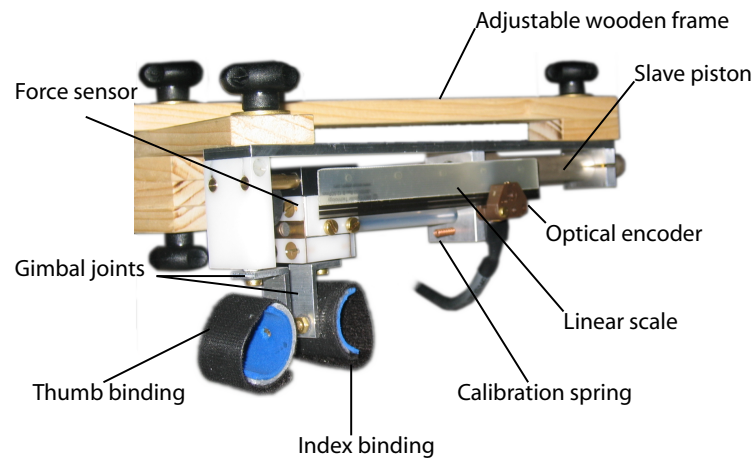


Figure 7.15: Finger interface developed in the project [Bleuler 03] to investigate finger movements.

7.6.1 Specifications

Based on pistons, the hydrostatic transmissions are translational mechanisms while the HUCA is a rotating one. To allow comparison, the values of one of these interfaces must be transposed in the physical values of the other. Since the focus of this thesis is the HUCA, the finger interface values will be reported. The interaction is done mainly in terms of force. The conversion factor is taken as the ratio that transforms the maximum output force of the finger interface $f_{fint_{max}}$ into the maximum output torque of the HUCA $t_{huca_{max}}$, this corresponds to

the gear ratio r_{conv} :

$$r_{conv} = \frac{t_{huca_{max}}}{f_{fint_{max}}} = \frac{0.05 Nm}{25 N} = 2 \cdot 10^{-3} m \quad (7.24)$$

The different values of the specifications of the two interfaces have been summarized in Table 7.5. Even the two interfaces have been designed to interact with fingers, the motor used in the finger interface is much more powerful. This difference is due to the fact that proportionally the output force/torque of the HUCA is smaller and that the main part of the motor power is used to move the hydrostatic transmission in the finger interface. This hydrostatic transmission constitutes a high impedance and has a very high friction on the output. This difference explains why the finger interface must be controlled in admittance, while the HUCA is better controlled in impedance.

Table 7.5: Comparison of the specifications of the finger interface vs. the HUCA

	Finger interface		HUCA
	Initial	Reported	
Actuator nominal power		150 W	1 W
Maximum output torque	25 N	$50 \cdot 10^{-3} Nm$	$50 \cdot 10^{-3} Nm$
Inertia	6.4 kg	$2.6 \cdot 10^{-5} kgm^2$	$7.6 \cdot 10^{-6} kgm^2$
Damping	834 Ns/m	$3.3 \cdot 10^{-3} Nms/rad$	$0.26 \cdot 10^{-3} Nms/rad$
Drag torque	28 N	$55 \cdot 10^{-3} Nm$	$1 \cdot 10^{-3} Nm$

7.6.2 Performances

The finger interface has specifications less favorable than the HUCA, however they are highly improved by control. In the Table 7.6, the bandwidths achieved in closed-loop force and velocity controls are reported. There are also the remaining output impedance and friction that have been estimated using the active transparency effect. The bandwidth of the HUCA is higher than the finger interface. In the finger interface, the bandwidth is limited by the propagation time of the movement in the hydrostatic transmission. In the HUCA, it is limited by the resolution of the encoders and the required time to change the rotation direction, then the HUCA bandwidth can still be improved. The performances in transparency of the finger interface are very good as it can reduce the remaining inertia and damping to values lower than the not powered HUCA. On the other hand, the HUCA in active transparency can reduce its output damping about 20 times and its drag torque almost by 2 and keeps the advantage on the finger interface. The remaining inertia of the HUCA could not be properly estimated due to the play in the HUCA mechanism and the torque peaks appearing in the

movement direction changes. The finger interface has the advantage not to suffer from any play.

Table 7.6: Comparisons of the performances of the finger interface vs. the HUCA

	Finger interface		HUCA
	Initial	Reported	
Torque bandwidth		2.5 Hz	10 Hz
Velocity bandwidth		3.5 Hz	10 Hz
Remaining inertia	0.4 kg	$1.6 \cdot 10^{-6} \text{ kgm}^2$	not estimated
Remaining damping	12.5 Ns/m	$0.05 \cdot 10^{-3} \text{ Nms/rad}$	$-0.01 \cdot 10^{-3} \text{ Nms/rad}$
Remaining drag torque	0.20 N	$0.4 \cdot 10^{-3} \text{ Nm}$	$0.16 \cdot 10^{-3} \text{ Nm}$

7.7 Conclusion

Four control schemes (Table 7.7) have been implemented on the HUCA. Its performances in the direct velocity and torque control modes have been evaluated. With the velocity and torque control, impedance and admittance control have been implemented and their ranges of displayable mechanical impedances have been determined. The range in impedance is lower and partially overlaps the admittance range. The possibility to control the HUCA in impedance and admittance allows to display a large range of impedances. The impedance control shows better performances than the admittance control and its stability is improved by a velocity that can be bounded dynamically and the clutch acting as a damper. The HUCA has the property of controlling its dynamics in impedance control even when its output is released. When zero torque is set in direct torque control or in impedance control, the system is in an active transparency mode compensating the friction and the inertia of the clutch. This mode is efficient except during the motion directions change, due to the time required to change the USM rotation direction. The haptic wall effect has been added to the passive and active transparency. Even if the friction is higher in the passive transparency, the walls displayed are stiffer. The HUCA has been compared to a hydrostatic transmission designed to interact with the finger. The HUCA has better specifications, better performances in active transparency and a higher bandwidth in force and velocity control than the hydrostatic transmission.

Table 7.7: Control schemes implemented on the HUCA

USM velocity control
$u_{usm}(k) = \frac{1}{G'_{usm}}(\omega_{set}(k) + K_p(\omega_{set}(k) - \omega'_{usm}(k)))$
HUCA force control
$\omega_{set}(k) = K_v t_{set}(k)$ $t'_{lim} = t_{set}(k) + K_f(t'_{sens}(k) - t_{set}(k)) $
HUCA interaction controllers
Impedance control $t_{set}(k+1) = -I\dot{\omega}_{huca}(k) - D\omega_{huca}(k) - K\theta_{huca}(k)$
Admittance control $-t'_{sens}(k) = \frac{I}{T_s}(\omega_{set}(k+1) - \omega_{set}(k)) + D\omega_{set}(k+1) + KT_s \sum_n^{k+1} \omega_{set}(n)$

Chapter 8

Conclusion

MR-compatible haptic interfaces are powerful tools for neuroscience study, diagnostic and rehabilitation. The interactions with fingers require miniaturized devices. This size reduction poses issues on the actuation methods: the remote actuation methods lose their efficiency, while the other MR-compatible actuators are not able to display arbitrary forces. This chapter summarizes and discusses the different contributions developed in this work to address this problem. Then future developments are suggested for the novel actuator created in this thesis: the Hybrid Ultrasonic motor Clutch Actuator (HUCA).

8.1 Contributions of this Thesis

The goal of this work was to develop an improved actuation method for haptics in MR environments. From an evaluation of the different MR-compatible actuation principles available, the Ultrasonic Motor (USM) showed the largest potential. However the USM output torque cannot be well controlled, resulting in a reduced quality of the force-feedback and constituting a hazard for the user. By considering the USM as a velocity source, different mechanical solutions have been investigated to control the system output force and then its output power. The performances achieved by the prototype validated the proposed concept.

A Mechatronic Approach

This thesis proposed an original approach to the USM output force control issues, by analyzing the mechanical aspects of the haptic interface with the force/voltage electrical analogy.

The USM high output impedance has been identified as the cause of its output force sensitivity to motion perturbations. The USM is then considered as a velocity source on which components may be added to control the output force in order to improve the system force-feedback performances and the user safety.

The first suggested solution is to filter the dynamics of the USM by adding in series low impedance passive components. This solution called *series dynamics* has been developed

initially to decrease the output impedance of a geared motor by the mean of a spring (Series Elastic Actuator) or a damper (Series Damper Actuator).

Criteria for the choice of the added spring and the added damper were determined by analyzing the specificities of the USM. Investigations of the SEA and SDA showed that the decrease of the output impedance is made in detriment of the forward transfer function, resulting in a loss of bandwidth for the SEA and a loss of gain for the SDA.

A Novel Actuator

Extending the electrical analogy, a force regulator can be used to control the output force of the system. This was achieved by adding in series a force-controlled clutch to the USM: the Hybrid Ultrasonic motor Clutch Actuator (HUCA).

The HUCA can behave like a velocity source or a force source depending on the state of the clutch. It does not suffer from the performance tradeoffs that are typical for the series dynamics actuators. With the HUCA, the safety of the user is improved, as both the output force and velocity are dynamically limited.

The brake-differential system, consisting of a brake connected through a differential, was proposed to replace the clutch. Compared to a conventional clutch, this mechanism limits the moving inertia and the rotating electrical connections, as the base of each actuator is fixed.

In order to validate the HUCA concept and the differential-brake system, a non-MR-compatible prototype of the HUCA has been realized with standard components. This prototype allowed to perform the preliminary control experiments. It showed that the HUCA concept can address the USM force control performance and safety issues for applications out of MR environments.

A MR-compatible prototype based on an ER-brake was realized. A torque sensor and hollow shaft brake were developed to allow a HUCA compact design. The MR-compatibility of this prototype was successfully tested and showed better haptic performances than the previous MR-compatible actuators. This prototype validates the concept of the HUCA for MR-environments.

Control of the HUCA

The hybrid nature of the HUCA requires the development of dedicated control schemes to achieve high-fidelity haptic rendering.

Its two different power source behaviors can be used in different control schemes: velocity and admittance control with the velocity source, and force and impedance control with the force source. The HUCA is able to render a wide range of impedance thanks to the overlap of the ranges of displayable impedance, using either impedance or admittance control.

The proposed force control scheme lets the clutch slip proportionally to the output force. This allows an active compensation of both the friction and the inertia of the brake when a

null force is set, and to control the dynamics of the output when it is released by the user, thus improving the stability of the HUCA in direct force control and impedance control.

A method to render hard walls with the HUCA has been implemented. Experiments show that the walls are stiffer without active friction and inertia compensation during free movement, as the dynamics of the USM decrease the wall stiffness.

Progress in MR-compatible Actuations

The hypothesis made in this work to exclude remote actuation methods constitutes an important break in the technology conventionally used in the LSRO. This hypothesis was validated by comparing the safety and the performances of the MR-compatible prototype to those of a hydrostatic transmission interface developed to interact with the fingers: the HUCA exhibits better performances and user safety.

An additional advantage of the power transmission through electrical wires is the compactness of the entire system making its use easier. The HUCA will allow to actuate more easily multiDOF interfaces. Thanks to its described qualities, the HUCA constitutes an important progress in the actuation of the haptic interfaces in an MR environment.

8.2 Outlook

Future developments of the HUCA may be undertaken in four directions as described below.

fMRI Studies

Though the performances and compatibility have been demonstrated, the MR-compatible HUCA prototype has not been used in an fMRI study yet. Thanks to the small force and low impedance achieved, it may be used in such an environment to study motor tasks requiring e.g. fine finger motion.

MultiDOF Interfaces

The compactness reached with the HUCA allows the development of MR-compatible multi-DOF haptic interfaces such as joysticks, pantographs or Delta robots. They will extend the interactions possibilities far above the current devices.

Advanced Control

Because in the HUCA both the limiting force and velocity can be controlled in parallel, a large variety of control schemes and haptic effects could be implemented to exploit these properties:

- In impedance control mode, the acceleration of the output is controlled when it is released. The HUCA should be able to render the same second order model in free motion as in constrained motion using an impedance control scheme.
- As the displayable range of displayable in impedance and admittance control are complementary, switching from one control scheme to the other will allow using the full range of the HUCA in a robust manner. Criteria must be defined for the switching and a smooth transition must be elaborated and implemented.
- The extension of these control schemes to an interface with several DOF can be studied.

Alternative Applications

The properties of the HUCA are unique also outside the MR-compatible robotics. Due to the severity of the constraints, MR-compatible components have in general lower mechanical properties than standard components. The performance limits of the HUCA integrating high-performances conventional components should be investigated.

Thanks to the large displayable impedance, the HUCA is an ideal actuator for human-machine interaction, including force-feedback simulators and teleoperation systems.

Bibliography

- [Adams 02] RJ Adams & B Hannaford. *Control law design for haptic interfaces to virtual reality*. Control Systems Technology, IEEE Transactions on, vol. 10, no. 1, pages 3–13, Jan 2002. 10
- [Aovagi 04] M Aovagi, T Tomikawa & T Takano. *A novel ultrasonic motor with a built-in clutch mechanism for a force-feed-back actuator*. In IEEE Ultrasonics Symposium, volume 3, pages 2239–2242 Vol.3, Aug. 2004. 56
- [Bar-Cohen 04] Y Bar-Cohen, editeur. *Electroactive polymer (eap) actuators as artificial muscles: Reality, potential, and challenges, second edition*. SPIE Press Book, March 2004. 19, 20
- [Barth 73] H V Barth. *Ultrasonic driven motor*. IBM Technical Disclosure Bulletin, vol. 16, page 2263, 1973. 23
- [Bennett 96] LH Bennett, PS Wang & Donahue MJ. *Artifacts in magnetic resonance imaging from metals*. The 40th annual conference on magnetism and magnetic materials, vol. 79, no. 8, pages 4712–4714, 1996. 15
- [Bleuler 03] H Bleuler, R Gassert, EW Radü, S Haller & E Burdet. *An fMRI compatible haptic interface to investigate brain mechanisms of manipulation*, September 2003. FNS-205321-104292/1. 2, 3, 127
- [Bullo 02] M Bullo & Y Perriard. *Performance Analysis and Optimization of the Travelling Wave Ultrasonic Motor*. vol. 3, pages 1907–1913, October 2002. 110
- [Chapuis 04] D Chapuis, R Gassert, L Sache, E Burdet & H Bleuler. *Design of a Simple MRI/fMRI Compatible Force/Torque Sensor*. In Proc. IEEE/RSJ International Conference on Intelligent Robots and Systems (IROS), volume 3, pages 2593–2599, 2004. 79, 95

- [Chapuis 06] D Chapuis, R Gassert, E Burdet & H Bleuler. *Hybrid Ultrasonic Motor and Electrorheological Clutch System for MR-Compatible Haptic Rendering*. In Proc. IEEE/RSJ International Conference on Intelligent Robots and Systems (IROS), 2006. 74, 83, 99, 103
- [Chapuis 07] D Chapuis, X Michel, R Gassert, C-M Chew, E Burdet & H Bleuler. *A Haptic Knob with a Hybrid Ultrasonic Motor and Powder Clutch Actuator*. pages 200–205, March 2007. 87
- [Chapuis 08] Dominique Chapuis, Roger Gassert, Etienne Burdet & Hannes Bleuler. *A hybrid ultrasonic motor and electrorheological fluid clutch actuator for force-feedback in MRI/fMRI*. In Engineering in Medicine and Biology Society, 2008. EMBS 2008. 30th Annual International Conference of the IEEE, pages 3438–3442, Aug. 2008. 87, 99
- [Chew 04] CM Chew, GS Hong & W Zhou. *Series damper actuator: a novel force/torque control actuator*. volume 2, pages 533–546, Nov. 2004. 51, 69, 70
- [Chinzei 99] K Chinzei, R Kikinis & A Jolesz. *MR Compatibility of Mechatronic Devices: Design Criteria*. Proc. Second International Conference on Medical Image Computing and Computer-assisted Interventions (MICCAI), pages 1020–1030, September 1999. 13
- [Chinzei 00] K Chinzei, N Hata, F Jolesz & R Kikinis. *Surgical Assist Robot for the Active Navigation in the Intraoperative MRI: Hardware Design Issues*. In Proc. IEEE/RSJ International Conference on Intelligent Robots and Systems (IROS), pages 727–732, 2000. 1, 18
- [Choi 99] B.H. Choi & H.R. Choi. *A semi-direct drive hand exoskeleton using ultrasonic motor*. pages 285–290, 1999. 42
- [Choi 00] B H Choi & H R Choi. *SKK Hand Master-hand exoskeleton driven by ultrasonic motors*. volume 2, pages 1131–1136, 2000. 31, 97
- [Colgate 93] JE Colgate, PE Grafing, MC Stanley & G Schenkel. *Implementation of Stiff Virtual Walls in Force-Reflecting Interfaces*. In Proceedings, IEEE-VRAIS, Seattle WA, 1993. 125
- [Del Pedro 97] M Del Pedro & P Pahud. *Mécanique vibratoire*. Presses Polytechniques et Universitaires Romandes, 1997. 49

- [DiMaio 06] SP DiMaio, GS Fischer, SJ Haker, N Hata, I Iordachita, CM Tempany, R Kikinis & G Fichtinger. *A System for MRI-guided Prostate Interventions*. In Proc. first IEEE / RAS-EMBS International Conference on Biomedical Robotics and Biomechatronics (BioRob), 2006. 1
- [DiMaio 07] S. P. DiMaio, S. Pieper, K. Chinzei, N. Hata, S. J. Haker, D. F. Kacher, G. Fichtinger, C. M. Tempany & R. Kikinis. *Robot-assisted needle placement in open MRI: system architecture, integration and validation*. *Comput Aided Surg*, vol. 12, no. 1, pages 15–24, 2007. 18
- [Elhawary ss] H Elhawary, A Zivanovic, M Rea, B Davies, C Besant, DW McRobbie, N de Souza, I Young & M Lampérth. *A Modular Approach to MRI Compatible Robotics: Interconnectable One DOF Stages*. *IEEE Engineering in Medicine and Biology Magazine*, in press. 78
- [Flueckiger 05] M Flueckiger, M Bullo, D Chapuis, R Gassert & Y Perriard. *fMRI Compatible Haptic Interface Actuated with Traveling Wave Ultrasonic Motor*. *Proc. IEEE Industry Applications Society (IAS)*, vol. 3, pages 2075–2082, 2005. 18, 19, 30, 42
- [Food 97] Food & Drug Administration. *A Primer on Medical Device Interactions with Magnetic Resonance Imaging Systems*. U.S. Department of Health and Human Services, <http://www.fda.gov/cdrh/ode/primerf6.html>, 1997. 14
- [Furusho 99] J Furusho & M Sakaguchi. *New Actuators Using ER Fluid and Their Applications to Force Display Devices in Virtual Reality and Medical Treatments*. *International Journal of Modern Physics B*, vol. 13, no. 14/16, pages 2151– 2159, 1999. 119
- [Gassert 06a] R Gassert, L Dovat, O Lambercy, Y Ruffieux, D Chapuis, G Ganesh, E Burdet & H Bleuler. *A 2-DOF fMRI Compatible Haptic Interface to Interact with Arm Movements*. In Proc. IEEE International Conference on Robotics and Automation (ICRA), pages 3825–3831, 2006. 2, 3, 95
- [Gassert 06b] R Gassert, N Vanello, D Chapuis, V Hartwig, EP Scilingo, A Bicchi, L Landini, E Burdet & H Bleuler. *Active Mechatronic Interface for Haptic Perception Studies with Functional Magnetic Resonance Imaging: Compatibility and Design Criteria*. In Proc. IEEE International Conference on Robotics and Automation (ICRA), pages 3832–3837, 2006. 78

- [Gassert 06c] Roger Gassert. *MR-Compatible Robotics to Investigate Human Motor Control*. PhD thesis, Ecole Polytechnique Fédérale de Lausanne (EPFL), Lausanne, 2006. 2
- [Gassert 06d] Roger Gassert, Akio Yamamoto, Dominique Chapuis, Ludovic Dovat, Hannes Bleuler & Etienne Burdet. *Actuation Methods for Applications in MR Environments*. Concepts in Magnetic Resonance Part B: Magnetic Resonance Engineering, vol. 29B, no. 4, pages 191–209, October 2006. 2, 17
- [Gassert 08a] R Gassert, E Burdet & K Chinzei. *MRI-Compatible Robotics*. Engineering in Medicine and Biology Magazine, IEEE, vol. 27, no. 3, pages 12–14, May-June 2008. 14
- [Gassert 08b] R. Gassert, D. Chapuis, H. Bleuler & E. Burdet. *Sensors for Applications in Magnetic Resonance Environments*. Mechatronics, IEEE/ASME Transactions on, vol. 13, no. 3, pages 335–344, June 2008. 78, 95, 96
- [Giraud 04] F. Giraud, B. Semail & J.-T. Audren. *Analysis and phase control of a piezoelectric traveling-wave ultrasonic motor for haptic stick application*. Industry Applications, IEEE Transactions on, vol. 40, no. 6, pages 1541–1549, Nov.-Dec. 2004. 30
- [Gogola 99] M Gogola & M Goldfarb. *Design of a PZT-actuated proportional drum brake*. Mechatronics, IEEE/ASME Transactions on, vol. 4, no. 4, pages 409–416, Dec 1999. 97
- [Golaszewski 02] SM Golaszewski, F Zschiegner, CM Siedentopf, J Unterrainer, RA Sweeney, W Eisner, S Lechner-Steinleitner, FM Mottaghy & S Felber. *A new pneumatic vibrator for functional magnetic resonance imaging of the human sensorimotor cortex*. J Neurosci Lett, vol. 324, no. 2, pages 125–128, 2002. 2
- [Hagood 95] N W Hagood & A J McFarland. *Modeling of a piezoelectric rotary ultrasonic motor*. Ultrasonics, Ferroelectrics and Frequency Control, IEEE Transactions on, vol. 42, no. 2, pages 210–223, March 1995. 29
- [Hara 09] M Hara, G Matthey, A Yamamoto, D Chapuis, R Gassert, H Bleuler & T Higuchi. *Development of a 2-DOF Electrostatic Haptic Joystick for MRI/fMRI Applications*. In 2009 IEEE International Conference on Robotics and Automation, 2009. 18

- [Harrington 00] GS Harrington, CT Wright & JH Downs. *A new vibrotactile stimulator for functional MRI*. Hum Brain Mapp, vol. 10, no. 3, pages 140–145, 2000. 18
- [Hartwig 04] V Hartwig, N Vanello, R Gassert, D Chapuis, MF Santarelli, V Positano, E Ricciardi, P Pietrini, L Landini & A Bicchi. *A compatibility test for tactile displays designed for fMRI studies*. In Proc. EuroHaptics 2004, pages 456–458, June 2004. 18
- [Heeger 02] DJ Heeger & D Ress. *What does the fMRI tell us about neuronal activity?* Nature Reviews, vol. 3, pages 142–151, 2002. 12
- [Hidler 06] Joseph Hidler, Timea Hodics, Benjamin Xu, Bruce Dobkin & Leonardo G. Cohen. *MR compatible force sensing system for real-time monitoring of wrist moments during fMRI testing*. J Neurosci Methods, vol. 155, no. 2, pages 300–307, 2006. 79
- [Hogan 85] N Hogan. *Impedance control: An approach to manipulation*. ASME Journal of Dynamic Systems, Measurement and Control, vol. 107, no. 1, pages 1–24, 1985. 10, 120
- [Hogan 04] N Hogan & SP Buerger. Robotics and automation handbook, chapitre Impedance and Interaction Control, pages 19.1–19.24. NY: CRC Press, 2004. 10, 47
- [Honold 06] S Honold. *Implementation of neuroscience experiments for an fMRI compatible haptic finger interface*. Master’s thesis, Ecole Polytechnique Fédérale de Lausanne (EPFL), 2006. 3, 127
- [Hu 95] J. Hu, T. Yamazaki, K. Nakamura & S. Ueha. *Analyses of an Ultrasonic Motor Driving Fluid Directly*. Japanese Journal of Applied Physics, vol. 34, page 2702, May 1995. 26
- [Hu 97] J Hu, K Nakamura & S Ueha. *An analysis of a noncontact ultrasonic motor with an ultrasonically levitated rotor*. Ultrasonics, vol. 35, no. 6, pages 459–467, September 1997. 26
- [Izawa 06] J. Izawa, T. Shimizu, H. Gomi, S. Toyama & K. Ito. *MR compatible manipulandum with ultrasonic motor for fMRI studies*. pages 3850–3854, May 2006. 31, 42
- [Kaneko 95] M Kaneko, T Nishihara & T Tsuji. *Active control of self-locking characteristic of ultrasonic motor*. volume 3, pages 2928–2934 vol.3, 21–27 May 1995. 31

- [Kawato 03] M Kawato, T Kuroda, H Imamizu, E Nakano, S Miyauchi & T Yoshioka. *Internal forward models in the cerebellum: fMRI study Internal forward models in the cerebellum: fMRI study on grip force and load force coupling*. Progr. in Brain Research, vol. 142, pages 171–188, 2003. 79
- [Khanicheh 05] A Khanicheh, A Muto, C Triantafyllou, B Weinberg, L Astrakas, A Tzika & C Mavroidis. *MR Compatible ERF Driven Hand Rehabilitation Device*. Proc. IEEE 9th International Conference on Rehabilitation Robotics (ICORR), pages 7–12, 2005. 2, 19, 21, 78
- [Kim 02] D Kim, E Kobayashi, N Hata, I Sakuma & T Dohi. *A 6-Dof Mechanism for a MR-compatible Surgical manipulator*. In In Proc. of the 6th International Conference on Biomedical Engineering and Rehabilitation Engineering, pages 67–69, 2002. 1, 18
- [Koyama 07] T Koyama, K Takemura & Maeno T. *Development of an Ultrasonic Brake*. Journal of Advanced Mechanical Design, Systems, and Manufacturing, vol. 1, no. 1, pages 122–129, 2007. 97
- [Krainak 07] D M Krainak, T B Parrish & J P Dewald. *A method to capture six-degrees-of-freedom mechanical measurements of isometric shoulder and elbow torques during event-related fMRI*. J Neurosci Methods, vol. 161, no. 2, pages 314–322, Apr 2007. 79
- [Kuhtz-Buschbeck 01] JP Kuhtz-Buschbeck, HH Ehrsson & H Forssberg. *Human brain activity in the control of fine static precision grip forces: an fMRI study*. European Journal of Neuroscience, vol. 14, pages 382–90, 2001. 79
- [Kumada 85] A Kumada. *A piezoelectric motor*. Journal of Applied Physics, vol. 24, pages 739–741, 1985. 24
- [Kurosawa 91] M Kurosawa & S Ueha. *Hybrid transducer type ultrasonic motor*. Ultrasonics, Ferroelectrics and Frequency Control, IEEE Transactions on, vol. 38, no. 2, pages 89–92, March 1991. Version disponibil comparer a l'article de 1987 sur le moteur ultrason yhbride. 25
- [Larson 04] BT Larson, AG Erdman, NV Tsekos, E Yacoug, PV Tsekos & IG Koutlas. *Design of an MRI-Compatible Robotic Stereotactic Device for Minimally Invasive Interventions in the Breast*. Journal of Biomechanical Engineering, vol. 126, no. 4, pages 458–465, August 2004. 1, 18
- [Lauria 07] M Lauria, M-A Legault & F Michaud. *High performance differential elastic actuator for robotic interaction tasks*. In American Association

- for Artificial Intelligence Spring Symposium on Multidisciplinary Collaboration for Socially Assistive Robotics, Stanford, March 2007. 32, 77
- [Lauria 08] M Lauria, M-A Legault, M-A Lavoie & F Michaud. *Differential elastic actuator for robotic interaction tasks*. pages 3606–3611, May 2008. 71, 72, 74, 75
- [Lavrinenko 65] V Lavrinenko & M Nekrasov. *USSR Patent n° 217509*, 1965. 23
- [Lemaire-Semail 07] B Lemaire-Semail, Z Dai & F Giraud. *Piezo-actuators for force feedback in human-computer interfaces: Advantages and drawbacks with regard to electromagnetic actuation*. pages 1–8, 2-5 Sept. 2007. 42
- [Longchamp 95] R Longchamp. *Commande numérique de systèmes dynamiques*. PPUR, 1995. 111
- [Maas 00] J Maas, T Schulte & N Frohleke. *Model-based control for ultrasonic motors*. *Mechatronics, IEEE/ASME Transactions on*, vol. 5, no. 2, pages 165–180, June 2000. 30, 31
- [Masamune 95] K Masamune, E Kobayashi, Y Masutani, M Suzuki, T Dohi, H Iseki & K Takakura. *Development of an MRI-compatible needle insertion manipulator for stereotactic neurosurgery*. *Image Guid Surg*, vol. 1, no. 4, pages 242–248, 1995. 1, 18
- [Melzer 08] A Melzer, B Gutmann, T Remmele, R Wolf, A Lukoscheck, M Bock, H Bardenheuer & H Fischer. *INNOMOTION for Percutaneous Image-Guided Interventions*. *Engineering in Medicine and Biology Magazine, IEEE*, vol. 27, no. 3, pages 66–73, May-June 2008. 1
- [Moix 05] T Moix. *Mechatronic Elements and Haptic Rendering for Computer Assisted Minimally Invasive Surgery Training*. Phd thesis No. 1734, École Polytechnique Fédérale de Lausanne (EPFL), 2005. 119
- [Moser 03] R Moser, R Gassert, E Burdet, L Sacher, HR Woodtli, J Erni, W Maeder & H Bleuler. *An MR Compatible Robot Technology*. In *Proc. IEEE International Conference on Robotics and Automation (ICRA)*, volume 1, pages 670–675, September 2003. 2
- [Mraz 03] R Mraz, J Hong, G Quintin, W R Staines, W E McIlroy, K K Zkazanis & S J Graham. *A platform for combining virtual reality experiments with functional magnetic resonance imaging*. *Cyberpsychol Behav*, vol. 6, no. 4, pages 359–368, Aug 2003. 78

- [Müller 82] HW Müller & JH Mannhardt WG and Glover. *Epicyclic drive trains: Analysis, synthesis, and applications*. Wayne State University Press, 1982. 74
- [Newman 92] S Newman W. *Stability and Performance Limits of Interaction Controllers*. *Journal of Dynamic Systems, Measurement, and Control*, vol. 114, no. 4, pages 563–570, 1992. 10, 123
- [Oura 06] M Oura, Y Kobayashi, J Okamoto & MG Fujie. *Development of MRI Compatible Versatile Manipulator for Minimally Invasive Surgery*. In *Proc. first IEEE / RAS-EMBS International Conference on Biomedical Robotics and Biomechatronics (BioRob)*, 2006. 1, 18
- [Pang 91] XD Pang, HZ Tan & NI Durlach. *Manual Discrimination of Force Using Active Finger Motion*. *Perception & Psychophysics*, vol. 49, no. 6, pages 531–540, June 1991. 11
- [Pons 05] J L Pons. *Emerging actuator technologies : a micromechatronic approach*. Wiley, Chichester, England; Hoboken, NJ, 2005. 7, 27
- [Pratt 95] GA Pratt & MM Williamson. *Series elastic actuators*. volume 01, page 399, Los Alamitos, CA, USA, 1995. IEEE Computer Society. 47
- [Riener 05] R Riener, T Villgrattner, R Kleiser, T Nef & S Kollias. *fMRI-Compatible Electromagnetic Haptic Interface*. *Proc. 27th Annual International Conference of the IEEE Engineering in Medicine and Biology Society (EMBC)*, 2005. 2, 79
- [Robinson 99] DW Robinson, JE Pratt, DJ Paluska & GA Pratt. *Series elastic actuator development for a biomimetic walking robot*. In *Proceedings. 1999 IEEE/ASME International Conference on Advanced Intelligent Mechatronics*, pages 561–568, 1999. 49
- [Sakaguchi 98] M Sakaguchi & J Furusho. *Development of ER Actuators and Their Applications to Force Display Systems*. In *Virtual Reality Annual International Symposium*, volume 0, page 66, Los Alamitos, CA, USA, 1998. IEEE Computer Society. 71
- [Sashida 93] T Sashida & T Kenjo. *An introduction to ultrasonic motors*. Clarendon Press, 1993. 23, 24, 25, 26, 39, 40
- [Schenck 96] JF Schenck. *The role of magnetic susceptibility in magnetic resonance imaging: MRI magnetic compatibility of the first and second kinds*. *Medical Physics*, vol. 23, no. 6, pages 815–850, June 1996. 15

- [Senjyu 95a] T. Senjyu, H. Miyazato & K. Uezato. *Quick and precise position control of ultrasonic motors with two control inputs*. volume 1, pages 415–420, 18-22 Jun 1995. 30
- [Senjyu 95b] T Senjyu, K Uezato & H Miyazato. *Adjustable speed control of ultrasonic motors by adaptive control*. Power Electronics, IEEE Transactions on, vol. 10, no. 5, pages 532–538, Sep 1995. 30
- [Senjyu 98] T Senjyu, H Miyazato, S Yokoda & K. Uezato. *Speed control of ultrasonic motors using neural network*. Power Electronics, IEEE Transactions on, vol. 13, no. 3, pages 381–387, May 1998. 30
- [Spaelter 06] U Spaelter. *Haptic Interface Design and Control with Application to Surgery Simulation*. PhD thesis, École Polytechnique Fédérale de Lausanne (EPFL), June 2006. 9
- [Spanner 06] K Spanner. *Survey of the Various Operating Principles of Ultrasonic Piezomotors*. In Actuator, 2006. 23
- [Sutherland 03] GR Sutherland, PB McBeth & DF Louw. *NeuroArm: an MR compatible robot for microsurgery*. In CARS 2003. Computer Assisted Radiology and Surgery. Proceedings of the 17th International Congress and Exhibition. International Congress Series, volume 1256, pages 504–508, June 2003. 79
- [Tada 02] M Tada, S Sasaki & T Ogasawara. *Development of an Optical 2-axis Force Sensor Usable in MRI Environments*. In Proc. IEEE Sensors, volume 2, pages 984–989, June 2002. 79
- [Tan 94] HZ Tan, MA Srinivasan, B Eberman & B Cheng. *Human factors for the design of force-reflecting haptic interfaces*. Dynamic Systems and Control, vol. 55, no. 1, pages 353–359, 1994. 11
- [Ueha 00] Y Ueha S and Hashimoto & Y Koike. *Non-contact transportation using near-field acoustic levitation*. Ultrasonics, vol. 38, no. 1-8, pages 26–32, March 2000. 26
- [Ushino 97] K Ushino. *Piezoelectric actuators and ultrasonic motors*. Kluwer Academic Publishers, 1997. 24
- [Vogan 04] J Vogan, A Wingert, JS Plante, S Dubowsky & M Hafez. *Manipulation in MRI Devices using Electrostrictive Polymer Actuators: With an Application to Reconfigurable Imaging Coils*. Proc. IEEE International Conference on Robotics and Automation (ICRA), pages 2498–2504, 2004. 20

- [Yamamoto 05] A Yamamoto, K Ichiyanagi, T Higuchi, H Imamizu, R Gassert, M Ingold, L Sache & H Bleuler. *Evaluation of MR-Compatibility of Electrostatic Linear Motor*. In Proc. IEEE International Conference on Robotics and Automation (ICRA), pages 3658–3663, 2005. 17, 19
- [Zappe 04] AC Zappe, T Maucher, K Meier & C Scheiber. *Evaluation of a Pneumatically Driven Tactile Stimulator Device for Vision Substitution During fMRI Studies*. J Magn Reson Med, vol. 51, no. 4, pages 828–834, 2004. 2
- [Zhang 06] R Zhang, A Kunz, P Lochmatter & G Kovacs. *Dielectric Elastomer Spring Roll Actuators for a Portable Force Feedback Device*. In 14th Symposium on Haptic Interfaces for Virtual Environment and Teleoperator Systems, pages 347–353, March 2006. 20, 21

Nomenclature

Latin Letters

\vec{a}	Acceleration
A	Amplitude of the stator wave (p. 27). ERF specific constant (p. 98)
B	ERF specific constant
C	Capacitor
D	Viscosity
D_{sda}	SDA damper viscosity
D_{usm}	USM viscous friction
\vec{e}_i	Unit vector along i
E	Electrical field
\underline{F}	Complex applied force
\underline{F}_{dc}	DC motor complex output force
\underline{F}_{in}	System complex input force
\underline{F}_{out}	System complex output force
\underline{F}_{th}	System complex output force with the locked output
\underline{F}_{usm}	USM complex output force
\vec{f}_{ext}	External forces sum
f	Force variable
f_1	Transmission input force (p. 72). Differential first input force (p. 75)
f_2	Transmission output force (p. 72). Differential second input force (p. 75)
f_3	Differential output force
f_{cl1}	Real clutch input force variable
f_{cl2}	Real clutch output force variable
f_{dc}	DC motor output force variable
f_{era}	ERA output force variable
f_{fint}	Finger interface output force variable
f_{hold}	USM holding force
f_{huca}	HUCA output force variable
f_{in}	Input force variable
f_{lim}	Clutch limiting friction force variable

f_{sda}	SDA output force variable
f_{sea}	SEA output force variable
f_{tr}	Clutch transmitted force variable
f_{usm}	USM output force variable
G'_{cl}	Clutch voltage to torque gain
G'_{usm}	USM voltage to velocity gain reflected on the HUCA output
\underline{H}_{dc}	DC motor complex force transfer function with the locked output
\underline{H}_{th}	System complex force transfer function with the locked output
\underline{H}_{usm}	USM complex force transfer function with the locked output
h_{0b}	Height of the stator surface from the neutral plane
H_{huca_f}	HUCA forward transfer function with its locked output and its locked clutch
H_{huca_s}	HUCA forward transfer function with its locked output and its slipping clutch
H_{sda}	SDA forward transfer function with its locked output
H_{sea}	SEA forward transfer function with its locked output
I	Inertia
i	Current variable
I_{cl1}	Real clutch input inertia
I_{cl2}	Real clutch output inertia
I_{dc}	DC motor inertia
I_{usm}	USM rotor inertia
J	Current density
K	Stiffness
k	Wave mode order (p. 27). Sample index (p. 90)
K_f	Torque feedback proportional gain
K_p	USM velocity feedback proportional gain
K_v	Velocity to torque conversion constant
K_{sea}	SEA spring stiffness
L	Inductor
M	Mass
n	Transmission or differential gear ratio
n_1	Differential first input gear ratio
n_2	Differential second input gear ratio
n_3	Additional transmission gear ratio
n_{brake}	Differential gear ratio of the brake to the HUCA output
n_{usm}	Differential gear ratio of the USM to the HUCA output
P	ERF specific linear conductivity
Q	Stator point (p. 28).ERF specific quadratic conductivity (p. 99)
Q_0	Contact point between the stator and the rotor
R	Amplitude of the stator wave along the radius (p. 27). Resistor (p. 33)
r	Stator radial coordinate
r_ω	Estimated velocity resolution

r_θ	Encoder angular resolution
r_m	Stator mean radius
r_{conv}	Conversion factor from the finger interface to the HUCA
t	Time variable
T_s	Sampling period
t_{brake}	Brake output torque variable
t_{huca}	HUCA output torque variable
t_{lim}	Clutch limiting friction torque variable
t_{sens}	HUCA output measured torque
t_{set}	Desired output torque variable
t_{tr}	Clutch transmitted torque variable
t_{usm}	USM output torque variable
\vec{u}_Q	Position vector of Q
u	Voltage variable
u_{cmd}	USM velocity amplitude command signal
u_{usm}	USM command signal
\underline{V}	Complex velocity
\underline{V}_{in}	USM complex input velocity
\underline{V}_{no}	System complex no-load output velocity
\underline{V}_{out}	System complex output velocity
\underline{V}_{usm}	USM complex output velocity
\vec{v}_Q	Velocity vector of Q
v	Velocity variable
V_{cl1}	Velocity source transfer function of the HUCA and the clutch input inertia
V_{cl2}	Velocity source transfer function of the USM with the locked differential-brake
v_{dc}	DC motor output velocity variable
v_{in}	USM input velocity variable
v_{sda}	SDA output velocity variable
v_{sea}	SEA output velocity variable
V_{usm}	Velocity source transfer function of the USM
v_{usm}	USM rotor velocity variable
w	Stator wave function
\dot{x}_1	Transmission input velocity (p. 72). Differential first input velocity (p. 74)
\dot{x}_2	Transmission output velocity (p. 72). Differential second input velocity (p. 74)
\dot{x}_3	Differential output velocity
\dot{x}_{cl1}	Clutch input velocity variable
\dot{x}_{cl2}	Clutch output velocity variable
x_{era}	ERA output position variable
x_{huca}	HUCA output position variable
x_{sda}	SDA output position variable
x_{sea}	SEA output position variable

x_{usm}	USM output position variable
\underline{Y}	Mechanical complex admittance
\underline{Z}	Mechanical complex impedance
\underline{Z}_1	Complex impedance on the transmission input
\underline{Z}'_1	Reflected complex impedance on the transmission input seen from the output
\underline{Z}_{dc}	DC motor complex output impedance
\underline{Z}_{out}	System Complex output impedance
\underline{Z}_{usm}	USM complex output impedance
Z_{era}	ERA output impedance
Z_{huca_i}	HUCA output impedance with its locked clutch
Z_{huca_s}	HUCA output impedance with its slipping clutch
Z_{sda}	SDA output impedance
Z_{sea}	SEA output impedance

Greek Letters

$\dot{\gamma}$	Shear rate
ΔD_{usm}	Non-linearities of the USM rotor friction
Δf_{sda}	Non-linearities on the SDA output force
$\Delta x_{usm_{min}}$	USM position minimum achievable increment
$\Delta \dot{x}_{cl}$	Clutch slipping velocity variable
$\Delta \omega_{cl}$	Clutch slipping angular velocity variable
$\Delta \theta$	Angular deflection of the virtual wall
$\Delta_{max} \omega_{huca}$	HUCA output maximum velocity increment
θ_m	Measured angular position
θ_{huca}	HUCA angular position variable
θ_{wall}	Virtual wall angular position
λ	Wave length (p. 27). Damping factor (p. 49)
μ	Friction coefficient
μ_0	ERF viscosity without electrical field
μ_{pl}	Plastic viscosity
τ	Shear stress (97). Time constant of the filter (111)
τ_y	Yield stress
$\dot{\phi}_{rotor}$	Rotor angular velocity
ϕ	Stator angular coordinate
ω	Angular frequency
ω_0	Natural angular frequency
ω_1	Damped natural angular frequency
ω_e	Estimated velocity
ω_{brake}	Brake output angular velocity variable

$\omega_{critical}$	Bandwidth of an critically-damped oscillator
ω_{huca}	HUCA output angular velocity variable
ω_{lim}	Clutch slipping velocity limit
ω_{over}	Bandwidth of an over-damped oscillator
ω_{sda}	SDA open-loop bandwidth
ω_{sea}	SEA open-loop bandwidth
ω_{set}	USM desired velocity
ω_{under}	Bandwidth of an under-damped oscillator
ω_{usm}	USM output angular velocity variable

Superscripts

'	Reflected value of an impedance seen trough the output of a transmission/differential
---	---

Curriculum Vitae

Personal Data

Name: Dominique Chapuis
Date of Birth: 29.06.79
Place of Birth: Fribourg
Nationality: Swiss

Education

2004-2009 École Polytechnique Fédérale de Lausanne (EPFL)
Ph.D. project at the Laboratoire de systèmes robotiques (LSRO)
2003-2004 École Polytechnique Fédérale de Lausanne (EPFL)
Research assistant at the Laboratoire de systèmes robotiques (LSRO)
1998-2003 École Polytechnique Fédérale de Lausanne (EPFL)
Degree: Ing. Dipl. Microtechnique
1998-2003 Collège St-Michel, Fribourg
Degree: Maturité fédérale type C (science)

List of Publications

Journal papers

1. R Gassert, D Chapuis, H Bleuler, and E Burdet, “Sensors for applications in magnetic resonance environments,” *Mechatronics, IEEE/ASME Transactions on*, vol. 13, no. 3, pp. 335–344, June 2008.
2. F Barrot, D Chapuis, T Bosgiraud, B Löhr, L Sache, L Moser, and H. Bleuler, “Preliminary investigations on a diamagnetically levitated linear conveyor,” *IEEEJ Trans. IA*, vol. 126, no. 10, pp. 1341–1344, 2006.
3. R Gassert, A Yamamoto, D Chapuis, L Dovat, H Bleuler, and E Burdet, “Actuation methods for applications in MR environments,” *Concepts in Magnetic Resonance Part*

B: Magnetic Resonance Engineering, vol. 29B, no. 4, pp. 191–209, October 2006.

Book Chapters

R Gassert, D Chapuis, N Roach, A Wing, and H Bleuler, *2-DOF fMRI-Compatible Haptic Interface for Bimanual Motor Tasks with Grip/Load-Force Measurement*. The sense of touch and its rendering, volume 45 of *Springer Tracts in Advanced Robotics*, 2008.

Peer-reviewed Conference Proceedings

1. D Chapuis, R Gassert, E Burdet, and H Bleuler, “A hybrid ultrasonic motor and electrorheological fluid clutch actuator for force-feedback in mri/fmri,” in IEEE Engineering in Medicine and Biology Society, August 2008.
2. D Chapuis, X Michel, R Gassert, C-M Chew, E Burdet, and H Bleuler, “A haptic knob with a hybrid ultrasonic motor and powder clutch actuator,” March 2007, pp. 200–205.
3. D Chapuis, R Gassert, E Burdet, and H Bleuler, “Hybrid ultrasonic motor and electrorheological clutch system for MR-compatible haptic rendering,” in Proc. IEEE/RSJ International Conference on Intelligent Robots and Systems (IROS), 2006.
4. L Dovat, O Lambercy, Y Ruffieux, D Chapuis, R Gassert, H Bleuler, C Teo, and E Burdet, “A haptic knob for rehabilitation of stroke patient,” in Proc. IEEE/RSJ International Conference on Intelligent Robots and Systems (IROS), 2006.
5. D Chapuis, R Gassert, G Ganesh, E Burdet, and H Bleuler, “Investigation of a cable transmission for the actuation of MR compatible haptic interfaces,” in Proc. first IEEE / RAS-EMBS International Conference on Biomedical Robotics and Biomechatronics (BioRob), 2006.
6. U Spaelter, D Chapuis, R Gassert, R Moser, and H Bleuler, “A versatile MRI/fMRI compatible spherical 2-DOF haptic interface,” in Proc. first IEEE / RAS-EMBS International Conference on Biomedical Robotics and Biomechatronics (BioRob), 2006.
7. L Dovat, R Gassert, D Chapuis, G Ganesh, E Burdet, and H Bleuler, “A haptic interface based on potential mechanical energy to investigate human motor control using fMRI,” Proc. 27th Annual International Conference of the IEEE Engineering in Medicine and Biology Society (EMBC), pp. 5021–5024, 2005.
8. M Flueckiger, M Bullo, D Chapuis, R Gassert, and Y Perriard, “fMRI compatible haptic interface actuated with traveling wave ultrasonic motor,” Proc. IEEE Industry Applications Society (IAS), vol. 3, pp. 2075–2082, 2005.

9. *D Chapuis, R Gassert, L Sàche, E Burdet, and H Bleuler, "Design of a simple MRI/fMRI compatible force/torque sensor," in Proc. IEEE/RSJ International Conference on Intelligent Robots and Systems (IROS), vol. 3, 2004, pp. 2593–2599.*
10. *E Burdet, R Gassert, G Gowrishankar, D Chapuis, and H Bleuler, "fMRI compatible haptic interfaces to investigate human motor control," Proceedings of the 9th International Symposium on Experimental Robotics (ISER), June 2004.*
11. *V Hartwig, N Vanello, R Gassert, D Chapuis, M Santarelli, V Positano, E Ricciardi, P Pietrini, L Landini, and A Bicchi, "A compatibility test for tactile displays designed for fMRI studies," in Proc. EuroHaptics 2004, June 2004, pp. 456–458.*